Tungsten transport in a tokamak : a first-principle based integrated modeling approach

Sarah Breton

AIX-MARSEILLE UNIVERSITÉ
CEA CADARACHE
ECOLE DOCTORALE 352 PHYSIQUE ET SCIENCES DE LA MATIERE
CULHAM CENTER OF FUSION ENERGY
Institut de Recherche sur la Fusion par confinement Magnétique

Thesis presented in fulfilment of the requirement for the Degree of Doctor

Sarah BRETON

Tungsten transport in a tokamak : a first-principle based integrated modeling approach

Defensed on 12/01/2018 before the jury composed of :

Dr. Yannick MARANDET	Aix-Marseille Université	PhD Director
Dr. Clarisse BOURDELLE	CEA Cadarache	PhD supervisor
Pr. Frank JENKO	Max Planck Institute of Plasma Physics	Referee
Dr. Alberto LOARTE	ITER Organization	Referee
Pr. Peter BEYER	Aix-Marseille Université	Examiner
Dr. Francis CASSON	Culham Centre for Fusion Energy	Examiner

Numéro national de thèse/suffixe local : 2017AIXM0001/001ED62

Table of contents

List of figures

1Introduction

1.1 Introduction of the chapter

This chapter first briefly recalls the global energy context before introducing the concept of thermonuclear fusion and its many advantages. In a second time the tokamak configuration is detailed and the notion of transport is introduced. The next section deals with Tungsten (W) material, the reasons why it is used in a tokamak but also the challenges it brings, as well as the situation on the understanding of the W behavior. Finally, the last section exposes the computational tools needed to model W behavior, called integrated modeling.

1.2 Global energy context

1.2.1 Energy needs and resources

In the past 40 years, the global energy demand more than doubled. Between 1973 and 2015, according to figure 1.1 from [3], the global primary energy supply went from 6 000 million tonnes of oil equivalent (Mtoe) to over 13 000 Mtoe. This rise in energy demand has slowed down in the last years because of the economic growth stabilization in developed countries. However the energy needs are predicted to expand by 40% between 2015 and 2040 [2], mainly due to the economic development of emerging coutries like China, India.

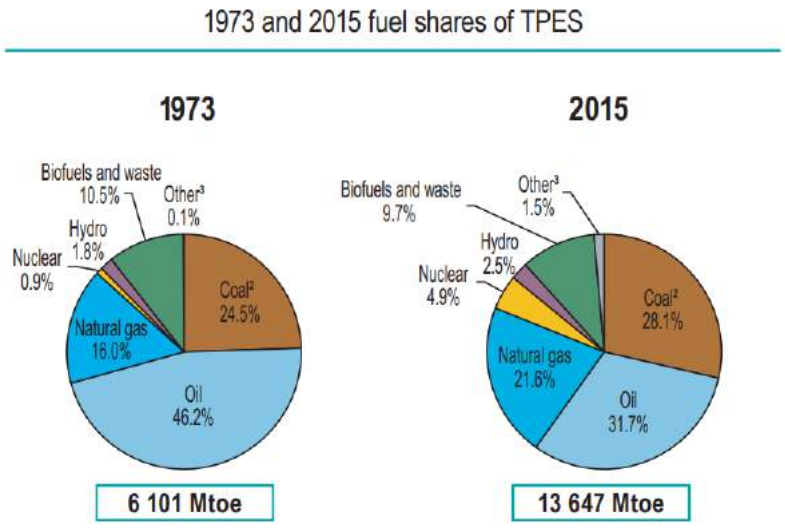

Figure 1.1 – Graph of the fuel shares in 1973 and 2015 [3]

Figure 1.1 shows that in 2015 about 80 % of this energy comes from fossil fuels (ie oil, natural gas and coal). Fossil fuels were the motors of the industrial

revolution in the XIXth century. They have many advantages, such as being abundant and accessible. Fossil fuels provide a large amount of concentrated energy for a relatively low cost.

However fossil fuels have two main flaws. The first one is, they have limited reserves. Assuming that the global fossil fuel consumption remains at its 2016 level, it is estimated that we have about 50 years of oil and natural gas (including shale gas) left, along with 150 years of coal [23]. The second issue raised by fossil fuel, is the pollution and its impact on global warming. Between 1971 and 2015, the amount of CO_2 generated by fossil fuels went from 15 500 Mega tonnes/year to 32 000 Mega tonnes/year. The link between greenhouse gas (such as CO_2) and global warming has been established [75] and the global increase temperature must be limited to 2°C. If not, 20% to 30% of fauna and flora will be threatened of extinction, the frequency of extreme climate events will increase. [131] The global warming also impacts food production and therefore food insecurity.

Overall, the energy challenge has two faces : meeting the increasing energy demand, and providing clean and sustainable resources.

1.2.2 Low carbon and sustainable energy sources

Sustainable energy sources represent only 14% of the total energy supply. Several renewable energies sources are developed. The biggest contributor is the hydropower which constitutes 70% of the global renewable electricity production. However hydropower almost reached its maximum deployment in developed countries and its global potential is limited. Solar and wind contribute at a very small scale to the energetic mix despite their strong increase in the past decades. Their main advantages are the low greenhouse gas emission and the unlimited energy source (sun and wind). However those energy sources are limited by the intermittency of their production and the lack of efficient solution to store electricity once produced, making them not well adapted to massive centralized electricity production.

Nuclear energy represents 5% of the energetic mix. France is the country with the biggest contribution of nuclear energy (70% of our electricity comes from nuclear plants) and produces 17% of the world nuclear energy. The nuclear reaction used in these nuclear plant, is called nuclear fission. It consists in breaking the bounds between nucleus elements, which releases energy. Nuclear fission has many advantages, such as no greenhouse gas emission, massive, constant and controllable electricity production, good efficiency. However, nuclear energy has some serious drawbacks, starting with the economical costs needed to ensure the safety of the nuclear power plants. Moreover, the disposal of nuclear waste is still a topic under investigation [50]. Finally, Uranium resources are also limited. Assuming a stabilized global consumption and based on the current nuclear power plant technologies (Generation III), the Uranium resources would last about 100 years [13]. Actual researches investigate several reactor systems (Generation IV) for more efficient, cleaner and safer power plants. [1]

Fission is not the only possible nuclear reaction. Figure 1.2 illustrates the binding energy/nucleon depending on the atomic mass. Liberating energy is possible with fission of heavy nuclei and fusion of lighter nuclei. Fusion is the reaction that occurs in the core of the sun and other stars, where hydrogen isotopes gather to form helium. Note that the fusion reaction releases 5 times more energy per nucleon compared with fission.

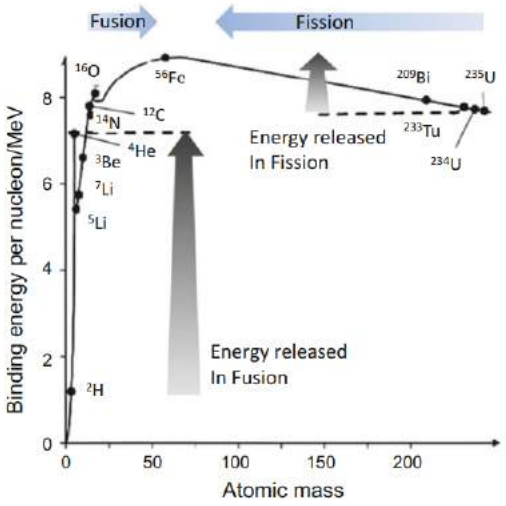

Figure 1.2 – Graph of the nuclear energy released depending on atomic mass [130]

Nuclear fusion does not directly produce greenhouse gas nor long-lived radioactive waste. It does not require chain process, so there is no risk of runaway reaction. Moreover, it necessitates little reactant quantities. Indeed, per year, a 1 000 MW coal power plant requires 2.7 million tons of coal. For the same power per year, a fusion power plant would need only 250 kg of hydrogen isotopes [101]. As a comparison, generating the same power currently requires per year around 200 tons of natural Uranium [122].

The next section focuses on the nuclear fusion process. A brief history of nuclear fusion is given, along with the possible fusion reactions. Finally, the conditions for a nuclear fusion are developed.

1.3 Nuclear fusion process

1.3.1 Brief history of nuclear fusion

In his book "A piece of the sun", Daniel Clery tells the story of the nuclear fusion from 1930 until today [38]. The interest in nuclear fusion developed around the Second World War, during the race for the nuclear weapon. In 1952, the first bomb using nuclear fusion, called H bomb, was tested. In the 50s, the first fusion experimental devices were operating in USSR, USA, United Kingdom, France and Japan. Progress in nuclear fusion were significantly hampered by the Cold War

and the lack of knowledge sharing between USSR and the occidental world until 1958. Nuclear fusion happens in the core of the sun thanks to its large mass but it requires very high temperatures (about 150 million degrees) to produce fusion reaction on Earth. At those temperatures, the nuclei are separated from the electrons, forming a very hot ionized gas called plasma. Therefore the first issue was to protect the reactor walls from the plasma. The break-through solution, first imagined in the USA in 1951 by Lyman Spitzer, is the use the pinch effect and magnetic fields to contain the fusion reactants : this method is called magnetic confinement. The operation of a fusion reactor requires a very wide spectrum of physics topics, from supra conductive magnets to atomic and material physics. Those specificities make international collaboration in fusion research a key element. The Joint European Torus (JET) in Culham (United Kingdom), which is currently the world's biggest tokamak, is an example of international collaboration (on the left on figure 1.3). In 1991, JET "achieved the world's first controlled release of fusion power in 1991" [110, 100]. In 2003, the longest controlled fusion reaction was achieved by the French tokamak Tore Supra [132].

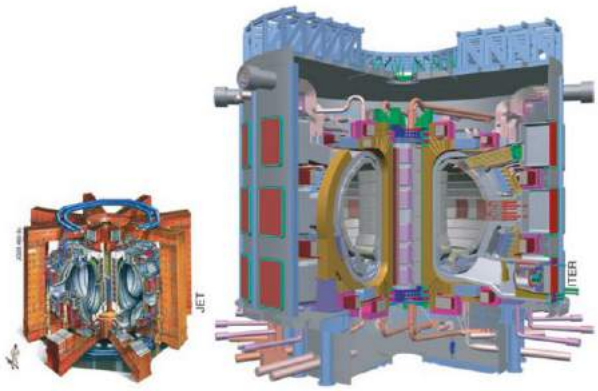

Figure 1.3 – Scheme of JET and ITER tokamaks (from https ://www.iter.org/)

The next milestone is to reach the "break-even" point, when the energy released by the fusion reaction compensates for the energy consumed to produce it. The tokamak ITER ("the way" in latin), currently under construction in France, will be the world's largest tokamak with a plasma volume 8 times bigger compared with JET (on the right on figure 1.3). ITER's objective is to go beyond the "break-even" point and generate 10 times the energy it consumes : 500MW of fusion power for 50MW of input power in 400 to 600s [102]. ITER will demonstrate our ability to control nuclear fusion and use it as an energy source. Finally, the DEMO (DEMOnstration power plant) reactor, even bigger than ITER, will be the first fusion reactor that actually produces electricity.

70 years of research on magnetic confinement nuclear fusion lead to several milestones on the design, geometry and materials required to achieve fusion reaction. Two main reactor designs are currently exploited : the doughnut-shaped tokamak (Russian acronym from "TOroidal'naya KAMera s AKsial'nym magnitnym

polem", ie toroidal chamber with an axial magnetic field) and the stellerator [123]. The study on the wall materials showed that metallic walls were problematic due to core radiation. Carbon, chosen as a replacement, caused other problems, such as erosion and hydrogen isotope retention. In the mean time the plasma geometry had evolved (explained below in section 1.4), allowing actual machines to come back to metallic materials such as Beryllium and W. Also, additional heating sources are needed to reach the temperature required to get fusion reaction. However this creates turbulent transport in the plasma and strongly modifies its behavior. The heating systems, the different transport mechanisms and the different plasma geometries will be developed in the section 1.4.

1.3.2 The nuclear fusion reaction

As mentioned earlier, the nuclear fusion reaction consists in two light nuclei gathering to form an heavier nucleus and subatomic particles (neutrons or protons). However the two nuclei repel each other as they are both charged positively. In order to get the fusion reaction, the reactants must be sufficiently close together, and a certain amount of energy is therefore vital to overcome the electrostatic repulsion and reach the space, extremely close to the nucleus, where fusion can happen. The probability of overcoming the electrostatic repulsion is expressed using the effective cross section. Figure 1.4 shows the effective cross sections for several fusion reactions depending on the interaction energy expressed in keV.

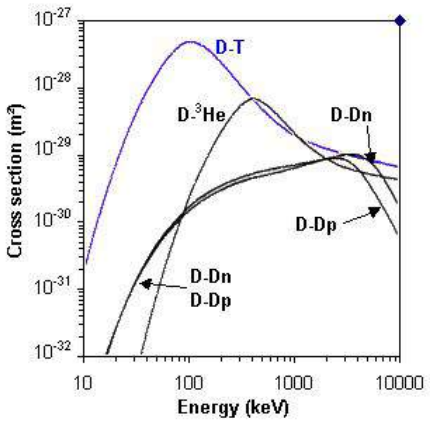

Figure 1.4 – Cross-sections of potential fusion reactions depending on interaction energy [32]

The combination Deuterium-Tritium (D-T), two hydrogen isotopes, offers by far the highest cross-section, with a maximum at 100 keV. The D-T fusion reaction is written below on equation 1.1 :

$$ {}^{2}_{1}D + {}^{3}_{1}T \longrightarrow {}^{4}_{2}He(3.5MeV) + {}^{1}_{0}n(14.1MeV) \tag{1.1} $$

Deuterium resources are almost unlimited since it can be extracted from sea

water (33g from one meter cube of seawater). Tritium is an unstable radioactive element with a half-life of 12.3 year, therefore it cannot be found as is in nature. The solution is to produce Tritium by placing Lithium blankets in the fusion reactor and taking advantage of the neutrons produced by the fusion reactions :

$$^{6}_{3}Li +^{1}_{0} n \longrightarrow^{4}_{2} He(2.1MeV) +^{3}_{1} T(2.7MeV) \tag{1.2}$$

Lithium can be extracted from salt flats and is the 25th most abundant element on Earth crust [67].

1.3.3 Conditions for a fusion reaction : confinement time and Lawson criteria

As briefly mentioned above, very high temperatures are required to produce fusion but there is a permanent energy loss, compensated by external heating systems. The plasma confinement time τ_e is a key parameter which characterizes the time needed for all the stored energy to leave the plasma, once all the heating systems are switched off. It is defined as the ratio of the total energy of the plasma W, over the power loss P_L : $\tau_e = \dfrac{W}{P_L}$. The bigger the confinement time, the better the performances. The power loss is defined as $P_L = P_H + P_\alpha$, as the sum of the external heating supply P_H and the thermonuclear power P_α, generated by the Helium (also called α) particles produced during a fusion reaction (see equation 1.1). Ultimately, the goal is to reach ignition, when the plasma is self-heated thanks to the α-particles, so no external power heating. This ignition point can be written as [139] :

$$n\tau_e \gtrsim \frac{T}{< \sigma v > E_\alpha} \tag{1.3}$$

with σ the cross-section shown on figure 1.4, n, T and v and the particle density, temperature and velocity, and E_α the α-particles energy.

Around 10-20 keV, which is about the functioning temperature of ITER, the reaction rate $< \sigma v >$ values borders up $10^{24} T^2 m^3 s^{-1}$. With the α-particle energy from equation 1.3 E_α=3.5 MeV it gives $nT\tau_e \gtrsim 3.10^{21} m^{-3} keV s$. This expression, which is an updated version of what is called the Lawson criteria [88] illustrates that the key parameters to produce fusion are the density, temperature and confinement time. It is clear from figure 1.4 that the temperature must be around 10 keV in order to maximize the cross-section of the fusion reaction. It leaves two possible configurations : high density and low confinement time, or low density and high confinement time. The first configuration corresponds to inertial confinement fusion [83], developed at the National Ignition Facility [92] or the Laser Mega Joule [53]. The second configuration corresponds to magnetic confinement fusion and is studied with tokamaks and stellarators. For example, for magnetic confinement fusion, the configuration T=10 keV $n = 10^{20} m^{-3}$ and $\tau_e = 3$s allows to reach ignition.

1.4 The tokamak configuration and confinement

1.4.1 The tokamak configuration

Figure 1.5a shows a sketch of a tokamak with its main elements. The plasma chamber is also called the vacuum vessel. The magnetic field is a combination of a toroidal component (green arrows in the φ direction) and a poloidal component (in the θ direction). The combination of these two magnetic fields create an helicoïdal magnetic field, as illustrated on figure 1.5b. The toroidal component is generated by the toroidal magnetic coil. The central solenoïd in red induces an electrical current in the plasma, in the toroidal direction. This electric current generates the poloidal magnetic field, completed by the poloidal magnetic coils.

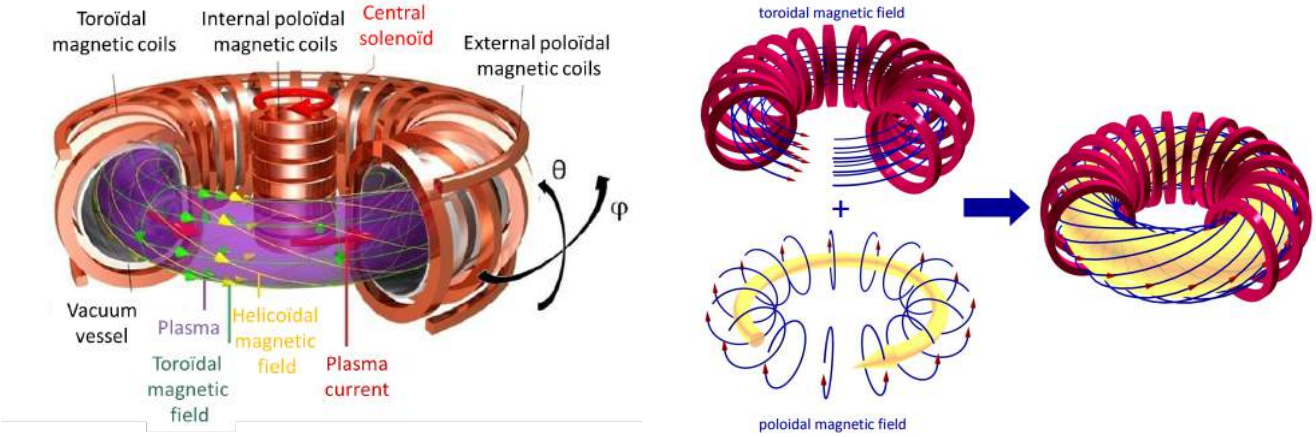

(a) Tokamak. (b) Magnetic field lines.

Figure 1.5 – Cartoons of a tokamak [48] and the magnetic field lines [40]

Figure 1.6 illustrates two possible plasma geometries. In both cases, the plasma core corresponds to the zone confined by closed magnetic field lines. The region in grey, after the Last Closed Magnetic Surface (LCMS) and before the wall, is the Srape-Off-Layer (SOL). The simplest geometric figure is a circular plasma, with the LCMS connected to the wall through the limiter. The circular shape was the first one studied in tokamaks, but the proximity between the plasma core and the wall led to important wall erosion. The divertor (or X point) configuration solves this issue by secluding the areas of plasma/wall interaction away from the plasma core. As a result, the impurity content of the plasma core was significantly reduced, which allowed the metallic materials to come back in the tokamak. The divertors of JET, ASDEX-Upgrade and WEST are now made of W for less erosion, less Tritium retention and higher melting point. The divertor configuration requires an extra magnetic coil that shapes the X point and the two divertor legs.

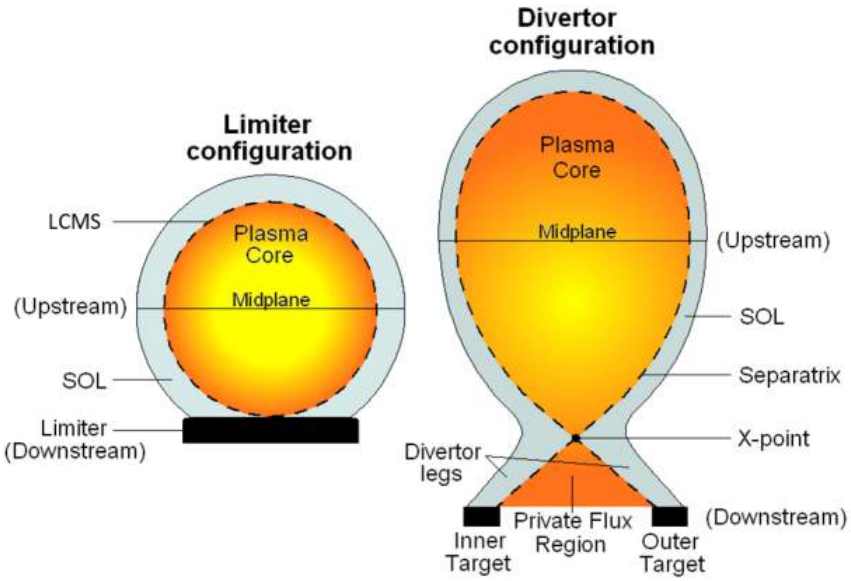

Figure 1.6 – Two plasma geometries (circular and X point) [63]

As mentioned above, the fusion reaction requires very high temperatures. The plasma current (in red on figure 1.5a) already provides Ohmic heating, due to plasma resistivity. However the Ohmic heating is limited because the resistivity decreases while the temperature rises. Therefore, several additional heating systems are required. The Neutral Beam Injection (NBI) consists in injecting fast Deuterium atoms in the plasma. Those atoms get ionized and transfer their kinetic energy by collisions. This heating method injects energy, particles and momentum to the plasma, as will be seen in chapter 3. Another method consists in injecting electromagnetic waves at specific frequencies. This method is called ECRH or ICRH (Electron or Ion Cylotron Resonance Heating) depending on the targeted particle. ICRH covers frequencies from 10 tp 50 MHz, ECRH uses much higher frequencies up to 100 GHz. A third frequency range(3 to 5 GHz) is covered by LHCD (Lower Hybrid Current Drive).

The use of these additional heating sources allows to dramatically increase the input power and this strongly impacts the plasma behavior. Above a power threshold a high confinement configuration is reached, called H-mode (visible on figure 1.7). H-mode is characterized by a pressure pedestal at the plasma edge, which is a consequence of the confinement improvement (around two times bigger) through the reduction of turbulence. The turbulence reduction creates an edge transport barrier (ETB on figure 1.7), decreasing the energy and particle loss from the core, and thus steepening the gradients. This mechanism leads to the formation of a pedestal. Thanks to the pedestal, the H mode allows the plasma pressure to be much higher than in L-mode, which is the low confinement configuration. However the H-mode also brought some magnetohydrodynamic (MHD) instabilities, such as Edge Localized Modes (ELMs). ELMs [141] are short bursts of the order of the ms which occur above a threshold edge pressure. As a

consequence particle and energy are expelled from the pedestal and are concentrated on the target at the bottom of the divertor legs (on figure 1.6). Other core MHD phenomena occur, such as sawteeth [135]. They correspond to periodic and abrupt collapses of the plasma pressure in the plasma center, followed by rebuilding phases of the temperature and density profiles.

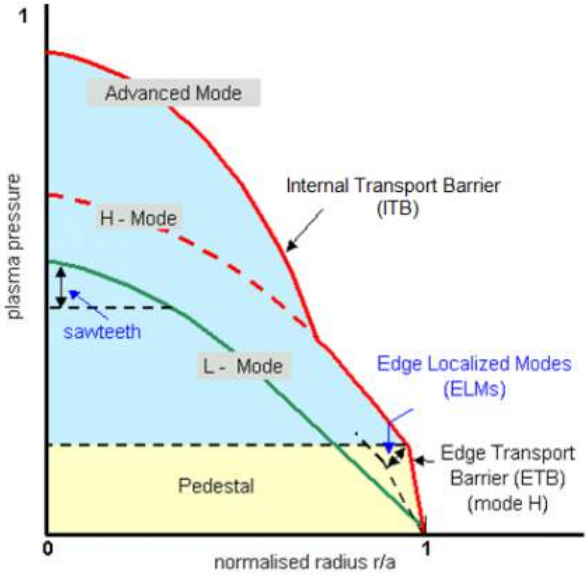

Figure 1.7 – Cartoon of L and H modes plasma pressure profiles with pedestal, ETB/ITB, ELMs and sawteeth [31]

In the H-mode configuration, there are two main kinds of plasma scenarii : baseline and hybrid. The baseline pulse corresponds to high confinement mode, with high plasma current [113]. Its purpose is to reach high power performances, but those pulses often present MHD instabilities such as sawteeth and Neoclassical Tearing Modes (NTMs), which lead to plasmas more prone to disruptions. The hybrid is an alternative configuration [79], with less plasma current and therefore lower performances. This allows, theoretically, to avoid the current configuration responsible for the appearance of sawteeth and NTMs and therefore longer and more stable pulses.

1.4.2 Transport in the plasma

Confinement is the key parameter for magnetic confinement fusion. Confinement is limited by thermal and particle losses, as well as radiation. In absence of instabilities, confinement inside a tokamak depends on Coulomb collisions, whose effect are described by neoclassical transport. However this collisional physics has been demonstrated to be inadequate to explain experimental measurements [93]. Indeed, anomalous or turbulent transport, caused by instabilities in the plasma, is the main contributor to the total particle, heat and momentum transport.

In the plasma core, particle, heat and momentum obey the local transport equation $\frac{\partial}{\partial t}[Density] + \vec{\nabla}[\vec{Flux}] = [Source]$. This expression assumes that the time evolution of temperature and density is smaller than the characteristic transport time scale, and their variation length is smaller than the characteristic correlation length. The transport equation can be adapted as follows, for particles (equation 1.4) and heat (equation 1.5)[109] :

$$\frac{\partial n}{\partial t} + \vec{\nabla}\vec{\Gamma} = S \tag{1.4}$$

$$\frac{3nk_B}{2}\frac{\partial T}{\partial t} + \vec{\nabla}\vec{q} = W \tag{1.5}$$

with n the particle density, Γ the particle flux ($m^{-2}.s^{-1}$) and S the particle source ($m^{-3}.s^{-1}$) ; T is the temperature, q is the heat flux (W.m^{-2}) and W the heat source (W.m^{-3}).

The particle flux from equation 1.4 is modeled as the sum of a diffusive and a convective contributions :

$$\Gamma = -D\nabla n + Vn \tag{1.6}$$

With $D = D_{turb} + D_{neo}$ and $V = V_{turb} + V_{neo}$ the diffusion and convection coefficients, each of them composed of a turbulent and a neoclassical part. This definition implies that it is an accurate assumption to sum neoclassical and turbulent contributions. It has been demonstrated that this assumption is not exact, some synergy exists between turbulent and neoclassical contributions. However it does not drastically modify the transport properties [49].

1.4.2.1 Turbulent transport

Turbulent transport of particles, heat and momentum results from fluctuations induced by instabilities at the microscopic scale. Instabilities occur because of the many free energy sources (pressure gradients, drift velocities...) which, in specific configurations, can create a self-amplifying loop which impacts the plasma behavior and degrades the confinement.

Drift-wave and interchange instabilities Plasma core instabilities can mainly have two physical origins : drift-wave and interchange phenomena.

Interchange instabilities represent the majority of the encountered instabilities in the plasma core. They are caused by the presence of magnetic field non-homogeneity and strong density and temperature gradients. Interchange occurs under the condition that the magnetic field and pressure gradients are aligned, which happens only on the Low Field Side (LFS). In this configuration, let us consider a small local ion cell and a small electron cell. This configuration creates opposite drift velocities for ions and electrons (see chapter 2 section 2.2 about drift velocities). As a consequence, ions are driven in the ion cell while electrons

travel to the electron cell. This creates an amplified electric potential which is destabilizing. Since interchange instabilities can only occur in presence of magnetic curvature, they are also referred to as "toroidal" instability category.

The description of the drift-wave instability requires the assumption that electrons, due to their small mass, follow almost instantaneously the variations of any electric potential fluctuation, given that the frequency of the fluctuation is small enough compared with the electrons parallel dynamic. The fluctuation of the electron density creates zones with higher densities and zones with lower densities. If the electron density and the electric perturbation are in phase, a drift velocity (explained in chapter 2 section 2.2) smooths out the electron density gradients. But if the electron density and the electric perturbation are not in phase, the drift velocity amplifies the electron density gradients, which leads to charge accumulations. Since the drift-wave instability does not depend on the gradient and curvature of the magnetic field, it is referred to as the "slab" instability category.

The kind of instabilities present in the plasma core can have drift-wave and/or interchange components. Ion Temperature Gradient (ITG) which has both drift-wave and interchange components, mainly depends on the ratio $d(logT_i)/d(logn_i)$. The Electron Temperature Gradient (ETG) is similar to ITG, driven by $d(logT_e)/d(logn_e)$. The Trapped Electron Mode (TEM) is caused by trapped electrons, also driven unstable by both electron temperature and density gradients.

Modeling turbulent transport In order to understand and predict turbulent transport in current and future experiments, several computational tools have been developed over time, with various degrees of accuracy and therefore various computational requirements. Since it is not feasible to model each particle separately, two descriptions of the plasma are possible : the fluid and the kinetic approaches. The kinetic approach studies the evolution of the distribution function in the velocity and phase space. This gives a 6 dimension problem, which can be reduced to a 5-D problem using the gyrokinetic assumption. This assumption applies to strongly magnetized plasmas by averaging over the gyro-orbits. The fluid approach solves the Vlasov equation for moments of the distribution function and requires an additional closure relation [27, 41].

For either plasma description (kinetic or fluid), several levels of description are available. The most time consuming method, called the non-linear approach, accounts for the cross terms between fluctuating quantities such as the density and the electric potential. A non-linear gyrokinetic code can be either "δf" (i.e. calculates only the deviations from the equilibrium distribution function) or "full-f" (i.e. calculates the complete distribution function). The approach can be either local with only one value of temperature, density and their gradients, or global with full profiles. A less-time consuming approach studies the linear plasma response to a weak perturbation : it is the quasi-linear approach. The complexity of a code also depends on the chosen collision operator.

Figure 1.8 displays different turbulent transport codes, divided in six sections

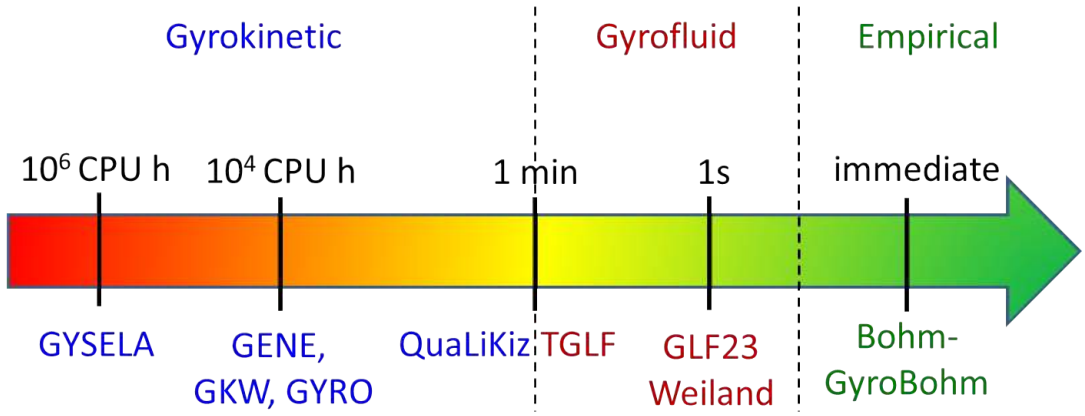

Figure 1.8 – Cartoon of different turbulent codes depending on their computational time. Gyrokinetic codes in blue, gyrofluid ones in red and empirical one in green

depending on their computational time, from the most expensive on the left, to the less expensive on the right. GYSELA [62] is a non-linear 5D gyrokinetic code able to perform global, full-f and flux-driven simulations. A reduced and linearized multi-species collision operator has been recently implemented [49]. GYSELA treats electrons as adiabatic, and accounts for ITG instabilities. Due to its global approach, GYSELA simulations are very expensive with a computational cost around 10^6 CPU hours for one radial position. The next codes in line (GENE [77], GKW [105] and GYRO [25]) are non-linear gyrokinetic codes which all share a fixed discretized grid in the phase space (called the Eulerian approach), and the use of periodic, or "flux-tube", radial boundary conditions. Those settings allow to save CPU time so for one radius the computational time borders up 10^4 CPU hours. They all account for ITG, ETG and TEM. They also propose a general geometry and the impact of the rotation on the turbulence is accounted for. Moving away from the non-linear codes, QuaLiKiz [22, 20, 37] proposes a gyrokinetic quasi-linear approach, which brings the computational time down to less than a minute for one radial position. QuaLiKiz mode of operation is described in chapter 3 section 3.3. TGLF [99, 127] is also a quasi-linear code, but with a gyro-Landau fluid description and general geometry. TGLF accounts for ITG, ETG and TEM, and has the same order of magnitude of CPU time as QuaLiKiz. [20] presents a comparative table of QuaLiKiz and TGLF frameworks. GLF23 [136] is a previously developed version of TGLF, using coefficients tuned on linear gyrokinetic and nonlinear fluid simulations. The Weiland model [137] is another fluid model which uses an "advanced" closure rule, and accounts for TEM. Both GLF23 and Weiland have a computational time around 1s for one radial position. Finally, the Bohm-GyroBohm model [45] is a very fast (almost instantaneous) analytical model based on scaling laws and coefficients empirically tuned on experimental measurements.

1.4.2.2 Neoclassical transport

In a cylindrical plasma, collisional transport can be described using the approach called classical transport. This description is inappropriate in a toroidal plasma. Indeed, the toroidal geometry and the non-uniform magnetic field allow some particles to be trapped on the field lines (as explained on section 2.2 in chapter 2), and their transport cannot be described using the classical transport approach. Therefore the collisional transport in a torus is known as neoclassical transport [139]. In a tokamak plasma, neoclassical transport describes how particles, heat and momentum evolve thanks to collisions, and is more developed in the first section of chapter 2. Note that apart from heavy ions, neoclassical transport is negligible for most species present in the tokamak.

There are several neoclassical codes, at different levels of complexity. NCLASS [74] is a multi-species fluid model with a simplified collision operator, and does not account for the effects of toroidal rotation. NCLASS uses the Hirschman-Sigmar collision operator, based on pitch angle scattering. NEO [15] solves the full drift kinetic equation, providing a first-principle calculation of the transport coefficients directly from the kinetic solution of the distribution function [17]. It uses the full linearized Fokker Planck collision operator [17], which is more accurate than the Hirschman-Sigmar collision operator, especially for multi-species collisions. NEO is also reliable in general geometry, and accounts for the effect of poloidal asymmetries on W distribution. NEO needs about 12 CPU hours for 1s of plasma on 16 processors, which makes its computational cost 1000 times bigger than NCLASS. In chapter 2 section 3 an analytical formulation accouting for poloidal asymmetries from [9] is combined with NCLASS and compared with NEO. NCLASS and NEO are radially local. The PERFECT code [86] accounts for global neoclassical effects and uses the exact linearized Fokker–Planck–Landau collision operator. The PERFECT code accounts for 3D neoclassical effects, which are required for the stellarator configuration. It might also be necessary to model correctly the impact of sawteeth on neoclassical transport in tokamaks [119]. The computational cost for a 4.10^{-6}s simulation is 3 CPU hours, ie 60 000 times slower than NEO.

Now that tokamak configuration and the different kinds of transports are introduced, the next section focuses on the materials used on the tokamak walls, especially Tungsten. First, the advantages that W brings are developed, then the issues caused by W are presented.

1.5 Tungsten as a plasma facing component : advantages and challenges

As briefly mentioned above in section 3.1, the walls of the first plasma magnetically confined devices, operated in limiter configuration, were made of high-Z (with Z the charge) materials. But due to high central radiative losses (see for example [104]), metallic walls were replaced by low-Z graphite and carbon

walls. The use of low-Z materials first improved the plasma performances with a reduction of central radiation, but the scales of the fusion devices increased, the geometry and wall requirements evolved. Low-Z wall material causes other serious problems, such as tritium retention [24], plus limited lifetime of the wall due to erosion [58]. Moreover, the divertor configuration explained above allows to reach low temperature at the target, thus limiting the erosion issue. Therefore high-Z materials are again considered for some wall components. ASDEX-Upgrade, in Germany, installed a 100% W coverage in 2007 [98] and WEST did the same in 2016, in France. JET chose to install ITER-Like Walls (ILW), "solid Beryllium limiters and a combination of bulk W and W-coated carbon fibre composite (CFC) divertor tiles" [91]. In ITER, Beryllium will be used on the first walls because the heat fluxes in those areas is much lower than on the divertor. Plus, Beryllium is a good oxygen trap. W is used on the divertor because of its many advantages : low erosion rate, high melting point so high heat tolerance, and low tritium retention because low erosion means low co-deposition. However, the radiation issue encountered 50 years ago comes back to the front.

1.5.1 The W central accumulation issue

W has an atomic mass A=184 and a charge Z=74.Even for ITER core temperatures, W does not get fully ionized. Therefore it radiates, mainly through dielectric recombination or line emission (see figure 1.9), plus a lower Bremsstrahlung contribution. W radiation depends on W and electron densities, and on a cooling factor which depends on the electron temperature and the W charge state. The cooling factor is calculated based on atomic data and on the contribution of the different collisional and radiative processes. The equation of the cooling factor is given in chapter 3 section 2. Figure 1.9 shows the cooling factor estimation from different models [108].

When W concentration exceeds a certain amount in the plasma core, typically around 2.10^{-4} radiative losses balance the heating supply, which can lead to disruption. Moreover, W can enter the central part of the plasma and disturb the plasma. W central accumulation was reported in JET [78] and ASDEX-Upgrade [97]. Fortunately it has been demonstrated that W levels can be controlled thanks to gas fuelling to reduce W sputtering at the divertor and other methods such as core heating with ECRH and ICRH [95]. Still, W central accumulation is a key issue to be adressed. W concentration will have to be kept below 10^{-5} in ITER in order to reach nominal fusion power [96]. Therefore, it is mandatory to understand W transport.

1.5.2 Properties of W transport

Ever since W central accumulation phenomenon was discovered, W transport became a central topic. Because of its mass and charge state, W has unique transport properties. This section gathers the main characteristics of W transport.

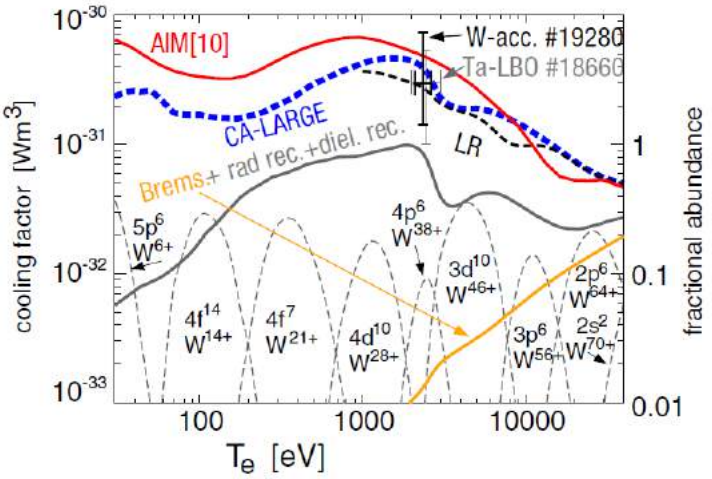

Figure 1.9 – W cooling factor depending on electron temperature for several calculations (full lines). Fractional abundances for several few ionization stages (dashed lines) [108]

W transport is a combination of neoclassical and turbulent components. Figure 1.10 shows the turbulent (in red) and neoclassical (in blue) contributions simulated respectively by GKW and NEO, for a JET-ILW hybrid pulse [10].

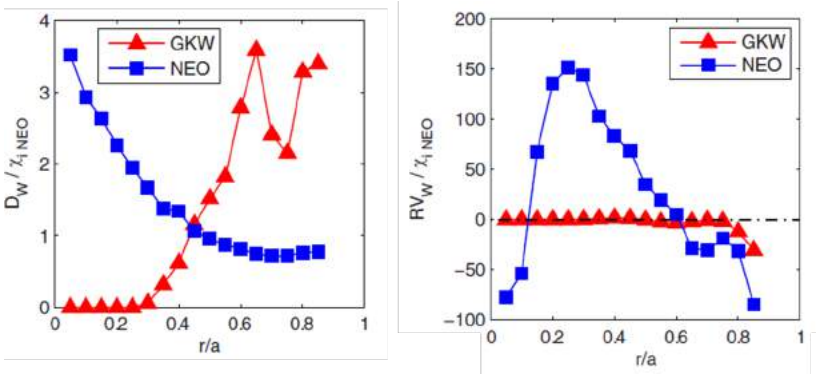

Figure 1.10 – Neoclassical (NEO) and turbulent (GKW) convective (right) and diffusive (left) contributions normalized to the neoclassical ion heat conductivity at 5.9s for JET-ILW pulse #82722. [10]

Starting with the diffusive term, the neoclassical contribution dominates on the inner half, while turbulent component dominates the outer half. Neoclassical transport dominates the convective part of the W flux. Especially, neoclassical convection is negative in the central part and at the edge, which drives W inward, i.e. towards the center. This figure illustrates that both turbulent and neoclassical transport must be accounted for when modeling W transport.

Poloidal asymmetries is another important feature of W transport. The W distribution can be described as in equation 1.7 from [28]. Equation 1.7 is a generalization of [140], which comes from the pressure balance equation in the

poloidal direction.

$$n_W(\theta) = n_{W0} \exp(-\frac{eZ\phi(\theta)}{T_i} + \frac{m_W\omega^2(R_{local}(\theta)^2 - R_0^2)}{2T_i}) \tag{1.7}$$

With n_{W0} the W density at the low field side, R_{local} is the local major radius and R_0 its value at the low field side, ω is the angular frequency, θ is the poloidal angle, Z is the W charge, m_W the W mass, and Φ the poloidally varying potential.

Only heavy impurities undergo poloidal asymmetries due to the charge Z and mass dependencies. Poloidal asymmetries can be caused by NBI [10, 28], which impacts the rotation ω in equation 1.7 and lead to a centrifugal acceleration effect. They can also be caused by Radio Frequency heating (ECRH/ICRH) [111, 19] which modifies the potential Φ. Poloidal asymmetries strongly increases neoclassical transport, up to a factor 10 in JET [10, 28]. Therefore they must be accounted for in integrated modeling. In chapter 2 section 3, an analytical formulation describing heavy impurity neoclassical transport in the presence of poloidal asymmetries is compared to numerical results from NEO.

MHD phenomena such as sawteeth and ELMs also impact W behavior. W production is mainly caused by erosion during ELMs [44], but ELMs also have a more positive impact since they also flush W out of the pedestal [43]. Sawtooth crashes flatten temperature and density profiles, which impact W transport. Periodic sawteeth seems to reduce W transport in the core.[76, 106]

In Alcator C-mod, experiments showed that with only RF heating [89] W central accumulation does not occur. This very encouraging phenomenon is most likely due to the lack of central fuelling and torque, which are mostly caused by the use of NBI. This assumption will be studied in our simulations in chapter 3 section 5.

Even in presence of NBI, the use of RF heating limits the W central density peaking both in ASDEX-Upgrade [11] and in JET. [60]

1.6 Integrated modeling

As seen in the previous section, many actuators are at play to model and understand W transport : neoclassical and turbulent transport, heating sources and radiation, MHD instabilities, W source... All these quantities impact each other through feedback loops and non-linear interplays. Therefore it is mandatory to model all these quantities self-consistently in order to get an accurate W transport prediction.

1.6.1 Operation of an integrated modeling tool

The use of an integrated modeling tool is mandatory in order to evolve many plasma quantities at the same time : main plasma and impurity transport (particles, heat and momentum), but also heating, radiation and plasma current.

Each plasma parameter, or module, is evolved by a specific code. Several codes are available per plasma parameter, so the user can choose the level of complexity needed for each module depending on the purpose of his/her study. An integrated modeling tool is at the same time very powerful and very fragile. Indeed, coupling many independent codes together brings all kinds of normalization adjustments and numerical stability issues. Setting up 5 or 6 codes together can take months and hundreds of iterations. Moreover, the CPU need of each module is limited by the fact that modeling 1s of plasma require each module to be called up to 10^4 times. For the integrated modeling simulations shown in chapter 3, simulating 1.5s of plasma took a week of computational time on 16 processors. Assuming that the turbulent transport module is called 10^4 times, it means that the transport code has 40s to cover all radial positions at each call. Figure 1.11 shows a cartoon of an integrated modeling tool.

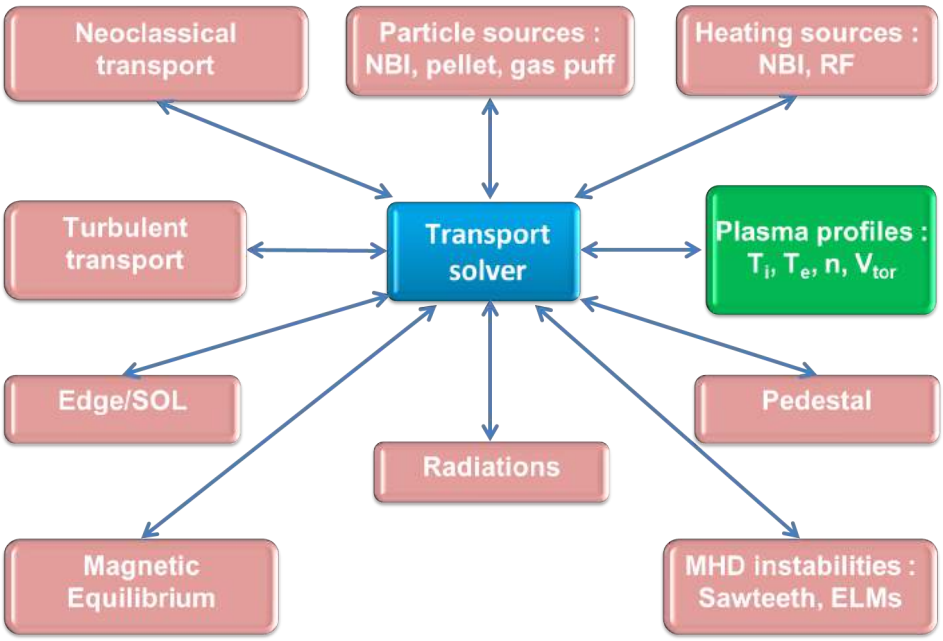

Figure 1.11 – Cartoon of an integrated modeling tool

The simulation starts at t_0 with the contents of the green box on the right side on figure 1.11 : initial ion and electron temperature profiles, electron and impurity densities, plasma rotation. Those profiles are fitted from experimental data and are distributed as inputs to several codes, via the transport solver, in blue on figure 1.11. Each code, represented by a magenta box, runs independently with the given set of input profiles. Then the codes feed back their outputs : transport coefficients, heat sources and losses and the updated magnetic equilibrium. The transport solver gathers those information, solves the transport equations 1.4 and 1.5 shown above in section 1.4.2 as well as the angular momentum equation [40], and updates the temperature, density and rotation profiles. Those profiles become the new input profiles at $t_0 + \Delta t$. The iteration goes on for several confinement times, making a self-consistent simulation of the plasma.

An integrated modeling tool can be run in two different modes : interpretive or predictive. Interpretive mode means that the plasma profiles (the contents of the green box : ion and electron temperatures, densities and rotation profiles) are not evolved by a code, but read from experimental fits. The outputs of such a simulation are the heat, particle and momentum transport coefficients. The predictive mode on the contrary uses only the density, temperature and rotation measurements are boundary conditions. The transport modules predict the fluxes and the outputs of such a simulation are the predicted density, temperature and rotation profiles.

1.6.2 State-of-art of integrated modeling tools for fusion

1.6.2.1 Short history of first principle transport modules in integrated modeling

Historically, the Weiland model [138] and GLF23 [136, 84] are among the first turbulent transport codes used in integrated modeling, evolving heat and particles [128, 57, 134]. Later momentum transport was implemented in TGLF [125] and QuaLiKiz [40].

Moving to neoclassical transport, NCLASS [74] is widely used in integrated modeling [30, 85] but, as seen above, does not account for poloidal asymmetry effects undergone by high-Z impurities. Self-consistent heavy impurity transport is now available thanks to the coupling of neoclassical codes accounting for poloidal asymmetries, such as NEO. Chapter 3 presents the first integrated modeling simulation, using first-principle based codes (QuaLiKiz and NEO), over multiple confinement times, flux driven, multi-channel (density, temperature, rotation) including W while accounting for poloidal asymmetry effects.

1.6.2.2 Different integrated modeling structures

Different integrated modeling platforms are currently used is fusion research. They all solve similar 1D transport equations, but using different approaches and assumptions.

TRANSP [103], developed at Princeton in the US from the 70s, is one of the first integrated modeling tools. One of its key elements is the Monte Carlo packages used for NBI modeling. This will be mentioned again in section 3 of chapter 3.

JINTRAC [33, 115] is developed at CCFE, in the United Kingdom. It includes 25 different modules that allow a complete description of a plasma, from the core to the Scrape-Off-Layer. JINTRAC corresponds to the modeling platform including the modeling of the SOL. If the modeling focuses on the plasma core, the integrated modeling platform is called JETTO. JINTRAC evolves ions and includes an impurity transport code, SANCO [4], which evolves heavy impurity radiations and charge states. It also includes first-principle based turbulent (GLF23, TGLF, QuaLiKiz) and neoclassical (NCLASS,NEO) transport codes.

Those elements makes JINTRAC the best integrated modeling tool to model self-consistently W transport in chapter 3.

ASTRA [5, 51] is developed in IPP Garching, in Germany. ASTRA evolves electron transport. NCLASS, NEO, TGLF and QuaLiKiz are also available in ASTRA.

CRONOS [12] was developed at CEA in France since 1999 and has been used to analyze data from several tokamaks including Tore Supra, JET and ASDEX-Upgrade. The strong point of CRONOS lies in the diversity of codes simulating heating systems. It also uses a user-friendly interface allowing the set up of all simulation parameters, from input profiles to post-processing. CRONOS, like ASTRA, evolves electrons.

The European Transport Simulator [39, 81] is the latest integrated modeling platform. Its goal is to homogenize and standardize the modules languages and normalizations, to allow more flexible, modular and machine agnostic workflows.

An integrated modeling tool can be used for many purposes : data or model validation, experiment analysis, diagnostic studies, scenario predictions. The accent can be put on any physical interest : core transport, MHD instabilities, SOL transport. JETTO, CRONOS and ASTRA are widely used to model core turbulent and/or neoclassical transport [10, 28, 14, 37]. Works such as [85] include simpler turbulent (GLF23) and neoclassical (NCLASS) transport but add complexity by coupling pellets, gas puff, SOL modeling, MHD instabilities and fuelling systems.

1.7 Purpose of this work

The goal of this work is to progress in the understanding of W central accumulation phenomenon. To do so, integrated modeling is used to reproduce a JET-ILW pulse, and study how accurate the best simulation can be compared with experiment. The main driver of W behavior, is W transport. NEO and QuaLiKiz codes, which are first-principle based neoclassical and turbulent transport codes, were recently coupled to JETTO. NEO and QuaLiKiz include treatment of poloidal asymmetries, which is essential for W transport. Therefore JETTO, also equipped with SANCO and heavy impurity radiation and charge state modeling, is currently the most advanced platform to model self-consistently the time evolution of W.

1.8 Conclusion of the chapter

The global energy demand is likely to further increase with time, therefore finding a sustainable, clean and safe energy source becomes an urgent problem. Thermonuclear fusion can, in theory, meet all these requirements and be a source of massive centralized electricity. Among the many challenges faced by fusion researchers, the W pollution and central accumulation is a key issue. Indeed, cur-

rent design entails W tiles for the most exposed plasma facing component. But since W is a heavy impurity it causes strong line radiation so W contamination must be lowered as much as possible. Further degradation related to W central density peaking, called accumulation, must be avoided. This destabilizes the reaction and strongly limits the current and future plasma performances. In order to control W pollution, the first step is to understand the mechanisms leading to the W accumulation, and identify the actuators responsible for it. Since W transport interplays with many plasma parameters, the problem requires a multi-physics approach and integrated modeling is the best tool currently available to address these issues. Modeling self-consistently the W behavior using first-principle based models is very new and was carried out for the first time during this PhD work, since it requires the coupling of several codes and many numerical adjustments. The goal of this work is to self-consistently reproduce 1.5s of a JET-ILW pulse with first-principle codes embedded in integrated modeling platform and identify the actuators leading to W accumulation.

The next chapter focuses on neoclassical transport of heavy impurities, which is a key element of W transport. Chapter 3 presents the integrated modeling simulations of the time evolution of W transport.

2High Z neoclassical transport : with and without the effect of poloidal asymmetries

2.1 Introduction to the chapter

The purpose of this chapter is to study high Z impurity neoclassical transport.

In a cylindrical plasma, collisional transport can be described using the approach called classical transport. This description is inappropriate in a toroidal plasma. Indeed, the toroidal geometry and the non-uniform magnetic field allow some particles to be trapped on the field lines (as explained on section 2.2.2), and their transport cannot be described using the classical transport approach. Therefore the collisional transport in a torus is known as neoclassical transport. [139] Neoclassical transport is negligible compared to turbulent transport for most of the species present in a tokamak, but can be dominant for high-Z impurities such as W.

This chapter is divided in two main parts. In the first one, the focus is neoclassical transport theory in absence of poloidal asymmetry of the impurity density, which is the most simple configuration. Neoclassical transport deals with transport by collisions, therefore at first collision frequencies are defined. Then a simplified version of the diffusion coefficient is presented, associated with the definitions of collisional regime and collisionality. This simplified diffusion coefficient expression is compared with the neoclassic code NEO [15, 17]. Finally an analytical formulation for the W neoclassical flux is given, along with poloidal velocity definitions and parametric dependencies of the W neoclassical flux. This part introduces an overview of the concepts used in neoclassical transport.

In the second part of the chapter, we study neoclassical transport taking into account poloidal asymmetries of the impurity density. Note that heavy impurities are more prone to such asymmetries in presence of rotation leading to centrifugal effects or in presence of RF heating. An analytical formulation to describe heavy impurity neoclassical transport in the presence of poloidal asymmetries in specific collisional regimes [9] is compared to numerical results from NEO. Finally the formula is tested inside an integrated tokamak transport platform (JETTO [115]) for two different JET-ITER Like Wall (JET-ILW) H-mode pulses and compared with NEO.

2.2 2. Neoclassical transport without poloidal asymmetries : definitions and generalities

In a tokamak plasma, neoclassical transport describes how particles, heat and momentum evolve thanks to collision. In the first section, the notion of collision is defined.

2.2.1 Collision times : definition

Since plasmas are made of charged particles, Coulomb collisions are considered here. Let us consider on figure 2.1 a configuration with an electron e^- passing by an ion i. We shall assume that the impact parameter b is large enough so the direction of the electron velocity, v, is deflected by a very small angle α.

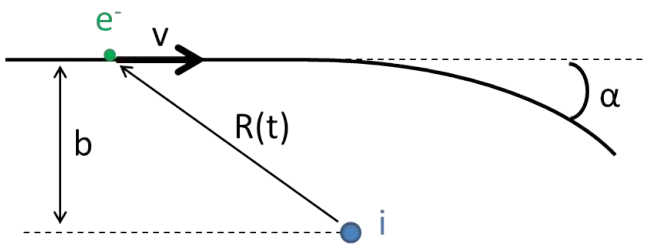

Figure 2.1 – Scheme of an electron-ion Coulomb interaction

The electron then performs a random walk with small modifications to its velocity, v, at every interaction. This creates a diffusion process, with a diffusion coefficient which will be discussed in section 2.2.3. The collision time is defined as "the time after which enough small-angle deflections have accumulated to cause a significant (say, 90 degrees) scattering of v." [69] The inverse of the collision time is called the collision frequency.

According to [94], in the case when particle "a" is lighter than particle "b", ie $m_a < m_b$, the collision frequency of the particle a on the particle b is :

$$\nu_{ab} = \frac{4}{3\sqrt{\pi}} \frac{4\pi n_b e_a^2 e_b^2 ln\Lambda}{(4\pi\epsilon_0)^2 m_a^2 v_{Ta}^3} = \frac{2^{1/2}}{12\pi^{3/2}} \frac{n_b e_a^2 e_b^2 ln\Lambda}{m_a^{1/2} T_a^{3/2} \epsilon_0^2} \tag{2.1}$$

with n_b the density of the particle "b", e_a and e_b respectively the charges of particles "a" and "b", $v_{Ta} = \sqrt{2T_a/m_a}$ is thermal velocity of the particle "a". $ln\Lambda = ln\lambda_D/\lambda_L$ the Coulomb logarithm with $\lambda_L = e_a e_b/4\pi\epsilon_0 kT_a$ the Landau length and $\lambda_D = \sqrt{\epsilon_0 kT_a/n_a e_a e_b}$ the Debye length, with k the Boltzmann constant, ϵ_0 the vacuum permittivity, n_a and T_a respectively the density and temperature of the species "a".

For $m_a = m_b$ and $n_a = n_b$ and $m_a > m_b$, equation 2.1 does not stricly applies and correction factors must be added, according to [94]. For $m_a = m_b$ and $n_a =$

n_b, $\nu_{aa} = (2^{-1/2})\nu_{ab}$. And for the case $m_a > m_b$, $\nu_{ab} = \nu_{ba}(\frac{m_b n_b}{m_a n_a})$.

The collision frequency depends on the density of the particle b. It also depends on the charge of both particles. e_a^2 and e_b^2 terms can become important for heavy impurities such as W. The collision frequency also depends on the mass of the moving particle a : the lighter it is, the higher the collision frequency. Finally, the collision frequency depends on the temperature of the particle a : the cooler it is, the higher the collision frequency.

Based on those equations, several collision frequencies between main ion (here Deuterium), electrons and W are plotted below on figure 2.2 depending on the W charge.

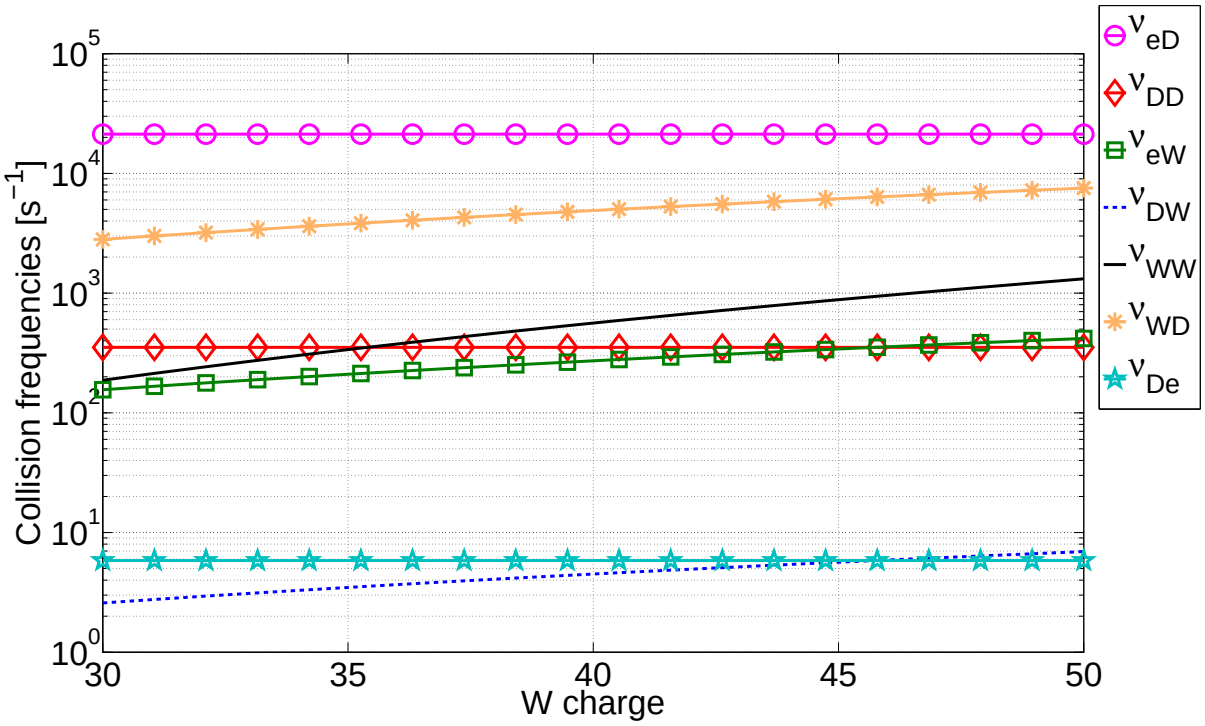

Figure 2.2 – Collision frequencies depending on W charge. $T_e = T_D = T_W = 2.5keV$ $n_D = 5.10^{19}m^{-3}$ $n_W/n_D = 10^{-5}$

The largest collision frequency is ν_{eD} because the electron mass is the smallest of the three species (at the denominator on equation 2.1) and the Deuterium density is the second biggest at play after n_e (on the numerator on equation 2.1). Note that $\nu_{eD}/\nu_{DD} = \sqrt{m_D/m_e} \approx 60$. Of all the collision frequencies implying W, the biggest is ν_{WD}, which increases with the W charge because of the e_W^2/m_W term in equation 2.1. ν_{WW} increases with $e_W^4/m_W^{1/2}$ so the slope of ν_{WW} is larger than the slope of ν_{WD}. However since $\nu_{WD}/\nu_{WW} = (\frac{e_D^2 n_D}{e_W^2 n_W})\sqrt{\frac{m_D}{m_W}} > 1$, ν_{WD} dominates.

2.2.2 Trajectories in a tokamak

Neoclassical transport is specific to the toroidal geometry, because of the properties of the particle trajectories in a toroidal magnetic field. In this subsection the tokamak geometry is detailed, the characteristics of the particle trajectories are detailed and the notion of trapped particles is defined.

2.2.2.1 Tokamak geometry

Figure 2.3 illustrates a poloidal cut of a circular plasma as an example. A tokamak geometry can be expressed using (r,θ,φ) coordinates, with r the radius, θ the poloidal angle and φ the toroidal angle. r varies from 0 to a the minor radius, and R is defined so that R=$R_0 + rcos(\theta)$ with R_0 the major radius. The symmetry axis represents the central solenoid.

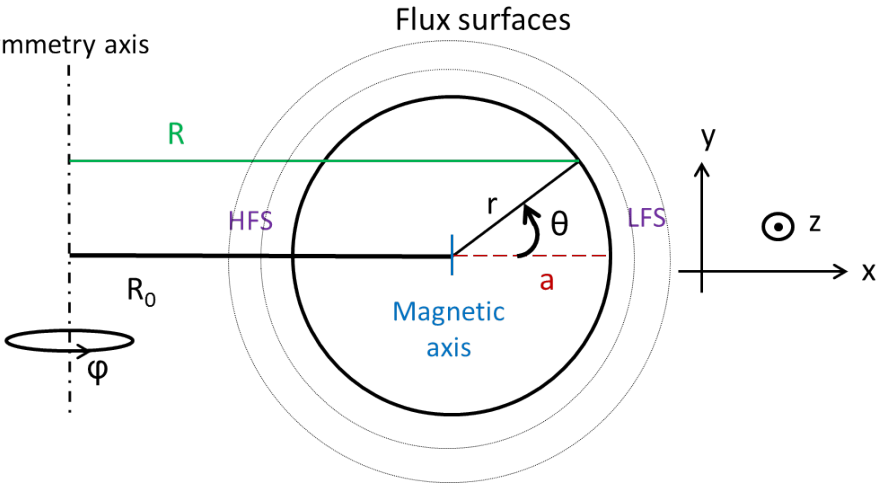

Figure 2.3 – Scheme of a poloidal cut of a tokamak presenting coordinates and notations

As seen in chapter 1, the helical magnetic field B that confines the plasma is a combination of the toroidal magnetic field B_φ generated by external coils, and a poloidal magnetic field B_θ created by the central solenoid. The safety factor characterizes how tight the magnetic fields are wrapped. At large aspect ratio ($R/r >> 1$) and with a circular plasma shape, q can be approximated as :

$$q = \frac{rB_\varphi}{RB_\theta} \tag{2.2}$$

q corresponds to the number of toroidal tours per poloidal tour a field line performs.

B_φ is generated by N external poloidal field coils in which a current I passes. Applying Maxwell-Ampere law, it gives $B_\varphi = \frac{\mu_0 IN}{2\pi R}$, with μ_0 the vacuum permeability. Therefore the magnetic field varies on a flux surface (dashed circle on

figure 2.3) with a minimum at $\theta = 0$ on the Low Field Side (LFS on 2.3), and a maximum at $\theta = \pi$ on the High Field Side (HFS on 2.3). This variation in B field, illustrated below on figure 2.4, has a great impact on particle trajectories and is the origin of trapped particles.

2.2.2.2 Particle motion and drift velocities

In this subsection, particle motion is explained, and drift velocities are defined.

Cyclotronic motion and guiding-center A particle "s" in a magnetic field $\vec{B}$, in absence of electric field, undergoes the Lorentz force and obeys the following motion equation :

$$\frac{d\vec{v_s}}{dt} = \frac{e_s B}{m_s}\vec{v} \times \vec{B} \tag{2.3}$$

with m_s and e_s respectively the mass and the charge of the particle "s", $\vec{v_s}$ its velocity.

In the configuration with $\vec{B}$ uniform and in the direction of the magnetic field (z direction illustrated on figure 2.3), the projection of equation 2.3 on (x,y,z) coordinates corresponds to :

$$\frac{dv_x}{dt} = \omega_{c,s}\vec{v_y} \qquad \frac{dv_y}{dt} = -\omega_{c,s}\vec{v_x}$$
$$\frac{dv_z}{dt} = 0 \tag{2.4}$$

with $\omega_{c,s} = \dfrac{e_s B}{m_s}$ the cyclotron frequency of the particle "s". For a Deuterium particle in a magnetic field B=5T, the cyclotron frequency is about 7.5MHz.

According to equation 2.4 the particle velocity in the z direction, along the magnetic field is constant. Another derivation and simple substitution in 2.4 allow to separate variables and solve the equations in x and y directions. Using $v_x = dx/dt$ and $v_y = dy/dt$ the solutions become :

$$x = -\rho_s cos(\omega_{c,s} t) \qquad y = \rho_s sin(\omega_{c,s} t) \tag{2.5}$$

with $\rho_s = \dfrac{m_s v_\perp}{e_s B}$ the Larmor radius of the particle "s". For a Deuterium particle with $v_{T,s} \approx v_\perp = 7.10^5 m/s$ and B=5T, the Larmor radius is around 2.5mm.

Overall, the particle draws a circular orbital motion around the magnetic field line. The radius of this motion is the Larmor radius, and the center of gyration of the particle is called the guiding-center. Guiding-center velocity has a parallel component $v_{G\parallel}$ and a perpendicular one $v_{G\perp}$. In addition to its gyration motion, the particle also has a constant velocity along the magnetic field line.

In order to simplify the particle motion for further calculations, the adiabatic theory is applied [118] since in a tokamak the magnetic field is considered varying slowly in time and space as compared respectively to the cyclotronic frequency and the Larmor radius. The adiabatic theory conditions can be written as :

$$\frac{d(\nabla B/B)}{dt} << \omega_{c,s} \qquad \rho_s \frac{\nabla B}{B} << 1 \tag{2.6}$$

Particle drifts On their path along a magnetic field line, the particles undergo large scale drifts that affect the perpendicular component of the guiding-center velocity. Note that the impact of the drifts is small compared with the parallel velocity of the particles. In this work three main drifts are introduced : the ExB drift, the ∇B drift and the curvature drift.

The ExB drift is caused by an electric field $\vec{E}$ perpendicular to the magnetic field. As a consequence the drift undergone by the particle is perpendicular to both fields. The ExB drift can be written as :

$$\vec{v}_{d,E\times B} = \frac{\vec{E} \times \vec{B}}{\vec{B}^2} \tag{2.7}$$

with $\vec{B}$ still along the magnetic field in the z direction and $\vec{E}$ in the y direction on figure 2.3. Note that the ExB drift does not depend on the particle charge.

The ∇B drift is caused by a gradient in the magnetic field perpendicular to the magnetic field. This drift, perpendicular to both the magnetic field and its gradient, in the "y" direction, drives electrons and ions in opposite directions. The curvature drift comes from a curvature of the magnetic field, causing the particles to undergo a centrifugal force. In the absence of current, it is convenient to combine ∇B and curvature drift :

$$v_{d,\nabla B} + v_{d,curvature} = \frac{\frac{1}{2}v_\perp^2}{\omega_{c,s}R} + \frac{v_\parallel^2}{\omega_{c,s}R} \tag{2.8}$$

2.2.2.3 Fraction of trapped particles

In a tokamak, particles follow the magnetic field lines and therefore undergo the poloidal variations of the magnetic field introduced in 2.2.2.1. As a consequence some particles with not enough parallel velocity can be trapped along the magnetic field. Starting from energy invariant applied for a particle :

$$v_\parallel^2 = \frac{2}{m}(\varepsilon - \mu B) \tag{2.9}$$

with $\mu = \frac{\frac{1}{2}mv_\perp^2}{B}$ and ε the kinetic energy, $v_\parallel$ and $v_\perp$ respectively the parallel and perpendicular components of the particle velocity.

One can see that if $\varepsilon < \mu B_{max}$ the parallel velocity $v_\parallel$ vanishes before $B(\theta) = B_{max}$. As seen above, B is maximal for $\theta = \pi$. Knowing that in the case of circular concentric flux surfaces with $\epsilon = r/R_0 << 1$ in the limit of large aspect ratio, B can be written as follows :

$$B(r,\theta) \simeq \frac{B_0 R_0}{R_0 + r cos\theta}; B_{max}(r, \theta = \pi) = \frac{B_0}{1-\epsilon} \approx B_0(1+\epsilon) \tag{2.10}$$

with $\epsilon = r/R_0$ the inverse of the aspect ratio.
Manipulating equation 2.9 gives :

$$\frac{\varepsilon}{\mu} = B + \frac{1}{2}\frac{m v_\parallel^2}{\mu} = B(1 + \frac{v_\parallel^2}{v_\perp^2}) \tag{2.11}$$

The quantity in equation 2.11 must be smaller than B_{max} for the particles to be trapped. It gives, at $\theta = 0$:

$$B(1 + \frac{v_\parallel^2}{v_\perp^2}) \leq B_0(1+\epsilon) \Leftrightarrow \frac{v_\parallel^2}{v_\perp^2} \leq \sqrt{2\epsilon} \tag{2.12}$$

This result is called the trapping condition, which determines the loss cone in the velocity space ($v_\parallel$,$v_\perp$) illustrated on figure 2.4. Trapped particles bounce along the magnetic field with a frequency ω_b and an orbit width δ_b, estimated below in 2.2.2.4.

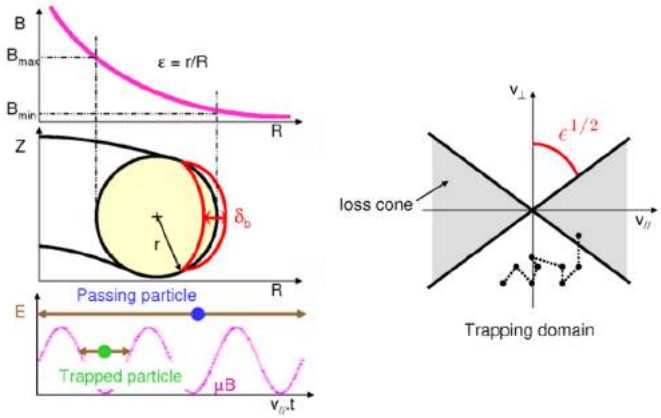

Figure 2.4 – Scheme from [118] of the characteristics of trapped particles and an illustration of the loss cone

We shall now calculate the fraction of trapped particles, which involves the expression of the distribution function f of the particles in the velocity space. In the simple case of a Maxwellian distribution, f can be written as :

$$f = (2\pi v_T^2)^{-3/2} e^{(\frac{-(v_\parallel^2 + v_\perp^2)}{2v_T^2})} \tag{2.13}$$

Then the fraction of trapped particles is :

$$f_t = 4\pi \int_0^{\infty} v_\perp dv_\perp \int_0^{v_\perp\sqrt{2\epsilon}} f dv_\parallel \tag{2.14}$$

The calculation, not detailed here, gives, in the limit of large aspect ratio tokamak, ie $\epsilon << 1$:

$$f_t \approx \sqrt{2\epsilon} \tag{2.15}$$

One can notice that the smaller ϵ is, the smaller is the number of trapped particles. It means that tokamaks with higher aspect ratios (ie with larger major radius for a given minor radius) will get less amount of trapped particles. For example, in JET, with $a = 0.96m$ and $R_0 = 2.96m$ at mid-radius the fraction of trapped particles borders up 55%, which illustrates that trapped particles represent a non-negligible quantity.

2.2.2.4 Banana width and characteristic frequencies of trapped particles

Banana width Once trapped, a particle bounces back and forth along the magnetic field line. Its trajectory follows a banana-like shape when projected on a poloidal cut, as seen on figure 2.4. The width of the trapped particle motion, called the banana width δ_b, can be calculated from the invariance of the toroidal kinetic momentum P_φ :

$$P_\varphi = m_s R v_\varphi + e_s \Psi \tag{2.16}$$

with m_s and e_s respectively the mass and the charge of the particle "s", v_φ its toroidal velocity and Ψ the toroidal flux function $\Psi = \int B_\theta . dS =$ and $\frac{d\Psi}{dr} \approx RB_\theta$.

At $\theta = 0$, the invariance of P_φ for the bounce motion is applied. Since $R >> \delta_b$ and using the fact that the toroidal velocity of a trapped particle reverses sign when moving from the inner to the outer side of the banana orbit, it gives :

$$\begin{aligned}
&P_\varphi(R) = P_\varphi(R + \delta_b) \\
\Leftrightarrow\ & m_s R v_\varphi + e_s \Psi(R) = -m_s (R + \delta_b) v_\varphi + e_s \Psi(R + \delta_b) \\
\Leftrightarrow\ & 2 m_s R v_\varphi + e_s \Psi(R) \approx e_s [\Psi(R) + \delta_b \frac{\Psi}{dr}] \\
\Leftrightarrow\ & 2 m_s R v_\varphi \approx e_s \delta_b R B_\theta \\
\Leftrightarrow\ & \delta_b \approx \frac{2 m_s R v_\varphi}{e_s R B_\theta}
\end{aligned} \tag{2.17}$$

We shall introduce the definition of the safety factor from equation 2.2 and the expression of the Larmor radius $\rho_s = \frac{m_s v_\perp}{e_s B_\varphi}$ from 2.5. Moreover, for trapped particle at $\theta = 0$, $v_\varphi \approx v_\parallel \approx v_\perp \sqrt{2\epsilon}$. Equation 2.17 becomes :

$$\delta_b = \frac{2m_s q v_\perp \sqrt{2\epsilon}}{e_s \epsilon B_\varphi}$$
$$\Leftrightarrow \delta_b \approx \frac{2q}{\sqrt{\epsilon}} \rho_s \tag{2.18}$$

The banana width is larger than the Larmor radius of the species "s".

Characteristic frequencies Two frequencies are characteristic of trapped particles. The first one is the frequency, called the bounce frequency, at which the trapped particle travels its banana orbit. For one half banana orbit, the trapped particle covers $L_\parallel = 2\pi q R$ at the speed $v_\parallel \approx v_\perp \sqrt{2\epsilon}$. The bounce frequency then corresponds to :

$$\omega_b = \frac{v_\parallel}{L_\parallel} = \frac{v_\perp \sqrt{\epsilon}}{\sqrt{2}\pi q R} \tag{2.19}$$

The "untrapping" frequency is another characteristic frequency for the trapped particles. Thanks to collisions, a trapped particle can be scattered out of the loss cone shown on figure 2.4. After a certain time τ, the trapping condition $v_\parallel^2 = v_\perp^2 2\epsilon$ is met and the particle is untrapped. τ can be calculated [109] and the "untrapping" frequency is then defined as $\nu_{eff} = 1/\tau$:

$$\nu_{eff} = \frac{\nu}{2\epsilon} \tag{2.20}$$

with ν the collision frequency defined in 2.2.1.

2.2.3 Neoclassical transport : effective diffusion coefficient and collisional regimes

As seen above in section 2.2.1, in neoclassical transport, particles are assumed to perform a random walk ruled by collisions, which creates a diffusion process. We shall now focus of this diffusion process and the expression of the diffusion coefficient.

Let us consider a configuration illustrated on figure 2.5 of free electrons in a magnetic field, in a slab geometry. One can consider electrons in rotation of the order of their Larmor radius (with homogenous and time independent B field).

Figure 2.5 – Scheme of two electrons

The effective diffusion coefficient D_{eff} can be defined as follows :

$$\Gamma_x = -D_{eff}\frac{dn}{dx} \tag{2.21}$$

The electron flux Γ_x (in the x direction here) corresponds to a number of particles per surface unit per second. It can also be written as :

$$\Gamma_x = \Delta n_x V_x \tag{2.22}$$

With Δn_x the variation of electron density : $\Delta n_x = n_x - n_{x+\Delta x}$ with $n_{x+\Delta x} = n_x + \frac{dn}{dx}\Delta x$. It gives $\Delta n_x = -\frac{dn}{dx}\Delta x$. Δx is the distance covered with one collision, in our example $\Delta x = \rho_e$ which is the electron Larmor radius. V_x corresponds to the speed of the random-walk of the electrons $V_x = \Delta x \nu_c = \rho_e \nu_c$. It gives :

$$\Gamma_x = -\Delta x^2 \nu_c \frac{dn}{dx} \tag{2.23}$$

Comparing equations 2.21 and 2.23 gives $D = \Delta x^2 \nu_c$ ie $D = distance^2 \times frequency$. The diffusion coefficient corresponds to the square of the distance covered during random walk, multiplied with the highest collision frequency (ie the one that generates the biggest transport).

In this section, the simplified approach to determine the diffusion coefficient is chosen, enabling to introduce collisional regimes and a first estimation of the diffusion coefficient.

2.2.3.1 Collisionality

There are three collisional regimes, each with a corresponding expression of the diffusion coefficient. The normalized collisionality is the parameter that determines the collisional regime. It corresponds to the ratio of the "untrapping" frequency (equation 2.19) over the bounce frequency (equation 2.20). The collisionality can be defined as follows, for a thermal species "s" ($v_T \approx v_\perp$) :

$$\nu_s^* = \frac{\nu_{eff,s}}{\nu_{bounce,s}} \approx \frac{qR}{v_{T,s}}\epsilon^{-3/2}\nu_s \tag{2.24}$$

with $v_{T,s}$ the thermal velocity of the species "s" and

$$\nu_s = \nu_{ss} + \sum_{s'} \nu_{ss'} \tag{2.25}$$

To calculate the collisionality of the species "s", all the collision frequencies involving "s" are summed according to 2.25, including the self-specie collision frequency. According to the ordering on figure 2.2, ν_{DD} is used to calculate ν_{DD}^* and ν_{WD} and ν_{WW} are summed to calculate ν_W^*. The notation ν_{DD}^* is used here to avoid confusion with section 2.2.3.6 where the D collisionality is calculated using ν_{De} and therefore written ν_{De}^*.

2.2.3.2 Weakly collisional : Banana regime

In this regime, trapped particles bounce many times before being untrapped, meaning that $\nu_{eff} << \nu_{bounce}$ or $\nu^* << 1$. In this configuration, the random walk covered by the particles is the banana width. The biggest collision frequency creating transport is ν_{eff} from equation 2.20. Moreover, in this regime, only trapped particles contribute to the transport, therefore the fraction of trapped particles from equation 2.15 needs to be introduced. According to the diffusion coefficient definition in 2.23 it gives :

$$D_{banana} = f_t \delta_b^2 \nu_{eff} = \frac{q^2 \rho_L^2}{\epsilon^{3/2}} \nu_s \tag{2.26}$$

In the banana regime, the diffusion coefficient increases with the collision frequency.

2.2.3.3 Highly collisional : Pfirsch-Schlüter regime

In this regime the mean free path of particles $l_{mfp} \approx v_T/\nu_s$ becomes much smaller than the transit length $\pi q R$, meaning that particles collide very early along their path. As a consequence, trapped particles do not have time to bounce. In terms of collisionality, the Pfirsch-Schlüter regime corresponds to :

$$\pi q R >> v_T/\nu_s \leftrightarrow \nu* >> \epsilon^{-3/2} \tag{2.27}$$

In this regime, the diffusion coefficient is not decomposed as $distance^2 \times frequency$ but rather as $velocity^2 \times time$.

Most particles are circulating and traveling along their field lines, creating a parallel transport with a parallel diffusion coefficient $D_\parallel \approx v_T^2 \nu_s$ [109]. The typical velocity of the random walk in this regime is dominated by the curvature drift introduced in section 2.2.2.2 equation 2.8. Therefore the velocity can be written as $v_D \approx v_\parallel^2/R\omega_{c,s} \approx \rho_s v_T/R$ with $\omega_{c,s} = e_s B/m_s$ the cyclotron frequency. The characteristic diffusion time $\tau_\parallel$ corresponds to the time needed for the particle to travel the distance $L_\parallel = 2\pi q R$ before a collision. Finally, it gives :

$$D_{PS} = v_D^2 \tau_\parallel \approx (q\rho_s)^2 \nu_s \tag{2.28}$$

In the Pfirsch-Schlüter regime, the diffusion coefficient does not depend on the inverse of the aspect ratio ϵ since trapped particles play no role in this regime.

2.2.3.4 Intermediary : Plateau regime

The intermediary regime is the plateau. It corresponds to $1 << \nu_* << \epsilon^{-3/2}$. Only a fraction ω_b/ν_{eff} of trapped particles travels several times their orbits before escaping. It gives :

$$D_{plateau} = \frac{\omega_b}{\nu_{eff}} D_{banana} = \frac{q v_T}{R} \rho_s^2 \tag{2.29}$$

In the plateau regime the diffusion coefficient does not depend on the collision frequency.

2.2.3.5 Collisionality example

To illustrate in which collisionality regimes Deuterium and W are, the profiles shown on figure 2.6 are used to calculate the D and W collisionalities on figure 2.7. Such temperature and density profiles are realistic tokamak values. All species are assumed to be at the same temperature.

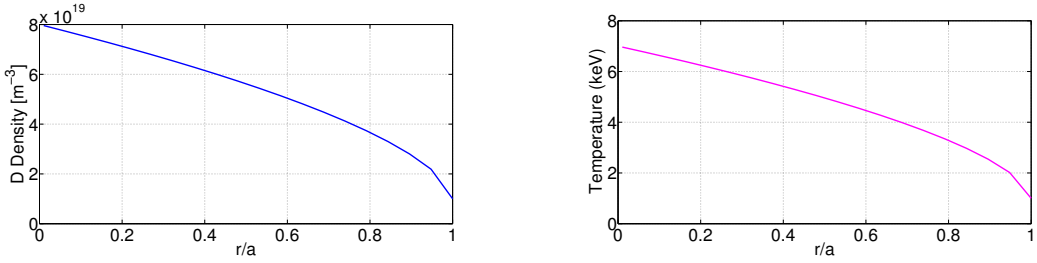

(a) n_D. (b) $Temperature$.

Figure 2.6 – Density and temperature profiles used to calculate collisionalities on figure 2.7

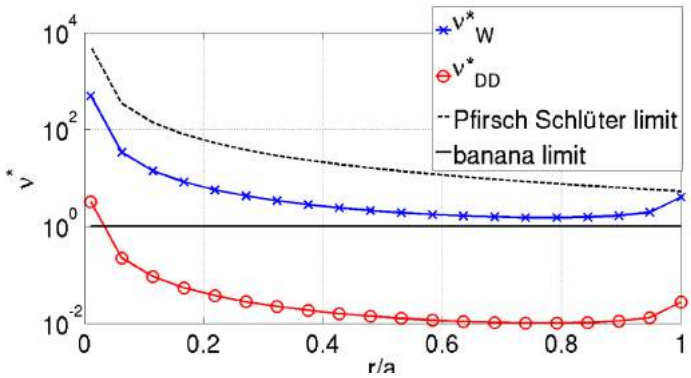

Figure 2.7 – W and D collisionalities versus r/a for the profiles given on figure 2.6. $R_0/a = 3$, $n_W/n_D = 10^{-5}$ and $Z_W = 40$, q=2

One can see on figure 2.7 that, for the chosen density and temperature profiles, D is in the banana regime for all radii except the first one. It means that most Deuterium particles are trapped and do not participate much to the neoclassical transport. W is in plateau regime for all radii and gets very close to Pfirsch-Schlüter regime at the very last radius. One could expect an heavy impurity such as W to be mainly in Pfirsch-Schlüter regime because of the e_s^2 and e_s^4 of the collision frequency expression on equation 2.1. However in our example the W is present as a trace, therefore its very small density balances its high charge state.

2.2.3.6 Comparison of the analytical formula for the diffusion coefficient vs NEO and NEO vs GYSELA

Now the approximative formulas for diffusion coefficient depending on the collisionality regimes are defined, they are compared with the neoclassical code NEO. Then in a second time the diffusion coefficient from NEO is compared with a gyrokinetic code, GYSELA [61].

Analytical formulas versus NEO The goal here is to compare the analytical formula for the diffusion coefficient in the different collisionality regimes (equations 2.28,2.26,2.29) with NEO results. The analytical formulas of the diffusion coefficient are applicable to any species, but we shall consider here a pure plasma with only one main ion, Deuterium, and electrons. Therefore the comparison focuses on the Deuterium diffusion coefficient. NEO, introduced in the previous chapter, is run with 19 Legendre and 10 Laguerre polynomials. In order to extract the diffusion coefficient from NEO outputs , for each set of inputs NEO is run twice, with two different Deuterium density gradients. The runs are called 1 and 2, with their associated fluxes Γ_1 and Γ_2, and their Deuterium density gradients $(\frac{R}{L_{ni}})_1$ and $(\frac{R}{L_{ni}})_2$ Assuming that equation 2.18 is a correct description of NEO results, the effective diffusion coefficient D_D can be isolated as shown on equation 2.30 :

$$D_D = \frac{R}{n_i} \frac{\Gamma_2 - \Gamma_1}{(\frac{R}{L_{ni}})_2 - (\frac{R}{L_{ni}})_1} \tag{2.30}$$

with $\frac{R}{L_{ni}} = -\frac{R\nabla n_i}{n_i}$. This method will be used again in section 3.

Figure 2.8a shows the Deuterium diffusion coefficient isolated from the NEO results in blue and compared with the analytical formulas in magenta for the different collisionality regimes. The vertical lines correspond to the collisionality regime limits : banana/plateau limit at $\nu^* = 1$ and plateau limit at $\nu^* = \epsilon^{-3/2}$. Figure 2.8b is a zoom of the banana area.

When studying the diffusion coefficient, self-species collisions can not be used to calculate the collisionality because they do no contribute to the transport of the considered species. Indeed, if for example two Deuterium particles collide, their velocities balance each other because of momentum conservation. Therefore in the case of the diffusion coefficient, the D collisionality ν^*_{De} is introduced, calculated with ν_{De} as ν_s in equation 2.24.

In order to scan the collisionality, the Deuterium density is scanned over two orders of magnitude. The density values are completely out of the experimental ranges, but as seen on figure 2.4 Deuterium barely gets out of the banana regime and the goal here is to test the validity of the analytical formulas against NEO over all collisionality regimes.

In the banana regime the formula over estimates NEO results up to a factor 10. Then NEO does not show any flat zone where, according to the analytical formula, the plateau regime should be. The lack of plateau area comes from

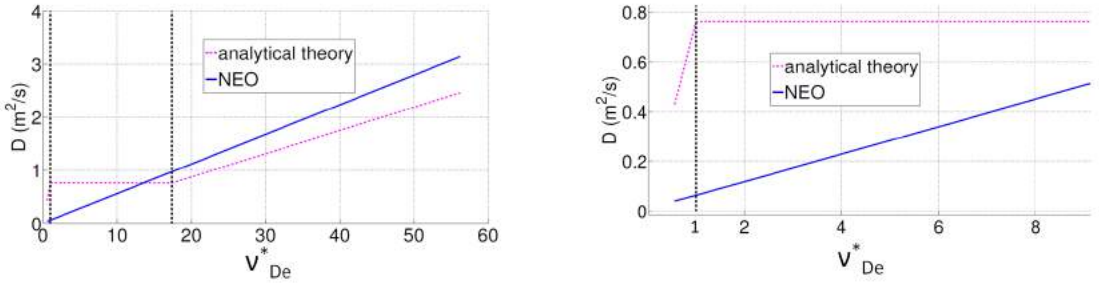

(a) full scan. (b) zoom of banana regime.

Figure 2.8 – Diffusion coefficient depending on collisionality for Deuterium. $n_D = 5.10^{21} \rightarrow 5.10^{23} m^{-3}$ $T_D = 1keV$ $r/a = 0.5$ $\epsilon = 0.15$

the fact that the theory assumes ϵ close to zero, which is not the case in our simulation ($\epsilon = 0.15$). Finally in the Pfirsch-Schlüter regime, the two curves show a much better agreement with a error reduced down to 20%.

Note that in the case of the pure plasma, because of the ambipolarity $\Gamma_i = \Gamma_e$ and the quasi-neutrality $n_e = Z_i n_i$, $D_e = D_i$.

Overall, the approximated formulae of the diffusion coefficient are not realistic, except in the Pfirsch-Schlüter regime.

NEO versus GYSELA GYSELA [61] is a non-linear 5D gyrokinetic code based on a semi-Lagrangian method and able to perform global, full-f and flux-driven simulations. A reduced and linearized multi-species collision operator has been recently implemented [49], so that both neoclassical and turbulent transport channels can be treated self-consistently on an equal footing. Therefore it is interesting to compare NEO and GYSELA on the neoclassical transport coefficients. Figure 2.9 shows GYSELA and NEO results depending on the collisionality for three species : Carbon, Helium and W, with the collisionality regimes. NEO is run with adiabatic electrons to match GYSELA electrons modeling, 19 Legendre and 10 Laguerre polynomials, but NEO can also be ran with kinetic electrons. As discussed later on 2.12, the kinetic electrons setting starts to impact NEO results when D is away from the banana regime, which is not the case here. The parameters values are summarized in Table 2.1.

Species	D	He	C	W
Collisionality ν^*_W	0.1	0.4	2.1	23.6
Concentration c_z	1	2.10^{-4}	10^{-5}	4.10^{-6}

Table 2.1 – Collisionality and concentration of the 4 species at r/a=0.5 of the NEO/GYSELA simulations. q=1.75, s=0.4, T=2.91keV, $n_D = 2.10^{20}$, $a/L_n = 0.031$, $a/L_T = 0.303$

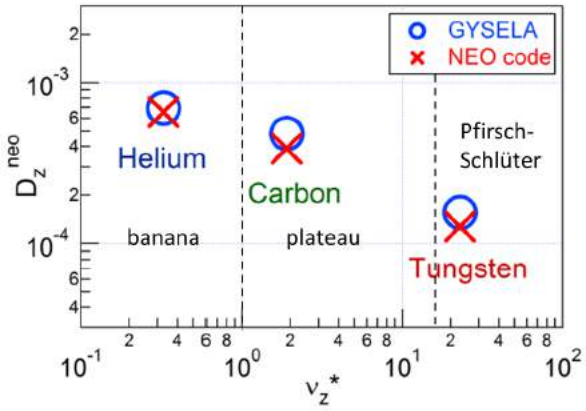

Figure 2.9 – Diffusion coefficient of 3 impurities (He, C and W) in a Deuterium plasma versus the impurity collisionality ν_Z^* . GYSELA (circles) NEO (crosses) with the zeroth-order Hirshman-Sigmar collision operator [17])

One can see that the code results are very close, with the best result at low collisionality for Helium. [49]

2.2.4 Neoclassical fluxes and poloidal velocity

Now the simplified expression of the effective diffusion coefficient has been studied, in this section the full analytical expression of the neoclassical particles fluxe is estimated. In this process the poloidal velocity is also discussed.

The calculation starts from the fluid momentum equation (equivalently called the force balance equation) :

$$n_s m_s \frac{d\vec{v_s}}{dt} = e_s n_s (\vec{E} + \vec{v_s} \times \vec{B}) - \vec{\nabla} p_s - \vec{\nabla} \bar{\pi}_s - \sum_{s \neq s'} n_s m_s \nu_{ss'} (\vec{v_s} - \vec{v_s'}) \qquad (2.31)$$

Where n_s, m_s, e_s, v_s, p_s, π_s, are respectively density, mass, charge, velocity, pressure and stress tensor associated with the species s. It is assumed that the plasma has a circular shape with a large aspect ratio, at a stationary state. The considered species are Deuterium as main ion, electrons and a trace impurity Z.

The projection of the stress tensor in the radial direction is negligible. In the toroidal direction it equals zero because of the axisymmetry. In the parallel direction it gives [64] :

$$u_{\parallel} \cdot \nabla \pi_s = n_s m_s \mu_s (v_{s\theta} - k_s \frac{\nabla T_s}{e_s B_\varphi}) \qquad (2.32)$$

with ν_s the collision frequency, k_s a function which will be determined later. Finally $\mu_s = \zeta q / \sqrt{\epsilon}$ with ζ constant and $u_{\parallel}$ the parallel velocity. The left hand part of equation 2.31 equals zero because we chose a stationary state and we

assume that the fluid velocity is smaller than the sound speed. Now we project equation 2.31 in radial (equation 2.33), parallel (equation 2.34) and toroidal (equation 2.35) directions :

$$0 = e_s n_s (E_r + v_{s\theta} B_\varphi - v_{s\varphi} B_\theta) - \nabla p_s \tag{2.33}$$

$$0 = e_s n_s E_\parallel - \mu_s n_s m_s (v_{s\theta} - k_s \frac{\nabla T_s}{e_s B_\varphi}) - \sum_{s \neq s'} n_s m_s \nu_{ss'} (\vec{v_{s\parallel}} - \vec{v_{s'\parallel}}) \tag{2.34}$$

$$0 = e_s n_s E_{ind} + e_s \Gamma_s B_\theta - \sum_{s \neq s'} n_s m_s \nu_{ss'} (\vec{v_{s\varphi}} - \vec{v_{s'\varphi}}) \tag{2.35}$$

We assume that $E_\parallel = E_{ind}$ (with E_{ind} the electrostatic field). It is interesting to notice that if we sum equation 2.35 over all the species, action-reaction principle makes the collision term to vanish, and electroneutrality causes the first term to vanish also. It leaves us with the ambipolarity constraint :

$$\sum e_s \Gamma_s = 0 \tag{2.36}$$

If we subtract equation 2.35 and equation 2.34 and assuming that $v_{s\varphi} - v_{s'\varphi} \approx v_{s\parallel} - v_{s'\parallel}$, it gives the flux expression :

$$\Gamma_s = -\frac{q\mu_s}{\epsilon} \frac{n_s m_s}{e_s B_\varphi} (v_{s\theta} - k_s \frac{\nabla T_s}{e_s B_\varphi}) \tag{2.37}$$

$v_{s\theta}$ is the poloidal velocity which needs to be determined.

2.2.4.1 Poloidal velocity

To estimate the poloidal velocity, equation 2.34 is summed over all the species. It gives :

$$\sum \mu_s n_s m_s (v_{s\theta} - k_s \frac{\nabla T_s}{e_s B_\varphi}) = 0 \tag{2.38}$$

The electron contribution is considered to be negligible because $m_e << m_D$ and $\mu_e \approx \mu_D$. The impurity contribution is also negligible because $n_Z << n_D$. Only Deuterium is left, leading to :

$$v_{D\theta} = k_D \frac{\nabla T_D}{e_D B_\varphi} \tag{2.39}$$

The value of the coefficient k_D varies depending on the collisional regime (1.17 for banana regime, -0.5 for plateau and -2.1 for Pfirsch-Schlüter). However these values correspond to $\epsilon << 1$ and are asymptotical. Hinton and Hazeltine created an interpolation formula (eq 6.(135) of [71]) for a species "s" :

$$k_{s,banana} = \frac{1.17 - 0.35\sqrt{\nu_s^*}}{1 + 0.7\sqrt{\nu_s^*}} \tag{2.40}$$

In the case of the Deuterium, the collisionality used in this formula is ν^*_{DD}. This formula is valid for banana and plateau regimes. For the Pfirsch-Schlüter regime, the formula (eq 6.(136) of [71]) is applied :

$$k_{s,PS} = \frac{k_{s,banana} - 2.1\nu_s^{*2}\epsilon^3}{1 + \nu_s^{*2}\epsilon^3} \tag{2.41}$$

To calculate the impurity velocity, equation 2.33 is written for the impurity and Deuterium :

$$\begin{cases} E_r + v_{Z\theta}B_\varphi - v_{Z\varphi}B_\theta - \dfrac{\nabla p_Z}{e_Z n_Z} = 0 \\ E_r + v_{D\theta}B_\varphi - v_{D\varphi}B_\theta - \dfrac{\nabla p_D}{e_D n_D} = 0 \end{cases} \tag{2.42}$$

Assuming that $v_{Z\varphi} \approx v_{D\varphi}$ and $T_D \approx T_Z$ it gives :

$$\begin{aligned} v_{Z\theta} &= v_{D\theta} + \frac{1}{B_\varphi}\left(\frac{\nabla p_Z}{n_Z e_Z} - \frac{\nabla p_D}{n_D e_D}\right) \\ \leftrightarrow v_{Z\theta} &= \frac{T_D}{e_D B_\varphi}\left[\frac{e_D}{e_Z}\frac{\nabla n_Z}{n_Z} - \frac{\nabla n_D}{n_D} + (k_D - 1 + \frac{e_D}{e_Z})\frac{\nabla T_D}{T_D}\right] \end{aligned} \tag{2.43}$$

The Hinton-Hazeltine analytical expression of the impurity poloidal velocity can now be compared with NEO.

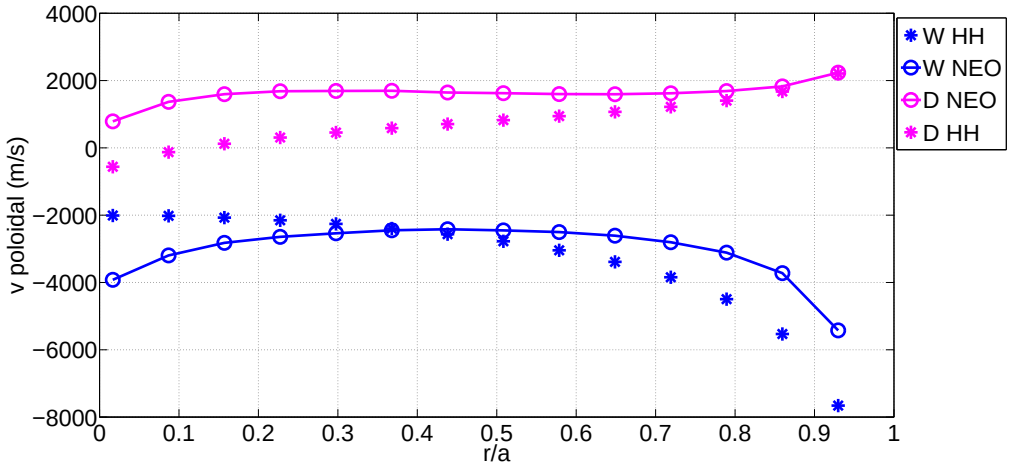

Figure 2.10 – Poloidal velocities depending on r/a. Based on profiles from figure 2.6. W in blue, D in magenta. NEO (circles) Hinton-Hazeltine from [71] (asterisks)

The velocities are calculated based on the profiles on figure 2.6. Let us first look

at the Deuterium in magenta. As seen on figure 2.7, the D first point is in plateau regime and the rest of the profile is in banana regime. From r/a=0-0.2, Hinton-Hazeltine formula (magenta asterisks) interpolates smoothly between the two regimes and from r/a=0.2 the two curves agreement improves towards the edge with Deuterium deeper in banana regime. The largest error (up to 80% in absolute values) between NEO and Hilton-Halzetine occurs for the first points, where the signs disagree.

For the W, NEO comes closer to Hinton- Hazeltine until r/a=0.5. Then the Hilton-Hazeltine formula over estimates NEO up 50%.

Overall Hinton-Hazeltine remains significantly different with respect to NEO, with absolute errors up to 80% and sign difference.

2.2.4.2 Particle fluxes

Thanks to the poloidal velocity expression, the analytical formula of the impurity flux from 2.37 can be finally determined.

$$\Gamma_Z = -D_Z \nabla n_Z + V_Z n_Z \tag{2.44}$$

with

$$\begin{cases} D_Z = \frac{q}{\epsilon} \mu_Z \rho_Z^2 \nu_Z D \\ V_Z = -Z D_Z [\frac{\nabla n_D}{n_D} + (1 - k_D + \frac{k_Z - 1}{Z}) \frac{\nabla T_D}{T_D}] \end{cases} \tag{2.45}$$

with $Z = e_Z / e_D$. But this formula is not valid in Pfirsch-Schlüter regime. [64]

2.2.4.3 Impurities

According to [94] the impurity neoclassical flux can be written as below, in the Pfirsch-Schlüter regime only :

$$\Gamma_Z = \frac{q^2 Z D_c n_Z}{R} [K(\frac{1}{Z} \frac{R}{L_{n_Z}} - \frac{R}{L_{n_i}}) - H \frac{R}{L_{T_i}}] \tag{2.46}$$

with

$$\begin{cases} D_c = \rho_D^2 \nu_{DD} \\ K = 1 - \dfrac{0.52\alpha}{0.59 + \alpha + 1.34 g^{-2}} \\ H = -0.5 + \dfrac{0.29 + 0.68\alpha}{0.59 + \alpha + 1.34 g^{-2}} \\ \alpha = \dfrac{n_Z Z_Z^2}{n_D Z_D^2} \\ g = \nu_D^* \epsilon^{3/2} \\ \nu_D^* D = \dfrac{\nu_{DD} q R}{v_{TD} \epsilon^{3/2}} \\ \nu_{DD} = \dfrac{4}{3\sqrt{\pi}} \dfrac{4\pi n_D e^4 ln\Lambda}{m_D^2 v_D^3} \\ \dfrac{R}{L_X} = -\dfrac{R \nabla_r X}{X} \end{cases} \tag{2.47}$$

Two coefficients apply, H and K, respectively on the ion density gradients (main ion i and impurity Z) and on the main ion temperature gradient. These coefficients depend on the impurity concentration and charge, as well as on the main ion collisionality. Indeed, having the main ion in banana regime implies that $\nu_D^* < 1$ so g term from equations 2.47 tends to 0, therefore $g^{-2} >> 1$. If the impurity concentration is low enough to remain in the trace limit (ie $\alpha << 1$) then the combination of the two assumptions (impurity trace and main ion banana regime) lead K to tend to 1 and H to tend to -1/2.

The impurity flux can be positive, meaning that the impurities are driven outward, or negative, with impurities driven inward. The sign of the flux depends on the three gradient lengths : the impurity density gradient length $\dfrac{R}{L_{n_Z}}$, the main ion density gradient length $\dfrac{R}{L_{n_i}}$, and the temperature density gradient length $\dfrac{R}{L_{T_i}}$. The main ion density gradient length is usually positive since the density profile is peaked. As a consequence, $\dfrac{R}{L_{n_i}} > 0$ which tends to drive the impurity inward ($\Gamma_Z < 0$) and is responsible for the phenomenon of impurity accumulation. This effect is more dramatic with an heavy impurity because of its Z dependence. This effect is limited by the counter acting impact of the temperature gradient length $\dfrac{R}{L_{T_i}}$. Again the temperature is usually peaked, leading to a positive temperature gradient length. With D in banana and the impurity in Pfirsch-Schlüter, the H coefficient is negative, so $H\dfrac{R}{L_{T_i}} < 0$ and tends to drive the impurity outward. This positive effect is called the temperature screening. However this positive effect is roughly cut by half because $|H| \approx 1/2$.

Figure 2.11 shows the W neoclassical flux versus r/a for the profiles from figure 2.6, therefore W is not in Pfirsch-Schlüter (see figure 2.7).

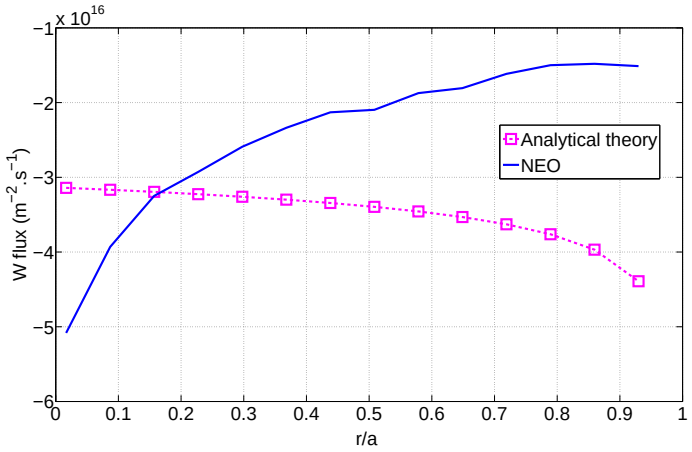

Figure 2.11 – W neoclassical flux depending on r/a. Based on profiles from figure 2.6

The W particle flux is negative at all radii, meaning that W is driven inward. NEO and the analytical formula show different trends, even if they have the same order of magnitude. An explanation could be that with the chosen profiles (figure 2.6) W is not in the Pfirsch Schlüter regime (see figure 2.7), while the analytical formula is valid in that regime only. Therefore it can be assumed that with W forced in deep Pfirsch-Schlüter regime, the fit between NEO and the analytical formula would agree better. However since increasing the W content would break the trace limit assumption, the exercise will not be tried here. It highlights the challenge to have both the W as a trace and in deep Pfirsch-Schlüter regime as assumed commonly in analytical derivations.

2.2.4.4 Temperature screening and pinch coefficients

In experimental plasmas, the impurities in the trace limit Pfirsch-Schlüter conditions are rarely simultaneously fulfilled (see figure 2.7 for example). This impacts the numerical value H and K respectively in front of $\frac{R}{L_{Ti}}$ and $\frac{R}{L_{ni}}$ inside equation 2.47, which is valid only in certain collisionality regimes according to [94]. Therefore the actual values of the H and K coefficients have to be tested against NEO.

A scan of the main ion (assumed to be Deuterium) collisionality was made with NEO. The Deuterium density is varied over a large range, in order to vary the D collisionality. Note that in order to reach Deuterium in deep Pfirch-Schlüter regime, unrealistic values of Deuterium densities are used, as for figure 2.8. The ratio $n_Z/n_D = 10^{-5}$ was kept fixed to maintain the impurity in the trace limit $\frac{n_Z Z^2}{n_D} = 1.2.10^{-3}$ with Z=34 the charge of W. Therefore, the W collisionality is varied from plateau to Pfirsch-Schlüter regimes. JET-like parameters are used based on pulse n°85308 time averaged over 10.35s-10.85s at mid-radius. The profiles can be seen on figures 2.14, the values are in the same range as figure 2.6.

Figure 2.12 shows the ratio H/K versus Deuterium collisionality ν_D^*, as it is not possible with NEO to extract H and K from the diffusion coefficient D_c. Indeed the theoretical formulation of D_c is only valid for deep Pfirsch-Schlüter regime, which makes it not reliable for a collisionality scan. On figure 2.12, NEO H/K is compared with Wenzel-Sigmar formula (equations 2.46 and 2.47 above) and with NCLASS ([74]). NCLASS is a neoclassical code based on the fluid moment approach with a simplified collision operator, and does not account for poloidal asymmetries. NCLASS uses the Hirschman-Sigmar collision operator , based on pitch angle scattering. Two NEO scans were made, one with adiabatic electrons, and the other with kinetic electrons.

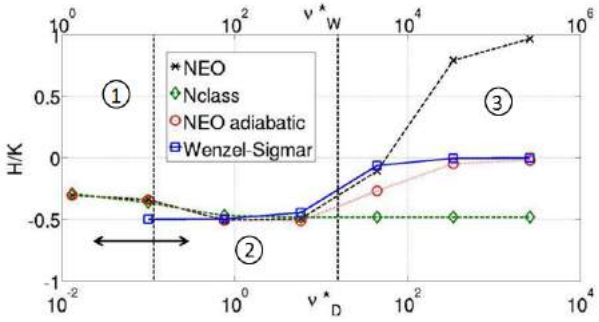

Figure 2.12 – H/K versus D and W collisionalities. Wenzel-Sigmar formulation equations 2.46 and 2.47 (solid line squares) NCLASS (diamonds) NEO kinetic electrons (dashed line and crosses) and NEO with adiabatic electrons (dot line and circles). The arrow shows JET-like core values range, see figure 2.14 below. The parameters used for this scan are : r/a=0.5, $\varepsilon = 0.16$, Z=34, $T_i = T_e = 2.1keV$, q=1.18, R=2.98, $\alpha = 1.2.10^{-3}$, $n_D = 10^{19} \rightarrow 3.10^{24}$. Left vertical line : plateau/Pfirsch-Schlüter regime limit for W. Right vertical line : plateau/Pfirsch-Schlüter regime limit for D

Figure 2.12 can be divided in three zones, separated by vertical dashed lines which correspond to change of collisional regime. The left one indicates that W enters Pfirsch-Schlüter regime, and the right one that Deuterium enters Pfirsch-Schlüter regime. Below $\nu_D^* = 0.1$ in the far left zone n°1, Deuterium is in the banana regime and W is in plateau. When $0.1 < \nu_D^* < 15$ in the central zone n°2, W is in Pfirsch-Schlüter regime and D is in banana/plateau regime. Above $\nu_D^* > 15$ in the far right zone n°3, both species are in Pfirsch-Schlüter regime. Core range values for the JET-ILW case studied and described in section 2.3.3.1 covers zones one and two, with W in plateau/Pfirsch-Schlüter, and D in banana/plateau (see figure 2.15). One can start with the first zone : D banana and W plateau. When the W is in plateau, Wenzel-Sigmar equation 2.46 is not applicable. In this zone, both NEO and NCLASS agree very well with each other. In the second zone, D is banana/plateau and W is in Pfirsch-Schlüter, Wenzel-Sigmar equation 2.46 is applicable. The H/K value derived in Wenzel-Sigmar in [94] equals -1/2, NEO

and NCLASS first converge towards -1/2. But as ν_D^* increases, NCLASS remains at -0.5 while H/K from [94] and both NEO curves move away from -0.5. It means that when approaching Pfirsch-Schlüter, NCLASS is no longer an adequate model. In the third zone, both species are in Pfirsch-Schlüter : in this configuration, according to [116] H/K derived in [94] tends to zero. NEO curve with adiabatic electrons goes to zero, but the NCLASS curve remains at -0.5, and NEO with kinetic electrons goes up to 1. NCLASS behavior comes from the fact that it uses a collision operator which does not include energy scattering, which makes it non-relevant with D in Pfirsch-Schlüter. NEO with kinetic electrons differs from the adiabatic electron case due to the electron coupling. Indeed, at low impurity density, the electron collision frequency with the main ions (i.e. ν_{eD}) is larger than the impurity collisional coupling with the main ions (i.e. ν_{DW}), as seen on figure 2.2. This explains the difference betwen kinetic and adiabatic electron NEO runs. NEO with kinetic electrons is the most physical result.

Two conclusions can be made out of this study of H/K term over Deuterium collisionality. First, typical tokamak collisionality values cover a zone where |H/K| can be lower than 0.5. Secondly, NEO and NCLASS give the same results within the experimental parameter range. This observation will be useful in section 2.3.

2.2.4.5 Parametric dependencies

In order to have a better understanding of the impact of the gradient lengths on the W flux, each gradient is scanned while keeping the others fixed : $-\nabla T_i/T_i$ on figure 2.13a, $\nabla n_D/n_D$ on, figure 2.13b and n_W/n_D on figure 2.13c. The goal is to know for which range of values the flux will be positive, leading to an outward W flux. The analytical formula 2.43 is also compared with NEO in this study.

One can see on figure 2.13a that the larger the T_D normalized gradient is, the larger the flux is. It means that the direction of the flux depends on the stiffness of the temperature gradient. Note that the analytical theory and NEO differs from up to a factor 2, even if the tendencies are similar. In particular the analytical W flux changes sign earlier than NEO, meaning that the Pfirsch-Schlüter analytical formula overestimates the temperature screening phenomena.

For the $-\nabla n_D/n_D$ scan on figure 2.13b, the positive values are reached by NEO when the gradient is close to zero. It means that we need a flat Deuterium density profile in order to keep the W out of the plasma. The analytical theory and NEO differs from up to 50%, even if the tendencies are similar, and NEO is a bit more pessimistic than the analytical formula.

Finally, on the n_W/n_D scan on figure 2.13c, NEO results show that the greater the W quantity, the more inward the flux is. If there is more W coming in, it means it will increase even more the W concentration, creating a feedback loop with a negative impact on plasma confinement and stability. The error between the analytical formula and NEO reaches 60%.

Overall, to avoid W accumulation the best configuration contains a stiff main ion temperature gradient and a flat main ion density gradient. Moreover, the

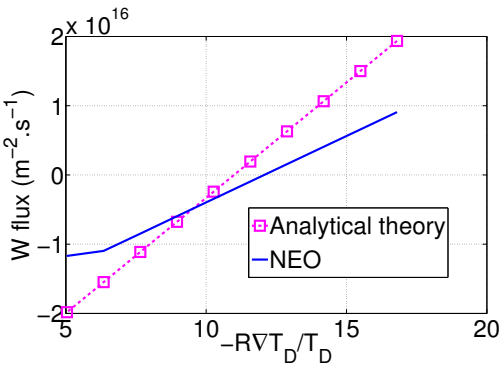

(a) Γ_W vs $-R\nabla T_D/T_D$.

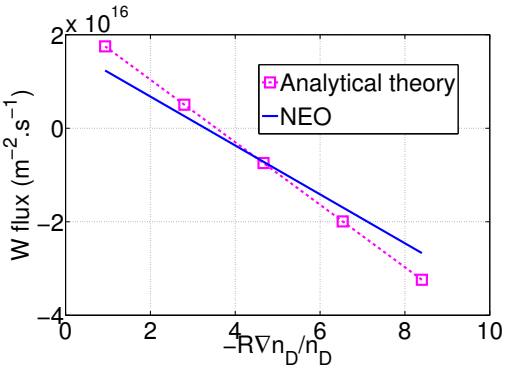

(b) Γ_W vs $-R\nabla n_D/n_D$.

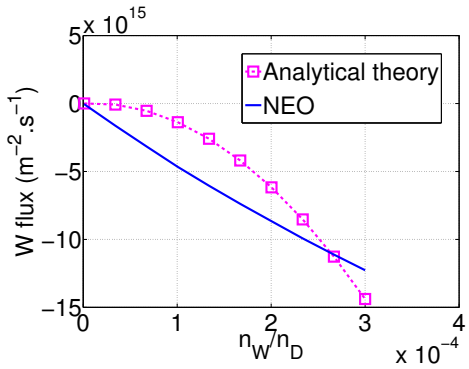

(c) Γ_W vs n_W/n_D.

Figure 2.13 – Γ_W dependng on $-R\nabla T_D/T_D$, $-R\nabla n_D/n_D$, n_W/n_D without rotation $T_D = T_W$=1,4 keV r/a=0,79 $n_D = 3,4.10^{19}m^{-3}$, $Z_W = 40$

calculation of the W flux requires the use of NEO or NCLASS rather than the analytical estimation.

In this section, neoclassical transport was described in absence of poloidal asymmetries. In the next section, the impact of poloidal asymmetries on heavy impurity is taken into account and an analytical formula is introduced and compared with NEO. Finally the formula is tested inside JETTO for two different JET-ITER Like Wall (JET-ILW) H-mode pulses.

2.3 Neoclassical transport with poloidal asymmetries : study of a generalized analytical formula

W transport is both turbulent and neoclassical. In the central region of JET core, W transport has been shown to be mostly neoclassical [73, 69, 6, 54, 10], whereas in the outer part the turbulent transport dominates. Due to its large mass A=184, W is subject to a strong centrifugal force when the plasma rotates. This causes poloidal asymmetry in W density. In presence of NBI momentum input, those asymmetries are shown to increase the neoclassical W transport by an order of magnitude in JET [10, 28]. Radio Frequency heating also impacts the poloidal distribution of W up to a factor 2 [111, 19]. NEO [16, 17] includes comprehensive treatments of poloidal asymmetries. However the computational cost of running NEO is of the same order of turbulent quasilinear codes such as QuaLiKiz [22] and TGLF [124] when embedded in integrated modeling platforms such as JETTO [115].

The goal of this section is to study an alternative solution applying an analytical formula that describes the impact of poloidal asymmetries on heavy impurity transport. Based on previous works such as [140, 70, 114] and especially [55], Angioni and Helander proposed such a formula in [9]. This formula, combined with the neoclassical code NCLASS [74] in which poloidal asymmetries are not included, could offer a faster option for integrated modeling. The Angioni Helander formula [9] derives the impurity neoclassical flux with a simplified collision model, valid for main ion in banana regime at low Mach number, impurity in trace limit and in collisional Pfirsch-Schlüter regime. These constraints are not simultaneously fulfilled for all radii in experimental plasmas. It is therefore essential to explore the validity domain of the analytical formulation accounting for poloidal asymmetries up to realistic ranges. In order to understand if an alternative to NEO exists to deal with poloidal asymmetries at a lower CPU cost, JET-ILW like parameters from H-mode plasmas are used as an illustration of such realistic conditions. This formula was tested out of its validity domain against NEO for several parameter scans, in order to test its robustness and its limits. At first it was noted that within the validity domain of the formula a factor had to be empirically adjusted. Then the modified formula was compared to NEO outside of its validity range, and it is found to remain valid outside its definition

domain. Indeed, considering main ions in the banana regime, it well reproduces NEO results whatever the collisionality regime of impurities, provided the poloidal asymmetry is not too large. Finally, the formula combined with NCLASS is used inside the transport solver JETTO to simulate a discharge, and then the W density profiles predicted are compared to the ones obtained with an integrated simulation with NEO, while gaining about a factor 1100 of CPU time.

The analytical formula and its limits are introduced in section 2.3.1 and are generalized in 2.3.2. In section 2.3.3 the formula is tested against NEO. Finally in section 2.3.4 the formula is tested inside JETTO for two different JET-ILW like H-mode pulses and compared with NEO.

This work has been submitted for publication to the journal Physics of Plasmas.

2.3.1 Analytical formula of the high Z neoclassical flux with poloidal asymmetries

Neoclassical impurity theory has been generalized to consider the case of poloidally asymmetric heavy impurity such as W [140, 114, 55, 56, 18, 9, 7]. The theory is valid whether the W localization is caused by centrifugal forces or RF induced temperature anisotropy. The impurity labeled Z has to stay in the trace limit ($\alpha = \frac{Z_Z^2 n_Z}{Z_i^2 n_i} << 1$). The impurity also has to be in the Pfirsch-Schlüter regime ($\nu_Z* >> \epsilon^{-3/2}$) while the main ion, labeled i, is in the banana regime ($\nu_i* < 1$). The normalized collisionality $\nu*$ is still defined as $\nu_s^* = \frac{\nu_s q R}{\upsilon_{T,s}\epsilon^{3/2}}$. For the main ion the dominant collisionality is ν_{ii}. With a simplified collision operator valid at large aspect ratio ($\varepsilon >> 1$), the neoclassical impurity transport can be written as follows (equation (2) of [7], recalled from [9]).

$$\frac{R\left\langle\Gamma_Z^{neo}\right\rangle}{\left\langle n_Z\right\rangle} = q^2 D_c Z\left[\left(\frac{1}{Z}\frac{R}{L_{nZ}} - \frac{R}{L_{ni}} + \frac{1}{2}\frac{R}{L_{Ti}}\right)P_A^{model} - 0.33 P_B^{model} f_c \frac{R}{L_{Ti}}\right] \quad (2.48)$$

with the purely geometric factors :

$$P_A^{model} = \frac{1}{2\varepsilon^2}\frac{\langle B^2\rangle}{\langle n_Z\rangle}\left[\left\langle\frac{n_Z}{B^2}\right\rangle - \left\langle\frac{B^2}{n_Z}\right\rangle^{-1}\right] \quad (2.49)$$

$$P_B^{model} = \frac{1}{2\varepsilon^2}\frac{\langle B^2\rangle}{\langle n_Z\rangle}\left[\frac{\langle n_Z\rangle}{\langle B^2\rangle} - \left\langle\frac{B^2}{n_Z}\right\rangle^{-1}\right] \quad (2.50)$$

The structure of equation 2.48 is very similar to the impurity transport flux without asymmetries derived above in equations 2.46 and 2.47 in section 2.2.4.3 from [94]. When comparing equations 2.47 and 2.48, one can recognize the diffusive term proportional to ∇n_Z, the neoclassical pinch driven by ∇n_i, both multiplied by the P_A^{model} factor. Concerning the temperature screening driven by ∇T_i,

two terms are contributing : the term without asymmetries multiplied by P_A^{model} to which a new term is added, proportional to P_B^{model}. This new P_B^{model} term decreases the impact of temperature screening. The P_A^{model} and P_B^{model} factors are both purely geometrical and one can notice that without poloidal asymmetries of the impurity density n_Z, i.e. $\langle n_Z \rangle = n_Z$, $P_A^{model} \to 1$ and $P_B^{model} = 0$ and one recovers Pfirsch-Schlüter W flux from equation 2.47 of [94]. In the case of strong asymmetries, P_A^{model} and P_B^{model} increase; it means that the impurity transport will be more sensitive to the main ion density gradient, and the benefits from temperature screening will be reduced.

2.3.2 Theoretical limits and implications of the formula

2.3.2.1 Symmetric neoclassical temperature screening and pinch coefficients

Equation 2.48 above from [7] is derived with the main ion in the banana regime, and heavy impurities in the Pfirsch-Schlüter regime. Heavy impurities must be present as a trace, i.e. $\alpha = \dfrac{Z_Z^2 n_Z}{Z_i^2 n_i} << 1$. The main ion are also assumed to remain subsonic, $M_i = \sqrt{m_i 2T_i}\omega R < 1$, where ω is an angular frequency of toroidal rotation. The impurity Mach number has no constraint, however one can notice that in present experiments with NBI [10] tungsten Mach number can be high, $M_W = M_i\sqrt{m_W/m_i} \geqslant 1$ (see figure 2.14c).

In experimental plasmas, the main ions in banana and impurities in the trace limit Pfirsch-Schlüter conditions are not always fulfilled (see figure 2.7 for example), whereas even in NBI JET cases the bulk ion Mach number remains subsonic. This impacts the numerical value 1/2 in front of $\dfrac{R}{L_{Ti}}$ inside equation 2.48, which corresponds to the H coefficient from equation 2.49 with the main ion in banana regime and the trace impurity in Pfirsch-Schlüter. But as seen in section 2.2.4.4, typical tokamak collisionality ranges values cover a zone where |H/K| can be lower than 0.5. It means that keeping the numerical value in equation 2.48 is not adequate to describe experimental plasmas. The H/K study also shows that NEO and NCLASS give the same results within the experimental parameter range. Therefore the combination of NCLASS with P_A and P_B formula (equations 2.48 2.49 2.50 and [74]) will be compared to NEO with poloidal asymmetries.

Therefore, we assume a generalisation of equation 2.48 as follows :

$$\frac{R\langle \Gamma_Z^{neo}\rangle}{\langle n_Z\rangle} = q^2 D_c Z \left[\left(K\frac{1}{Z}\frac{R}{L_{nZ}} - K\frac{R}{L_{ni}} - H\frac{R}{L_{Ti}}\right)P_A^{model} - H_0 f_C P_B^{model}\frac{R}{L_{Ti}}\right] \tag{2.51}$$

In the limit of main ion in banana regime and W in the trace limit and Pfirsch-Schlüter regime, K=1, H=-0.5 and $H_0 = 0.33$ and equation 2.48 is recovered. The numerical value 0.33 associated with P_B term in equation 2.48 is also valid only for W in Pfirsch-Schlüter. But as shown later in figure 2.15 W is mainly in

plateau for the studied JET pulse. Therefore in equation 2.51 the 0.33 value is generalized to an H_0 numerical term that will be empirically adjusted based on NEO results.

2.3.2.2 Extracting P_A and P_B terms from NEO outputs

In order to explore the validity of equation 2.51, one needs to extract the transport coefficients from NEO outputs, and then deduce P_A and P_B terms calculated with NEO and compare them to their theoretical expressions (equations 2.49 and 2.50). For clarity, equation 2.51 is re-written : the idea is to gather the terms respectively in front of densities and temperature gradients. The general version of the flux equation, written in equation 2.52 below is the starting point. The impurity flux is expressed as the sum of a diffusion term and a convective part. The diffusion coefficient is D_{asym}^{model} and the convection velocity coefficient is identified as V_{asym}^{model}. The index asym stands for asymmetric, i.e accounting for the effects of poloidal asymmetries. "model" means that the coefficients are based the analytical derivation of P_A and P_B (equations 2.49 and 2.50).

$$\left\langle \Gamma_{asym,Z}^{model} \right\rangle = \frac{D_{asym}^{model} n_Z}{R} \left(\frac{R}{L_{nZ}} + \frac{V_{asym}^{model} R}{D_{asym}^{model}} \right) \tag{2.52}$$

with the pinch velocity term defined as

$$V_{asym}^{model} R = R V_{N,asym}^{model} + R V_{T,asym}^{model} \tag{2.53}$$

We define $V_{N,asym}^{model}$ and $V_{T,asym}^{model}$ as the convection velocities respectively proportional to $\frac{R}{L_{ni}}$ and $\frac{R}{L_{Ti}}$:

$$V_{N,asym}^{model} = D_{asym}^{model} C_{N,asym}^{model} \frac{1}{L_{ni}} \tag{2.54}$$

$$V_{T,asym}^{model} = D_{asym}^{model} C_{T,asym}^{model} \frac{1}{L_{Ti}} \tag{2.55}$$

By identification with equation 2.51 the coefficients D_{asym}^{model}, $C_{N,asym}^{model}$ and $C_{T,asym}^{model}$ can be written as follows :

$$D_{asym}^{model} = q^2 D_c K P_A^{model} = D_{sym}^{model} P_A^{model} \tag{2.56}$$

$$C_{N,asym}^{model} = C_{N,sym}^{model} = -Z \tag{2.57}$$

$$C_{T,asym}^{model} = -Z\left(\frac{H}{K} + \frac{H_0 f_C P_B^{model}}{K P_A^{model}}\right) = C_{T,sym}^{model} - \frac{Z H_0 f_C P_B^{model}}{K P_A^{model}} \tag{2.58}$$

In equation 2.58 $f_c = \frac{3\left\langle B^2 \right\rangle}{4} \int_0^{\lambda_c} \frac{\lambda d\lambda}{\left\langle \sqrt{1-\lambda B} \right\rangle}$ is the fraction of circulating particles with λ the pitch angle variable. In this section, we use f_c provided by NEO. To

recover the transport coefficients in absence of poloidal asymmetries : D_{sym}^{model}, $C_{N,sym}^{model}$ and $C_{T,sym}^{model}$ one just needs to set $P_A^{model} = 1$ and $P_B^{model} = 0$ in equations 2.56-2.58.

Next we compute the coefficients 2.54-2.56 from NEO results. The NEO inputs and outputs that are relevant in our simulations are listed in table 2.2. NEO inputs are defined at the outboard midplane, noted as $(.)_0$ in table 2.2.

Inputs	Outputs
$(\frac{R}{L_{ni}})_0$, $(\frac{R}{L_{Ti}})_0$, $(\frac{R}{L_{nZ}})_0$, $n_{W,0}/n_{i,0}$	$\Gamma_{asym,Z}^{NEO}$, $\Gamma_{sym,Z}^{NEO}$, f_c

Table 2.2 – NEO relevant inputs and outputs used for the simulations

NEO equilibrium coefficients come from the EFIT numerical equilibrium of JET-ILW pulse 85308 at 10.35s. To extract the diffusion coefficient computed by NEO called D_{asym}^{NEO}, two NEO runs are needed : they are called runs 1 and 2. They share the same inputs, except for the impurity density gradient $(\frac{R}{L_{nZ}})_0$. Sanity checks have been done to ensure that W flux evolves linearly with the impurity density gradient, therefore only two values of $(\frac{R}{L_{nZ}})_0$ are needed. The transformation $(\frac{R}{L_{nZ}})_0 = \frac{R}{L_{nZ}}\frac{\langle n_Z \rangle}{n_{Z,0}}$ is applied to match the definition of the average gradient length as defined in [7], therefore a correction factor $\frac{\langle n_Z \rangle}{n_{Z,0}}$ was added to the NEO gradient length defined at the outboard midplane, as explained in [10]. $\langle n_Z \rangle$ is the W flux surface averaged density, and $n_{Z,0}$ is the W density at the outboard midplane.Γ_1 is the output flux associated with the input $\frac{R}{L_{nZ}} = 2$, noted as $(\frac{R}{L_{nZ}})_1$. Γ_2 is associated with $\frac{R}{L_{nZ}} = 5$, noted as $(\frac{R}{L_{nZ}})_2$. D_{asym}^{NEO} is then calculated as shown in equation 2.59 :

$$D_{asym}^{NEO} = \frac{R}{\langle n_Z \rangle} \frac{\Gamma_2 - \Gamma_1}{(\frac{R}{L_{nZ}})_2 - (\frac{R}{L_{nZ}})_1} \tag{2.59}$$

We assume that the description of equation 2.54 is correct, so that $V_{N,asym}^{NEO} = -ZD_{asym}^{NEO}\frac{1}{L_{ni}}$.

To extract $V_{T,asym}^{NEO}$, an extra NEO run is needed, with a different main ion temperature gradient compared with run 1. Γ_1 is the output flux associated with the input $(\frac{R}{L_{Ti}})_1 = 1$, Γ_3 is associated with $(\frac{R}{L_{Ti}})_3 = 0$. It gives equation 2.60 :

$$V_{T,asym}^{NEO} = \frac{R}{\langle n_Z \rangle} \frac{\Gamma_1 - \Gamma_3}{(\frac{R}{L_{Ti}})_1 - (\frac{R}{L_{Ti}})_3} \frac{1}{L_{Ti}} \tag{2.60}$$

In total, to compute transport coefficients with poloidal asymmetries D_{asym}^{NEO} and $V_{T,asym}^{NEO}$, and similar coefficients without poloidal asymmetries, D_{sym}^{NEO} and $V_{T,sym}^{NEO}$, 6 NEO runs are needed.

Since the P_A^{model} geometry coefficient is equivalent to :

$$P_A^{model} = \frac{D_{asym}^{model}}{D_{sym}^{model}} \tag{2.61}$$

And assuming that equation 2.51 is an accurate description of NEO results, we define P_A^{NEO} as follows :

$$P_A^{NEO} = \frac{D_{asym}^{NEO}}{D_{sym}^{NEO}} \tag{2.62}$$

Now we have extracted P_A^{NEO} from NEO coefficients, we need to do the same with P_B^{NEO}. However, isolating P_B alone from NEO transport coefficients is not possible using NEO coefficients (equations [2.59-2.60). Therefore the term Q_B^{NEO} is defined in equation 2.63, for it is the simplest coefficient including P_B that can be extracted. Q_B^{model} is defined as :

$$Q_B^{model} = -\frac{H_0 f_C P_B^{model}}{H} = \frac{V_{T,sym}^{model} P_A^{model} - V_{T,asym}^{model}}{V_{T,sym}^{model}} \tag{2.63}$$

And assuming that equation 2.51 is an accurate description of NEO :

$$Q_B^{NEO} = \frac{V_{T,sym}^{NEO} \frac{D_{asym}^{NEO}}{D_{sym}^{NEO}} - V_{T,asym}^{NEO}}{V_{T,sym}^{NEO}} \tag{2.64}$$

Now we compare the model built from the generalization of the analytical formula (equations 2.61 and 2.63) with NEO computed terms (equations 2.62 and 2.64).

2.3.3 NEO vs analytical formula

In this section P_A^{NEO} and Q_B^{NEO} are compared with P_A^{model} and Q_B^{model} for given JET-ILW plasma profiles. Transport coefficients are then reconstructed with a combination of NCLASS runs to estimate the symmetric transport coefficients (D_{sym}^{NCLASS} equation 2.59 and $V_{T,sym}^{NCLASS}$ equation 2.60) and geometrical P_A^{model} and P_B^{model} and compared with NEO extracted transport coefficients : D_{asym}^{NEO}, $V_{N,asym}^{NEO}$ and $V_{T,asym}^{NEO}$.

2.3.3.1 JET pulse 85308 presentation and collisionality profiles

The comparison between NEO and analytical P_A^{model} and Q_B^{model} is based on JET-ILW parameters from the baseline H-mode shot 85308 ($I_P = 2.5MA$ and B=2.7T), also presented in [28]. The heating power of this discharge is 19.1 MW of NBI. Be ($n_{Be}/n_D = 2,9.10^{-2}$), and Hydrogen ($n_H/n_D = 9,5.10^{-2}$) are present in the NEO simulations. The W concentration is arbitrarily chosen so that $n_W/n_D = 10^{-5}$ and W remains a trace specie. Other dimensionless quantities at 3 radial positions are shown in table 2.3. In this section, unless specified otherwise, NEO resolution is the follows : 21 theta poloidal gridpoints, 19 extensions in pitch-angle Legendre polynomial, and 10 energy polynomials. These resolutions were checked to be sufficient at the extrema of our scans.

r/a	$R/L_{T_D} = R/L_{T_e}$	R/L_{n_e}	Z_W	Z_{eff}	q	n_W/n_D	M_D	M_W
0.1	2.4	1	44	1.39	0.9	10^{-5}	0.19	1.82
0.4	5.2	1.4	38	1.37	1	10^{-5}	0.18	1.78
0.8	10.4	2.8	26	1.29	2	10^{-5}	0.17	1.66

Table 2.3 – JET data main inputs. Pulse 85308 time averaged over 10.35s-10.85s

Figure 2.14 shows the main JET based input profiles, and figure 2.15 shows the collisionalities calculated with these inputs. Table 2.3 gives the main quantities that are used for NEO runs at three radial locations, with r/a defined as the ratio of the mid-plane averaged minor radius r, to the mid-plane minor radius r at the last closed flux surface a.

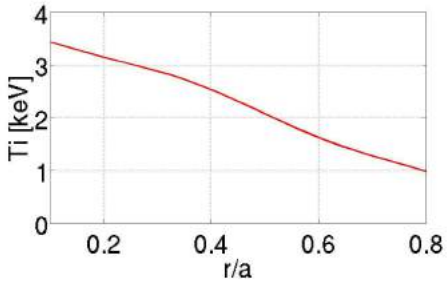

(a) Ion temperature profile

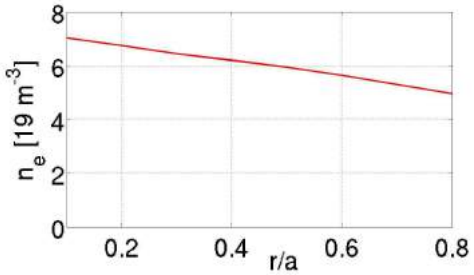

(b) electron density profile

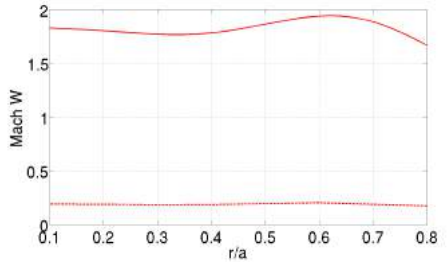

(c) Impurity and Deuterium Mach numbers : Tungsten W, solid line and D dashed line

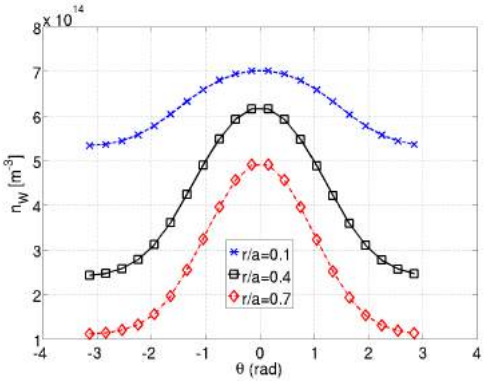

(d) W distribution vs the poloidal angle θ from NEO simulations for r/a=0.1 (blue,crosses) 0.4 (dark, squares) 0.7 (red, diamonds)

Figure 2.14 – Input profiles based on JET 85308 baseline H-mode shot ($I_P = 2.5MA$ and B=2.7T) for simulated timeslice (averaged over t=10.35s-10.85s). Experimental data and error bars can be found in [28]

The Mach number is defined as $M = \sqrt{\frac{m\omega^2 R^2}{2T}}$ where m is the mass of the considered species, R is the major radius, T the temperature and ω is the angular

frequency. Mach number from figure 2.14c) is computed based on experimental angular frequency and temperature.

Figure 2.14d shows that poloidal asymmetries are stronger at the edge. This comes from the dependency on the local value of R at a given poloidal angle R_{local} in the expression of the W density presented in [28] and re-written in equation 2.65 in the case of isotropic temperature :

$$n_Z(\theta) = n_{Z0} \exp(-\frac{eZ\phi(\theta)}{T_i} + \frac{m_Z\omega^2(R_{local}(\theta)^2 - R_0^2)}{2T_i}) \tag{2.65}$$

With n_{Z0} the impurity density at the low field side, R_{local} is the local major radius and R_0 its value at the low field side, ω is the angular frequency, θ is the poloidal angle, Z is the impurity charge, m_Z the impurity mass, and Φ a poloidally varying potential.

Collisionality parameter is still defined as $\nu^* = \frac{qR\nu}{v_{th}\epsilon^{3/2}}$. For Deuterium, the dominant collision frequency is ν_{DD} defined in equation 2.47. For, W, the dominant collision frequency is ν_{WD} defined in equation 2.1.

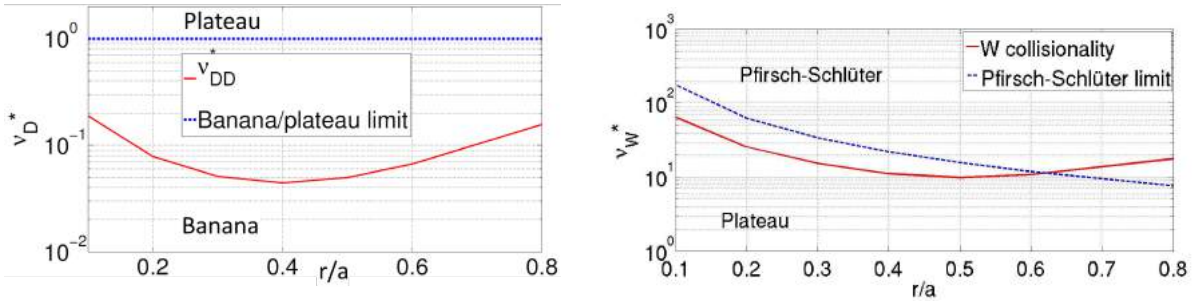

(a) D collisionality (b) W collisionality

Figure 2.15 – D and W collisionalities calculated from JET-like 85308 profiles from figure 2.14.

Figure 2.15a illustrates the D collisionality and the limit banana-plateau regime. Deuterium remains deep in the banana regime across the whole plasma. Note that in this case D collisionality differs from figure 2.7. The same definition of ν^*_{DD} is used, but in the configuration on figure 2.15, only r/a=0.1-0.8 are shown, and in this region 2.7 is indeed far from the banana/plateau limit. Moreover,apart from differences in density and temperature profiles (figure 2.6 versus figure 2.14), R and q are also varied with the radius on 2.15 while they were kept fixed on figure 2.7. This strongly impacts ϵ in ν^* calculation from equation 2.24, which explains the difference.

On figure 2.15b, the dashed line corresponds to the limit above which W reaches the Pfirsch-Schlüter regime. Again the W collisionality profile is a slightly different compared with figure 2.7 but the difference is less dramatic than on D. This is explained by the fact that the W charge is varied with the radius on figure 2.15b while being kept fixed on figure 2.7, which balances the impact of the

change of the other parameters. One can see that W is in Pfirsch-Schlüter regime only at r/a>0.6. Therefore r/a>0.6 is the only region where both species are in the regimes (W trace and Pfirsch-Schlüter, D banana) where the Angioni and Helander formula from [9] strictly applies. In the next section we compare P_A^{model} and Q_B^{model} with NEO coefficients and we study the impact of the theoretical assumptions.

2.3.3.2 Focus on terms from the formula accounting for poloidal asymmetries

P_A and Q_B terms were extracted from NEO as explained in the previous section. On figure 2.16, H corresponds to the Wenzel-Sigmar formulation from equation 2.47. For the studied JET-ILW case, H stays surprisingly close to -0,5, which is not expected if refering to figure 2.12 in section 2.2.4.4.

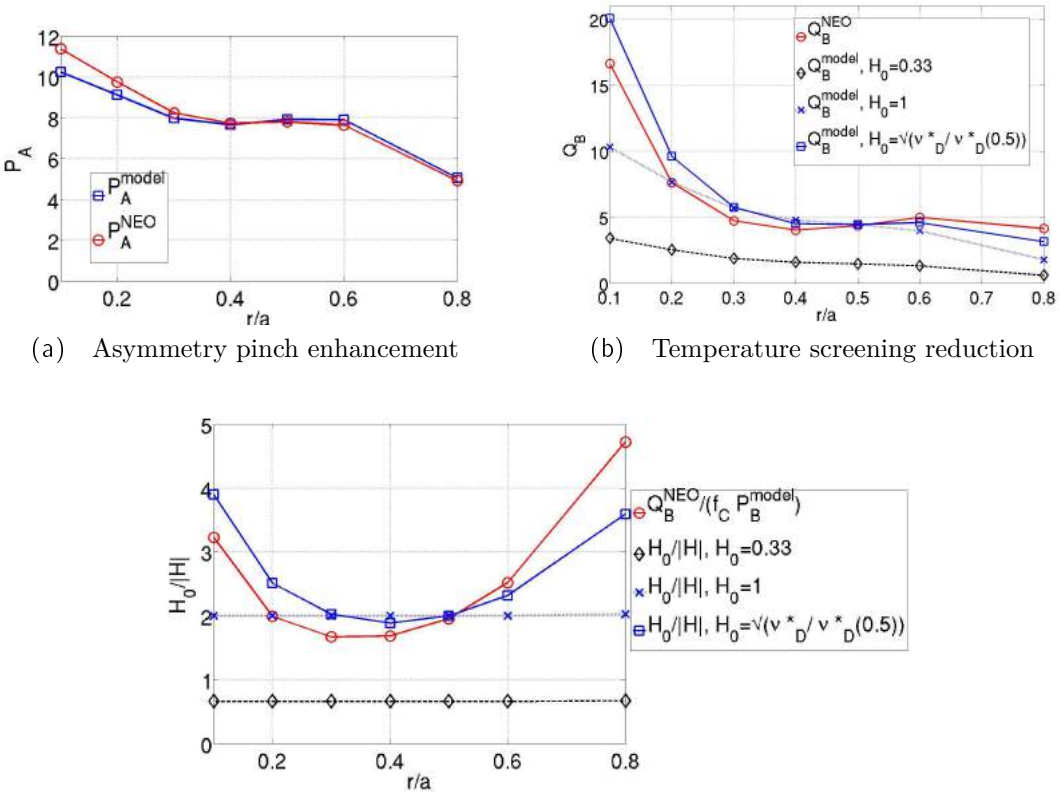

(a) Asymmetry pinch enhancement

(b) Temperature screening reduction

(c) Ratio of temperature screening coefficients

Figure 2.16 – Comparison of NEO results and model results for JET data pulse n°85308

On figure 2.16a one can see that globally P_A^{model} shows a good agreement with NEO, which is very encouraging because, as seen in figure 2.15, not all the assumptions of the analytical derivation are well fulfilled in this pulse. However,

one can note that for $r/a = 0.1 - 0.3$, P_A^{model} underestimates P_A^{NEO}. This is likely due to having W in plateau where the analytical formula does not strictly apply. Figure 2.16b shows Q_B^{NEO} compared with different Q_B^{model} combinations, each with a different H_0 formulation. Figure 2.16c shows the numerical value of $H_0/|H|$ extracted : Q_B^{NEO} is divided by $f_C P_B^{model}$, assuming that equation 2.51 is an accurate description of NEO results. $|H|$ corresponds to Wenzel-Sigmar coefficient from equation 2.47. On figure 2.16b one can see that Q_B^{model} with $H_0 = 0.33$ as initially proposed by Angioni-Helander in [9] (dashed line and diamond) is well below Q_B^{NEO} (circles and solid line). Q_B^{model} with $H_0 = 1$ (crosses and dot line) seems to be a better approximation, but at low r/a the fit can be improved. The best fit out of the three H_0 formulations presented here seems to be the empirical choice of $H_0 = \sqrt{\nu_D * / \nu_D * (0.5)}$, with $\nu *_D (0.5)$ the value of D main ion collisionality at r/a=0,5 (solid line and squares). The collisionality dependence allows to simultaneously reproduce the increase of $H_0/|H|$ in the center and towards the last closed flux surface, shown on figure 2.16c. The normalisation of main ion collisionality at r/a=0,5 was chosen because of the excellent agreement between Q_B^{NEO} and Q_B^{model} using $H_0 = 1$ at that radius. Indeed, according to [55], the 0.33 value was calculated with a simplified collision operator and remains valid only with W in Pfirsch-Schlüter regime and D in banana regime, for large temperature and density gradients. One can see that $H_0 = 1$ is a better fit to the numerical results than 0.33, but it mismatches at small r/a and r/a>0.6. The H_0 formulation depending on the collisionality gives a better match. However, a more physics based formulation for H_0 is required instead of an adjusted formulation depending on the normalization value.

To summarize, there is no radial range where both species are in the regimes (W trace and Pfirsch-Schlüter, D banana) where the Angioni and Helander formula from [9] strictly applies. However analytical P_A^{model} and Q_B^{model} show a very good agreement with NEO coefficients, provided a collisionality dependence is introduced in H_0. In order to further study the validity of the formula, and try to quantify its reliability, in the next section the impact of W Mach number is studied.

2.3.3.3 Mach number dependency scan

Mach number for main ions, M_i, for the case $T_i = T_W$, is proportional to M_W by definition, $M_i = M_W \sqrt{m_i/m_W}$. In the M_W scan we consider values up to $M_W \approx 3$, observed in JET NBI pulses [10]. In this range the bulk ion Mach number remains small, $M_i < 0.3$. Figures 2.17 illustrate such a scan where both W and the main ion (here Deuterium) Mach numbers are simultaneously varied.

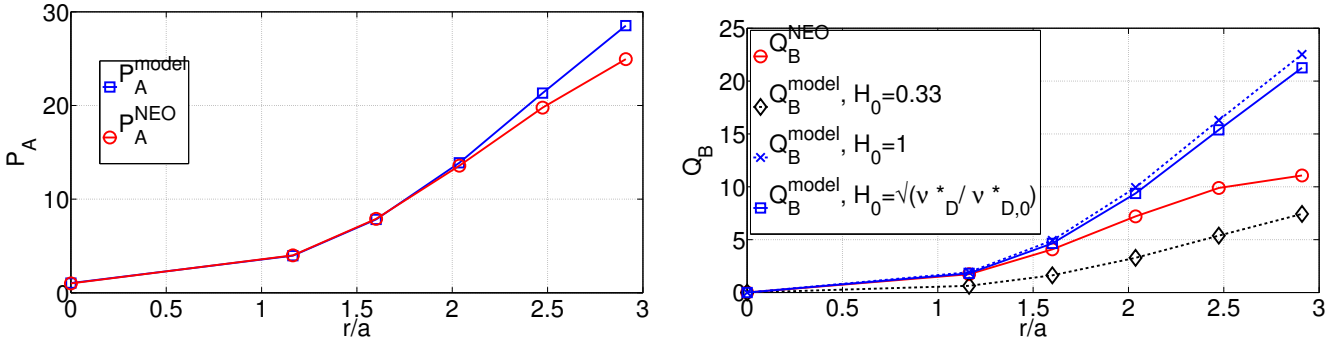

(a) Asymmetry pinch enhancement (b) Temperature screening reduction

Figure 2.17 – P_A and Q_B terms depending on W Mach number. JET data shot n°85308, r/a=0.4 in table 2.3 except $n_W/n_D = 10^{-6}$. D in banana and W in plateau. For the last two points, NEO resolution increased to 41 theta gridpoints and 39 extensions in Legendre polynomials.

One can see that the agreement is very good until $M_Z \approx 2$; above, NEO does not increase as much as geometric terms predict, both for P_A and Q_B terms with both H_0 formulations, showing a discrepancy up to 50%. In figure 2.18, another scan of the W Mach number was made, but this time W is placed in the Pfirsch-Schlüter regime. To do so, we increased both D and W densities, keeping the ratio $n_W/n_D = 10^{-5}$ fixed so that W is still a trace impurity. In the configuration shown on figure 2.18, W is in Pfirsch-Schlüter and D is still in banana regime.

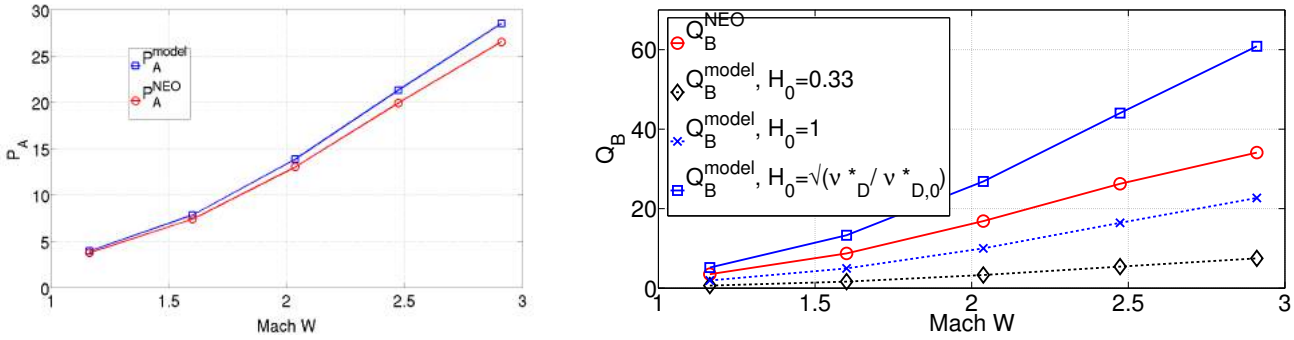

(a) Asymmetry pinch enhancement (b) Temperature screening reduction

Figure 2.18 – P_A and Q_B terms depending on W Mach number. JET data shot n°85308, r/a=0.4 in table 2.3 except $n_D = 5.10^{20}\ m^{-3}$. D in banana and W forced in Pfirsch-Schlüter regime

On figure 2.18 the fits are almost perfect for P_A until $M_Z \approx 2$, with a maximum error of 7% compared with 20% on figure 2.17a. This can be explained by the fact that, with W in Pfisch-Schlüter, NEO values are increased. On figure 2.18b for the Q_B part, one can see that forcing W into Pfirsch-Schlüter increased Q_B^{NEO} up to a factor 3. This brings Q_B^{NEO} closer to Q_B^{model} with $H_0 = 1$ formulation. Indeed

Q_B^{model} with $H_0 = 1$ values were not impacted by the change in W collisionality from figure 2.17b to figure 2.18b. However, increasing the D content as well as the W content in order to keep the ratio $n_W/n_D = 10^{-5}$ did change the value of the H_0 formulation depending on ν^*_{DD}, which shifted the Q_B^{model} accordingly. This reinforces the importance to find be better characterised H_0 formulation.

Overall, for very strong poloidal asymmetries, W needs to be in Pfirsch-Schlüter regime for the formula to be applicable. In this configuration the H_0 formulation plays a crucial role in the estimation of Q_B^{model}. Therefore, until a better H_0 formulation is established, the use of NEO is recommended. But for this JET-ILW case, as shown on figure 2.14c W Mach number is low enough so that analytical coefficients can be used.

2.3.3.4 Reconstruction of the transport coefficients

To complete the test of the validity of the model, one can compare NEO coefficients from equations 2.59-2.60 with a combination of NCLASS runs and geometrical P_A^{model} and P_B^{model} from equations 2.49 and 2.50. NCLASS inside JETTO provides a factor 1100 speedup compared with NEO because it is a fluid-moment based model, solving a lower dimensionality problem, while NEO solves exactly the drift kinetic equation. Moreover, NCLASS uses a simple collision operator, which saves time compared to NEO especially with multi-species cases, like the JET-ILW pulse used here.

For clarity, the three transport coefficients are presented as they would be used in a transport code : the diffusion term, defined in equation 2.56; the main ion gradient pinch velocity term, defined in equation 2.54; and the temperature screening term, defined in equation 2.55. But instead of using the analytical expressions for the poloidally symmetric coefficients in equations 2.54-2.56, we use NCLASS poloidally symmetric transport coefficients D_{sym}^{NCLASS}, $V_{N,sym}^{NCLASS}$ and $V_{T,sym}^{NCLASS}$, obtained by using the same procedure shown in equations 2.59-2.60. Therefore we define, in equations 2.66-2.68, coefficients that combine NCLASS poloidally symmetric coefficients and analytical P_A and P_B : $D_{asym}^{NCLASS,model}$, $V_{N,asym}^{NCLASS,model}$ and $V_{T,asym}^{NCLASS,model}$.

$$D_{asym}^{NCLASS,model} = D_{sym}^{NCLASS} P_A^{model} \tag{2.66}$$

$$V_{N,asym}^{NCLASS,model} = Z D_{sym}^{NCLASS} P_A^{model} \frac{R}{L_{ni}} \tag{2.67}$$

$$V_{T,asym}^{NCLASS,model} = V_{T,sym}^{NCLASS} \left[P_A^{model} + \frac{H_0 f_C P_B^{model}}{H} \right] \tag{2.68}$$

For the comparison between NCLASS and NEO we also introduce transport coefficients which are a combination of NEO poloidally symmetric coefficients associated with P_A^{model} and P_B^{model}, defined as follows :

$$D_{asym}^{NEO,model} = D_{sym}^{NEO} P_A^{model} \tag{2.69}$$

$$V_{N,asym}^{NEO,model} = Z D_{sym}^{NEO} P_A^{model} \frac{R}{L_{ni}} \tag{2.70}$$

$$V_{T,asym}^{NEO,model} = V_{T,sym}^{NEO} \left[P_A^{model} + \frac{H_0 f_C P_B^{model}}{H} \right] \tag{2.71}$$

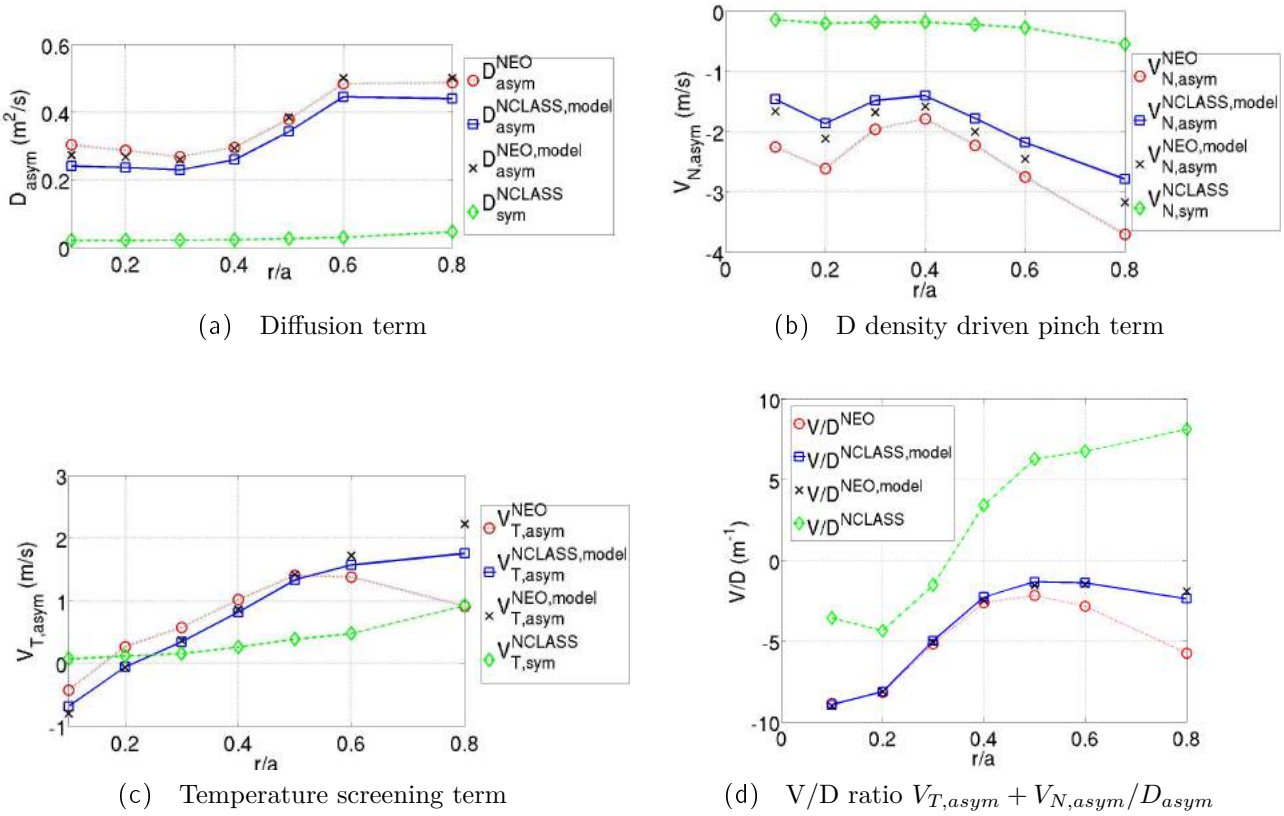

(a) Diffusion term

(b) D density driven pinch term

(c) Temperature screening term

(d) V/D ratio $V_{T,asym} + V_{N,asym}/D_{asym}$

Figure 2.19 – Reconstruction of W transport coefficients : comparison between NEO and NCLASS+correction factors for the parameters from table 2.3 and figure 2.14

First of all, one can notice on figures 2.19 that NCLASS alone (dash-dot line and diamonds) underestimates all transport coefficients by an order of magnitude for $M_W \approx 2$. On the contrary NCLASS combined with P_A^{model} and P_B^{model} (squares and solid line) is very close to NEO (circles and dot line) coefficients while obtained 1100 times faster. Indeed NEO runs take the same time, with or without asymmetry. NEO and P_A^{model} and P_B^{model} combined with NEO (crosses) symmetric runs give also globaly similar results.

Regarding the diffusion term (figure 2.19a)), $D_{asym}^{NCLASS,model}$ (squares and full line) is lower than both NEO-only diffusion coefficient D_{asym}^{NEO} (circles and dotted

line), and $D_{asym}^{NEO,model}$ (crosses). The difference in collision operator between NEO and NCLASS explains the gap between $D_{asym}^{NCLASS,model}$ and $D_{asym}^{NEO,model}$. Finally the difference between $D_{asym}^{NEO,model}$ and D_{asym}^{NEO} comes from the difference between P_A^{model} and P_A^{NEO} on figure 2.16. We mostly want to see how $D_{asym}^{NCLASS,model}$ compares with D_{asym}^{NEO} and although we recover the difference between P_A^{model} and P_A^{NEO} on figure 2.16, both coefficients remain comparable.

The fit on the D density driven pinch term on figure 2.19b shows a similar trend : $V_{N,asym}^{NCLASS,model}$ is lower than $V_{N,asym}^{NEO}$. One can notice that this term is one order of magnitude bigger than the diffusion term in figure 2.19a, due to the W charge factor.

Concerning the temperature screening term on figure 2.19c we use $H_0 = \sqrt{\nu_D*/\nu_{*D}(0.5)}$ as it seems to be the best adjustment for this case. On figure 2.19c, there is a sign change at low epsilon, coming from H_0 and H compensating each other. The agreement between $V_{T,asym}^{NCLASS,model}$ and $V_{T,asym}^{NEO}$ combined with analytical P_A^{model} and Q_B^{model} is very good except for the last point at r/a=0.8 where a factor 2 discrepancy is observed. However one can notice that the temperature asymmetry screening term is two times weaker than the D density driven pinch contribution to the W flux.

Figure 2.19d shows the ratio V/D, ie the ratio of the convection term (combining V_T and V_N) to the diffusion term D. One can see that V/D^{NCLASS} (green dash-dot lines and diamond) overestimates the peaking by one order of magnitude. The agreement between V/D^{NEO} (red circles), $V/D^{NEO,model}$ (black crosses) and with $V/D^{NCLASS,model}$ (blue squares) is excellent from the center until r/a=0.4. For r/a>0.4 $V/D^{NEO,model}$ and $V/D^{NCLASS,model}$ over-estimates the peaking by a maximum of 50% at r/a=0.8. This difference comes mainly from the overestimation of the temperature screening term (see figure 2.19c).

The last step is to test the combination NCLASS + geometric P_A^{model} and Q_B^{model} inside a JET transport solver, JETTO. The goal is to compare the resulting W 2D profile time evolution with P_A^{model} and Q_B^{model} and full NEO with poloidal asymmetries.

2.3.4 Application in the integrating modeling tool JETTO

2.3.4.1 85308 : simulation of one set of profiles at a given time

P_A^{model} and Q_B^{model} equations are implemented in the JET integrated modeling platform JETTO [115]. JETTO is coupled with NCLASS and NEO, but also with the impurity module SANCO [4], that calculates impurity profiles and the amount of radiation produced. JETTO will be introduced in greater details in the next chapter. The goal of this exercise is to study the impact of the discrepancies between D_{asym}^{NEO}, V_{asym}^{NEO} and $D_{asym}^{NCLASS,model}$, $V_{asym}^{NCLASS,model}$ seen of figure 2.19.

To calculate analytically P_A^{model} and Q_B^{model}, the fraction of passing particles is an output from JETTO magnetic equilibrium. The W distribution is calculated inside JETTO using equation 2.65 above. Therefore, all the pieces necessary to estimate P_A^{model} and Q_B^{model} are computed independently from NEO. The simula-

tions starting at t=10.35s are performed over 0,5s to make sure NEO/NCLASS and SANCO are converged. JETTO is ran with all transport channels interpretive. The input profiles used in JETTO are based on the JET pulse 85308 illustrated on figure 2.14. Only W neoclassical transport is evolved as W turbulent transport is assumed to be negligible.The total W content remains fixed during the time evolution of the simulation. JETTO-NCLASS simulations with P_A^{model} and Q_B^{model} ran on average 1100 times faster than JETTO-NEO simulations, as found when comparing stand alone NEO vs NCLASS combined with P_A^{model} and Q_B^{model} in section 2.3.3.

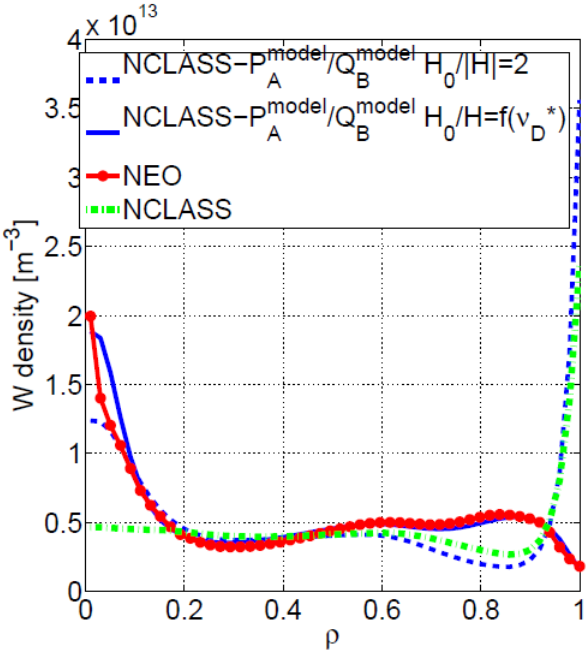

Figure 2.20 – Flux surface averaged W density profile $< n_W >$ depending on ρ : comparison between JETTO-NEO and JETTO-NCLASS $+P_A^{model}/P_B^{model}$ based on JET case 85308 at t=10.85s

We compare, on figure 2.20, the W profile calculated with JETTO-NEO, and the W profile calculated using JETTO-NCLASS with P_A^{model} and Q_B^{model}. For the whole r/a range, JETTO-NEO (full line and circles) and JETTO-NCLASS$+P_A^{model}/Q_B^{model}$ with H_0 depending on ν_D*(full line) are very close. The agreement of JETTO-NEO with and JETTO-NCLASS$+P_A^{model}/Q_B^{model}$ with $H_0/|H| = 2$ (dashed line) is also very good within $\rho = 0.5$, except in the very core where JETTO-NCLASS$+P_A^{model}/Q_B^{model}$ with $H_0/|H| = 2$ underestimates the peaking. JETTO-NCLASS (dashed and dotted line) does not account for poloidal asymmetries and therefore does not capture the W core density peaking. For ρ larger than 0.5 up to the pedestal region, the curves split in two groups : JETTO-NCLASS$+P_A^{model}/Q_B^{model}$ with H_0 depending on ν_D* stays in very good agreement with JETTO-NEO. However in this region JETTO-NCLASS alone and JETTO-NCLASS$+P_A^{model}/Q_B^{model}$ with $H_0/|H| = 2$ both underestimate JETTO-NEO results. In the pedestal region, the

study made in section 2.3.2 does not apply. JETTO-NCLASS alone and JETTO-NCLASS+P_A^{model}/Q_B^{model} with $H_0/|H| = 1$ both present an increased peaking at the boundary due to the boundary condition and the total W content forced to be constant. JETTO-NCLASS+P_A^{model}/Q_B^{model} with H_0 depending on ν_D* keeps its very good agreement with JETTO-NEO. Therefore a H_0 increase with ν_D* increasing seems to be a key ingredient to predict the W profile, as observed previously in the stand-alone study on figure 2.19. The underlying physics still requires to be investigated.

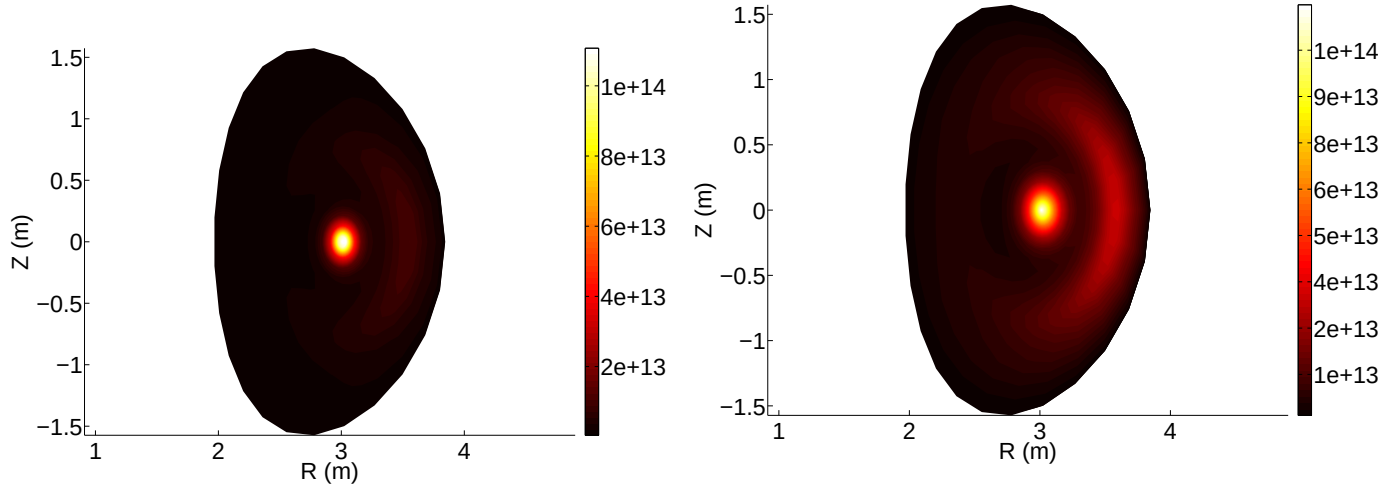

(a) JETTO-NCLASS with P_A^{model}/Q_B^{model} and with H_0 depending on ν_D*

(b) JETTO-NEO

Figure 2.21 – 2D maps of the W distribution in particles/m^{-3} at t=10.85s

Figures 2.21 show the 2D maps of the W distribution at t=10.85s, with P_A^{model}/Q_B^{model} and with H_0 depending on ν_D* (left) and JETTO-NEO (right). As seen on figure 2.20, both simulations show similar results, with a central accumulation. The modeling of the poloidal asymmetries in the outer part is a factor 3 more signalized in the JETTO-NEO simulation than in the JETTO-NCLASS P_A^{model}/Q_B^{model} simulation.

2.3.4.2 82722 : time evolving simulation with time evolving profiles

To further test the robustness of P_A^{model} and Q_B^{model} inside JETTO over time, another JET ILW H-mode pulse was chosen. The hybrid pulse 82722 ($B_T = 2$ $TI_P = 1.7MA$) shows W accumulation due to a dominant neoclassical transport in the core [10] (see figure 2.23a), therefore it is important to see if the formula reproduces successfully this pattern. This pulse will be analyzed in details in the

next chapter. Here, the simulation runs for 1.6s, from 5.5s to 7.1s, which corresponds to the shaded part on figure 2.22. In this time window only Neutral Beam Injection is at play. We also have several sawteeth (seen on the central temperature figure 2.22) and Edge Localized Modes. The main plasma profiles evolution (electron density and temperature, ion temperature and plasma rotation) is not evolved, instead we use fits based on experimental data. Those profiles are updated every 0.1s. Only W neoclassical transport is modeled using NEO or the P_A^{model}/Q_B^{model} formula combined with NCLASS. The total W content is forced to remain constant during the whole simulation. At the beginning of the simulation $n_W/n_D = 5.10^{-5}$, is chosen to match experimental radiation level, assumed to be caused by W only. Be is added to match the experimental $Z_{eff} = 1.34$. For this JETTO simulation we only used the H_0 depending on ν_D* formulation. The goal of the simulation is to compare the ability of NCLASS combined with P_A^{model}/Q_B^{model} to reproduce NEO results over time.

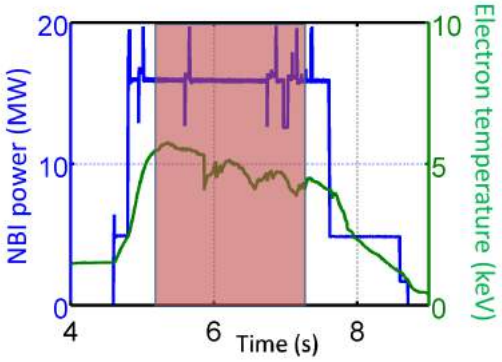

Figure 2.22 – Experimental timetraces of NBI, T_e(ECE) of 82722 pulse

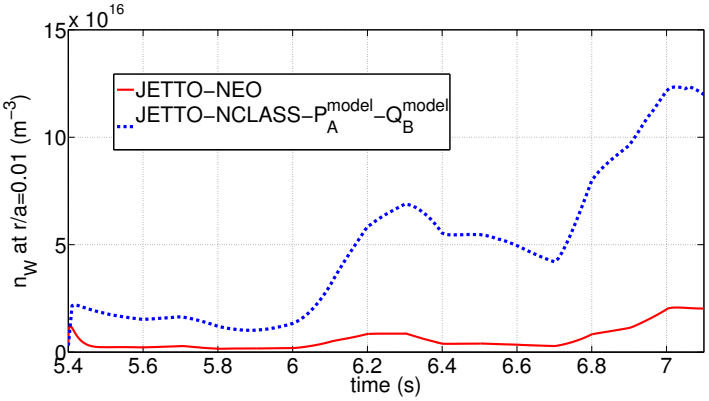

(a) W density over time at $\theta = 0$ at r/a=0.01

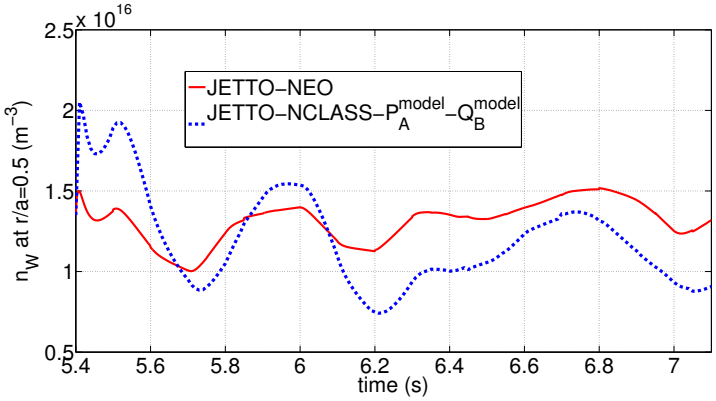

(b) W density over time at $\theta = 0$ at r/a=0.5

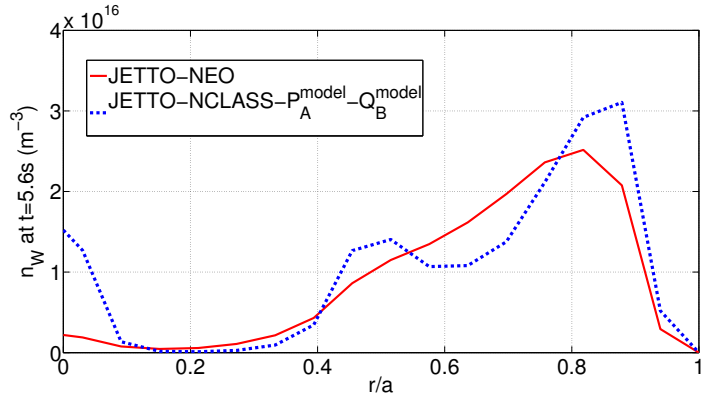

(c) W density profile at $\theta = 0$ at t=5.6s after 0.2s of simulation

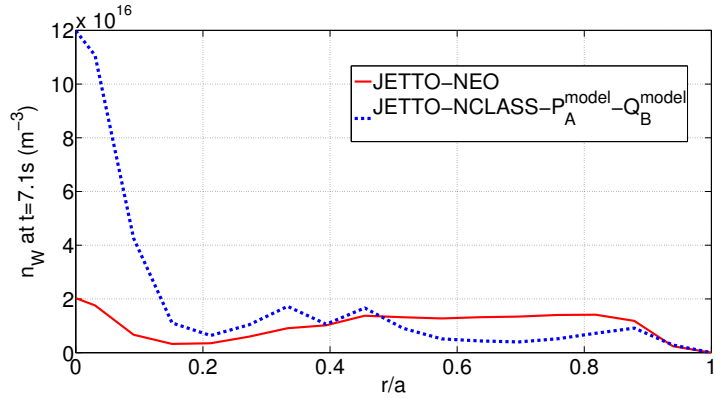

(d) W density profile at $\theta = 0$ at t=7.1s after 1.6s of simulation

Figure 2.23 – W density at the Low Field Side over time at r/a=0.01 and r/a=0.5 and W density profile at the Low Field Side at t=7.1s after 1.6s of simulation. JETTO-NEO (red full line) and JETTO-NCLASS-$P_A^{model} - Q_B^{model}$ (blue dashed line)

In order to quantify more precisely the quality of the simulations, the W density timetraces of JETTO simulations are shown at r/a=0.01 (on figure 2.23a) and r/a=0.5 (on figure 2.23b). One can see that at r/a=0.01 on figure 2.23a, very close to the plasma center, JETTO-NCLASS combined with P_A^{model}/Q_B^{model} simulation (blue dashed line) overestimates NEO prediction (red full solid line) by a factor 6, similarly to the previous case on figure 2.20. At mid-radius on figure 2.23b, JETTO-NEO and JETTO-NCLASS combined with P_A^{model}/Q_B^{model} simulations reach a much better agreement, with a maximum of 30% difference. Figure 2.23c shows the W density profile at t=5.6s after 0.2s of simulation. At this time on both simulations, W is mostly located on the outer half of the plasma. However in the center JETTO-NCLASS combined with P_A^{model}/Q_B^{model} already starts to overestimate JETTO-NEO results by a factor 5. Figure 2.23d shows the W density profile at t=7.1s after 1.6s of simulation. Both NEO and NCLASS combined with P_A^{model}/Q_B^{model} simulations predict that most of the W moved towards the center. Between r/a=0.5-0.9, JETTO-NCLASS combined with P_A^{model}/Q_B^{model} underesti-

mates JETTO-NEO results up to a factor 3. And most importantly, in the central part, JETTO-NCLASS combined with P_A^{model}/Q_B^{model} overestimates JETTO-NEO by a factor 6.

2D W density maps at t=6.8s, therefore after 1.3s of simulation, are shown on figure 2.24. Figure 2.24a shows the prediction of JETTO-NCLASS and P_A^{model}/Q_B^{model}, figure 2.24b shows the prediction of JETTO-NEO. The poloidal asymmetries are clearly visible on figure 2.24b, the W did not move towards the center yet. The W density absolute values are comparable between the two simulations. Some W already moved in the center (as seen on figure 2.23c). The JETTO-NCLASS combined with P_A^{model}/Q_B^{model} predicts that all the W already moved toward the center, overestimating the JETTO-NEO W content by a factor 5, even though the poloidal asymmetry is still present (red shape on figure 2.24a).

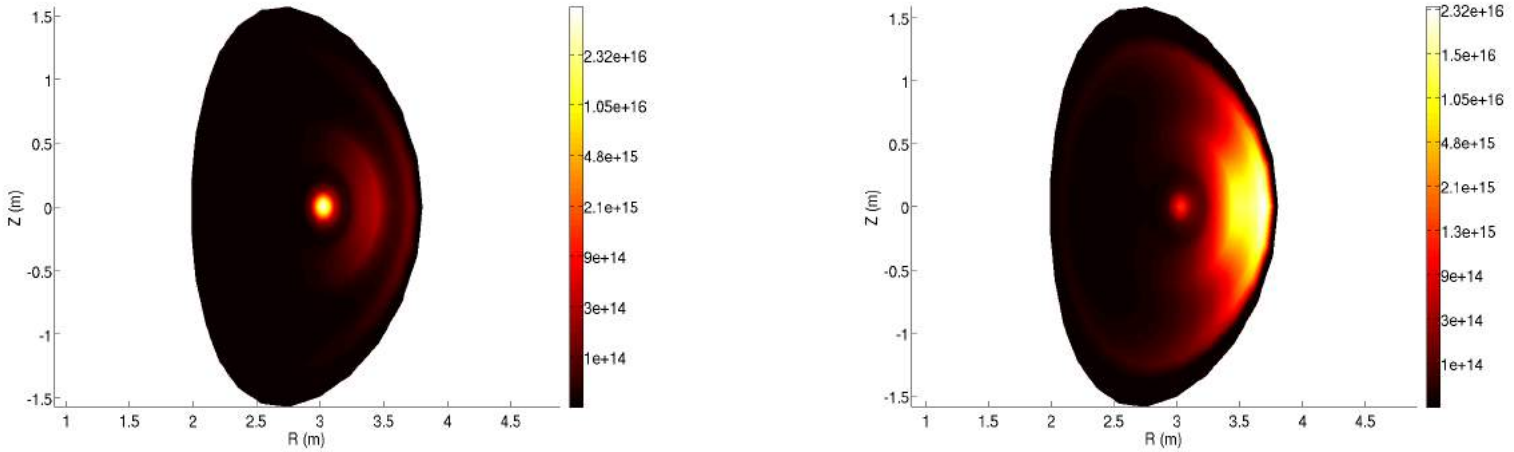

(a) Pa/Pb model + NCLASS (b) NEO

Figure 2.24 – Comparison of 2D plots of W density at t=6.8s (after 1.3s of simulation) for 82722

Overall, for the 82722 shot, the JETTO-NEO and JETTO-NCLASS with P_A^{model}/Q_B^{model} simulations seems to agree quite well at mid-radius and disagree in the center. This can be surprising since on figure 2.21 the agreement in the center was much better. In order to study this pattern, figures 2.25 show the ratio of the neoclassical convection over the neoclassical diffusion depending on r/a at t=6.8s for JETTO-NEO and JETTO-NCLASS with P_A^{model}/Q_B^{model}. Figure 2.25b focuses on the central part. On 2.19d,for the pulse 85308, the agreement of the transport coefficients between JETTO-NEO and JETTO-NCLASS with P_A^{model}/Q_B^{model} was excellent in the center, leading to a good agreement on the W density profile on figure 2.21. For 82722, in the central part on figure 2.25b, JETTO-NCLASS with P_A^{model}/Q_B^{model} overestimates JETTO-NEO results up to a factor 2. Then from r/a=0.2-0.85 on figure 2.25a, both ratios altern positive and negative values, -20 to 10 and a maximum of 50% disagreement, which is consistent with figure 2.23b. However they intersect several times and do not change sign at the same

radii. Finally from r/a=0.85 outward, JETTO-NEO models a very strong peaking inward, while JETTO-NCLASS with P_A^{model}/Q_B^{model} simulation starts dropping and then increases again to finish around V/D=-250, a factor 4 too small compared with JETTO-NEO. Note that NEO starts decreasing at r/a=0.85 before JETTO-NCLASS, which drops at r/a=0.9.

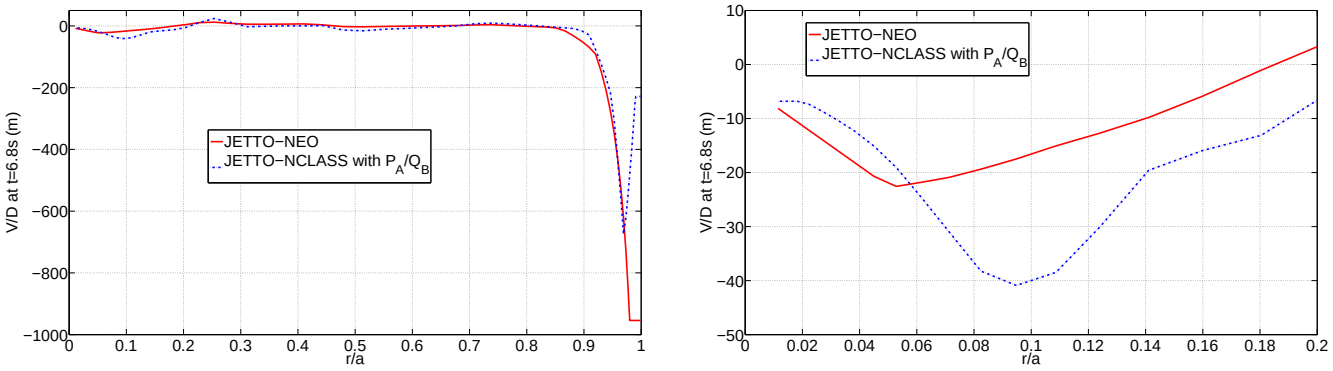

(a) Neoclassic V/D over rho at t=6.8s

(b) Zoom on the central part

Figure 2.25 – Neoclassic V/D over rho at t=6.8s. JETTO-NEO (red full line) and JETTO-NCLASS (blue dash dot)

To summarize, NCLASS associated with the equations P_A^{model} and Q_B^{model} allows to reproduce poorly the W density predicted by NEO in JETTO, while being 1100 times faster. It especially overestimates the core accumulation up to a factor 6. The choice of the collisionality dependency of H_0 formulation was proved to be crucial to reproduce of NEO results. On a time evolving simulation, NCLASS and P_A^{model}/Q_B^{model} predictions captures correctly the poloidal asymmetries but overestimates the core accumulation. Nonetheless, in case of poloidal asymmetries, NCLASS associated with the equations P_A^{model} and Q_B^{model} can be used within JETTO to speed up scoping studies, while NEO is required for accurate predictions.

2.4 Conclusion of the chapter

For high-Z impurities such as Tungsten (W), neoclassical transport must be accounted for in integrated modeling simulations. Neoclassical transport deals with transport due to particle collisions. Collisions mainly depend on the densities of the species, their temperatures, their charges and their masses. Depending on their energies, particles might end up trapped on magnetic field lines. In absence of poloidal asymmetries, trapping and circulating particles are separated in three collisional regimes, banana, plateau and Pfirsch-Schlüter. For each category, simplified formulae are used to describe the diffusion process and the corresponding poloidal velocity and particle flux. But this simplified approach is

not adequate for Tungsten because,due to its large mass and charge, W neoclassical transport can be significantly enhanced by poloidal asymmetries [9].

Poloidal asymmetries are produced by the centrifugal force in presence of NBI [72, 140, 114, 55, 10] and/or by RF heating [35, 82, 19]. In some JET cases, the enhancement can reach an order of magnitude (first established in [114] and continued in [28, 10, 7]). It is therefore essential to take poloidal asymmetries into account in integrated modeling. The effect of poloidal asymmetries are captured by the neoclassical code NEO [10]. At first, neoclassical poloidally symmetric standard quantities calculated by NEO are compared with text book analytical derivation (diffusion coefficient, poloidal velocities, impurity flux, diffusion and convection coefficients) in various collisional regimes (banana, plateau, Pfirsch-Schlüter). NEO is also compared to GYSELA for poloidally symmetric cases. In numerous regimes NEO is shown to disagree with analytical formulations. But it agrees with NCLASS for D in banana/plateau regimes and W in plateau/Pfirsch-Schlüter, which are the most likely configurations in experimental plasmas.

However, NEO leads to significant computational expense in integrated modelling applications. In presence of poloidal asymmetries, the goal was to determine if it was feasible to combine geometric analytical terms from [9] describing the effect of poloidal asymmetries on W flux, with a simpler and faster neoclassical code, NCLASS [74], in order to produce results similar to the ones obtained with NEO.

At first, the analytical formula by Angioni-Helander [9] was tested outside of its range of applicability. Indeed, W can be in the plateau regime and not only in Pfirsch-Schlüter regime for realistic tokamak plasma parameters. Furthermore, the analytical formula has been empirically adjusted to match better NEO by accounting for a collisionality dependence in the reduction factor of the temperature screening due to poloidal asymetries. As long as the D is in the banana regime, the analytic formula can be applied even with W out of the Pfisch-Schlüter regime. For very strong poloidal asymmetries with main ions in the banana regime, the geometric convection enhancement factor Q_B overestimates NEO results (up to 50%), impacting also temperature screening term.

In order to test further NCLASS+P_A^{model}/Q_B^{model} and NEO, they were implemented in JETTO. All the profiles are fits from experimental data, only the W profile is evolved, assuming a purely neoclassical transport. In one case based on JET baseline scenario parameters, this fast model can predict a very similar 2D W density map as NEO while saving a factor 1000 in computer time. In a second JET hybrid scenario case, the central tungsten peaking was overestimated due to a sensitive balance between temperature screening and inward impurity convection near the magnetic axis. The model in its present formulation therefore cannot be considered to have general applicability, but could be used for scoping studies before running the full NEO model. The parametric dependencies of the temperature screening reduction due to poloidal asymmetrics still remains to be better characterised and explained by neoclassical theory; such an understan-

ding would allow our fast neoclassical model for heavy impurity transport to be extended to more general applicability. In order to gain CPU time while keeping the accuracy of NEO, another possibility would be to develop a Neural Network regression for NEO, similarly to the work done for QuaLiKiz [37, 107].

In the next chapter, the focus is set on integrated modeling for W transport. All background profiles are simultaneously evolved and both neoclassical and turbulent transport are accounted for. From now on, NEO only will be used in JETTO.

3First principle integrated modeling of multi-channel transport including Tungsten in JET

3.1 Introduction of the chapter

W transport is both turbulent and neoclassical. As seen in the previous chapter, neoclassical transport depends on main ion temperature and density gradients, as well as on plasma rotation. Therefore, in order to understand the mechanisms of W transport, it is crucial to predict accurately and self-consistently the time evolution of the temperature, density and rotation profiles. To do so, one needs to model the interplay between heat, particle, angular momentum, sources and losses, transport (both neoclassical and turbulent), over multiple confinement times while self-consistently letting the current diffuse and reconstruct the magnetic equilibrium. Therefore the use of an integrated modeling tool such as JETTO [115] is mandatory. The goal of our simulations is to reproduce the experimental behavior of a representative hybrid JET-ILW shot (n°82722) over 10 confinement times. While it has been demonstrated that MHD phenomena impact the W behavior in the core through sawteeth [89] and at the edge through Edge Localized Modes [52], they are not modeled in our simulations. This decision is based on the results of [10], which shows JETTO simulations conducted with GKW [105] and NEO [15, 17] at given time slices that successfully reproduce SXR measurements. Therefore the focus of our work is the time evolution of W behavior through the modeling of neoclassical and turbulent transport using the most advanced theoretical models available for integrated modeling, QuaLiKiz [22, 20, 37] and NEO. To model the W source, the initial W content was adjusted to match the bolometry signal, plus a constant incoming flux at the Last Closed Flux Surface (LCFS). The modeled pedestal remains fixed during the simulation with an artificially adjusted transport matching measurements, without ELM modeling.

In section 3.2 the JET-ILW shot and its characteristics are presented, especially the W accumulation process. In section 3.3 all the JETTO modules available are presented, along with the configuration used in this work. Section 3.4 presents the results of the simulations compared with measurements for the plasma profiles and W. Section 3.5 focuses on two actuators leading to W accumulation : central particle source and toroidal rotation. Section 3.6 deals with the W stabilization effect in the simulations and its causes. Finally, conclusions are drawn in section 3.7

3.2 Presentation of JET-ILW shot : plasma profiles and W accumulation phenomenon

As seen in the first chapter, understanding and modeling the mechanisms leading to central W accumulation is a priority. In this perspective, [10] presents a detailed analysis of the hybrid JET-ILW shot #82722. For two time slices, JETTO [115]-SANCO [4] interpretive simulations are run, with density, temperature and rotation profiles made of fits from experimental data. GKW [105] predicts turbulent transport and NEO [15, 17] models neoclassical transport. The simulations successfully reproduce SXR measurements of the W density, showing that turbulent and neoclassical transport modeling at a given time provide an accurate description of the W behavior. In order to pursue the work of [10] and deepen the understanding of the W transport mechanisms, the present work proposes a self-consistent simulation of the pulse, with time-evolving profiles (density, temperature, rotation) as well as the W transport (both turbulent and neoclassical), over 10 confinement times. The goal is to quantify how accurately the time evolution of the W behavior is reproduced with the plasma profiles evolving self-consistently and the modeling of turbulent and neoclassical transport.

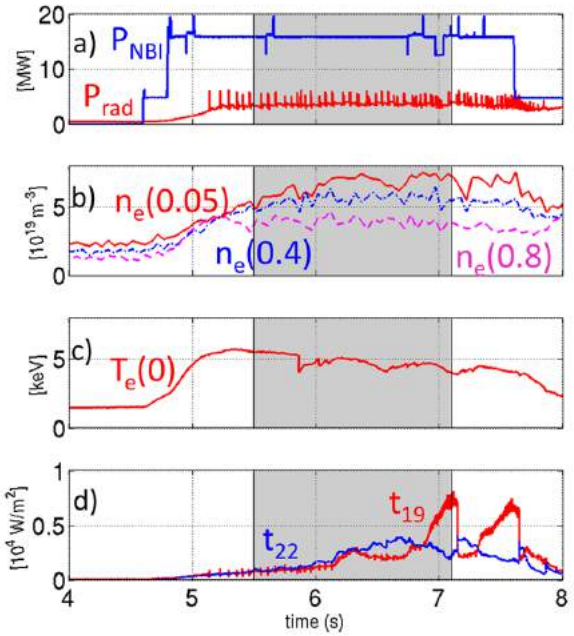

Figure 3.1 – Experimental timetraces of NBI and radiated power from bolometry (a), electron density at different position from HRTS (b), central electron temperature from ECE (c), and central (t19) and ρ ==0.22 (t22) SXR lines of 82722 JET pulse

Timetraces of the chosen JET-ILW pulse (#82722 B_T=2T I_P=1.7MA) are shown on figure 3.1. The modeled time window corresponds to the shaded area,

from 5.5s to 7.1s. In this time window only Neutral Beam Injection (NBI) is at play for 16 MW. The presence of ELMs in the pedestal is visible on the total radiated power on 3.1a. The total radiated power remains stable during the whole discharge, showing no sign of W central accumulation. However the SXR central line t_{19} on figure 3.1d shows strong peakings when compared with the peripheric SXR line t_{22}, which denounces the W central accumulation, visible also on figure 3.3. Around 5s, the electron density shown on 3.1b has a hollow profile, which is more visible on figure 3.2a. Then the central density peaks, though limited by three sawtooth crashes at 5.9s, 6.5s and 7.1s, with an inversion radius at $\rho \approx 0.2$. The sawteeth can also be seen on the central temperature on 3.1c and on the central SXR line on 3.1d. The central electron temperature on 3.1c first increases until 5.5s, then tends to decrease with time. Note that there is no SXR peak corresponding to the time between the sawteeth at 5.9s and 6.5s. It comes from the fact that W has not yet moved towards the axis, as seen later of figure 3.3a.

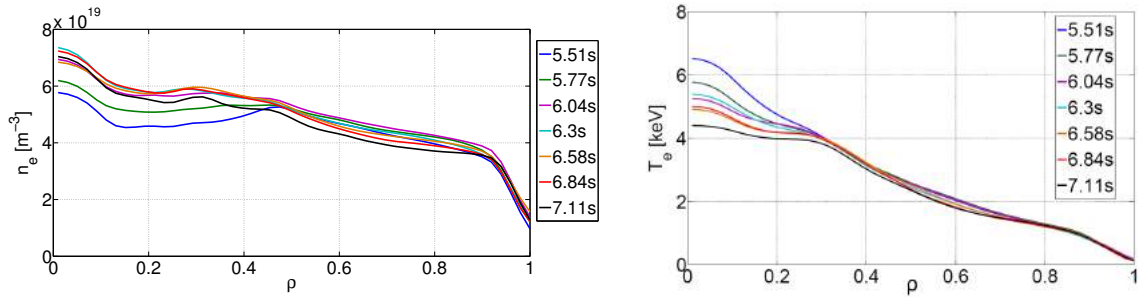

(a) n_e. (b) T_e.

Figure 3.2 – Selection of electron density and temperature profiles obtained by cubic spline fits of the JET HRTS diagnostic plotted against ρ, with ρ the square root of the toroidal flux

Selection of electron density and temperature profiles obtained by cubic spline fits of the JET High Resolution Thomson Scattering (HRTS) diagnostic are presented on figure 3.2a and 3.2b. Through the whole time window, the pedestal height of the electron density varies around 20%, which is due to the presence of ELMs, visible on the radiation on figure 3.1. At the beginning of our time window, the electron density profile is hollow at 5.5s, which means that the density at ρ=0.2 is lower than the density around mid-radius. The central density is already peaked, meaning that the radial gradient is negative. This phenomenon is most likely caused by NBI central particle source (see figure 3.24a) and low central diffusivity [90]. Then the density builds up over time from mid-radius inward, keeping a strong central peaking. One sawtooth crash occurs between 6.3s and 6.5s, causing the central density to drop. Between 6.8s and 7.1s the central density increases and then slightly drops again. As explained later on section 3.4, the electron density gradient, especially the central one, plays a major role in W transport and accumulation.

On figure 3.2b, the electron temperature profiles remain quite unchanged from ρ=0.3 outward. The central temperature tends to decrease over time, from ρ=0.3 inward. The impact of the three sawtooth crashes (5.9s, 6.5s and 7.1s) is visible : the central temperature increases between 6s and 6.3s, and again between 6.6s and 6.8s. Overall the central electron temperature drops by 35% in 1.6s.

To confirm the presence of W in the core, the poloidal cross sections of the experimental W density are shown on figure 3.3, at t=6.2s before the central SXR line on figure 3.1 peaks, and at t=7s during a SXR central line peak.

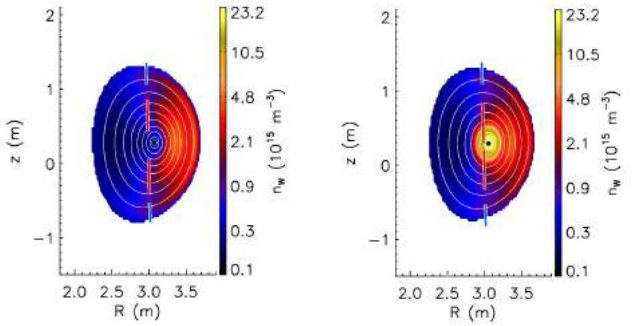

(a) W density at t=6.2s. (b) W density at t=7s.

Figure 3.3 – Poloidal cross sections of the W density estimated from SXR-UV measurements

The W density is reconstructed from SXR measurements based on the method from [120]. This method is valid for electron temperature above 1.5 keV, which is the case most of the time in the modeling time window. Moreover, the transport time-scale must be negligible compared with W recombination and ionization rates. Assuming that W is the main contribution to radiation, the SXR emissivity ϵ^{SXR} and W density n_W are linked by equation 3.2 :

$$\epsilon^{SXR} = n_W n_e L_W^{SXR} \tag{3.1}$$

n_e is the electron density and $L_W^{SXR} = \sum_q f_{W,q}(K_{W,q}^{ff} + K_{W,q}^{fb} + K_{W,q}^{bb})$ is the cooling factor, defined in [133] and illustrated on figure 8 in chapter 1 section 5.1. $f_{W,q}$ the fractional abundance of the ionization state W_q, K^{ff} is the emissivity coefficient of the Bremsstrahlung (free-free) contribution, K^{fb} is the emissivity coefficient of the radiative recombination(free-bound) contribution and K^{ff} is the emissivity coefficient of the ray emission (bound-bound) contribution. The cooling factor depends on the electron temperature and its estimation for W is made in [108]. A first SXR emissivity estimation, constant over the flux surface, is obtained by performing an Abel inversion on the HFS lines of sight. Then, assuming a poloidal asymmetric emissivity distribution that can be written as in [140], a χ^2-minimization procedure is performed to match at best all the lines

of sight. This operation gives a 2D emissivity map. Once the maps on electron density and cooling factors are obtained, a first estimation of the W density map is made. Then a cross-calibration between the 2D W density map and the spectrometer measurements is performed. Finally, the W density map is adjusted to match the experimental Z_{eff} value, assuming that Be is the only other impurity.

In our analysis of figure 3.3 we shall assume that the radiations are caused by W only. On figure 3.3a at t=6.2s, the W did not reach the center yet and gathers at the Low Field Side, showing strong poloidal asymmetries. At this time the W concentration is around $n_W/n_D = 7.10^{-5}$ so the W is still a trace specie, ie $\frac{Z_W^2 n_W}{Z_i^2 n_i} << 1$ with i main ion. At 7s shown on figure 3.3b a significant amount of W accumulated in the center of the plasma. The central W concentration borders up $n_W/n_D = 4.10^{-3}$ therefore W is no longer a trace specie. Studies performed in [10] show that for this specific pulse, the breaking of the trace limit assumption has very little impact on the results of the modeling.

The goal of this work is to reproduce the main features of the 82722 pulse : central electron density peaking, central electron temperature dropping, and W central accumulation by predicting with JETTO the time evolution of the plasma profiles (density, temperature, rotation) as well as the W profile.

3.3 Integrated modeling tool : JETTO

3.3.1 Codes available in JETTO

The use of an integrated modeling tool is mandatory in order to evolve many quantities at the same time : particles, heat, momentum, but also heating, radiation or current. As seen in the first chapter in section 6, several integrated modeling tools exist. For our work we selected JETTO, our choice will be explained as JETTO possibilities are described.

Figure 3.4 represents the different modules of JETTO with the different codes available.

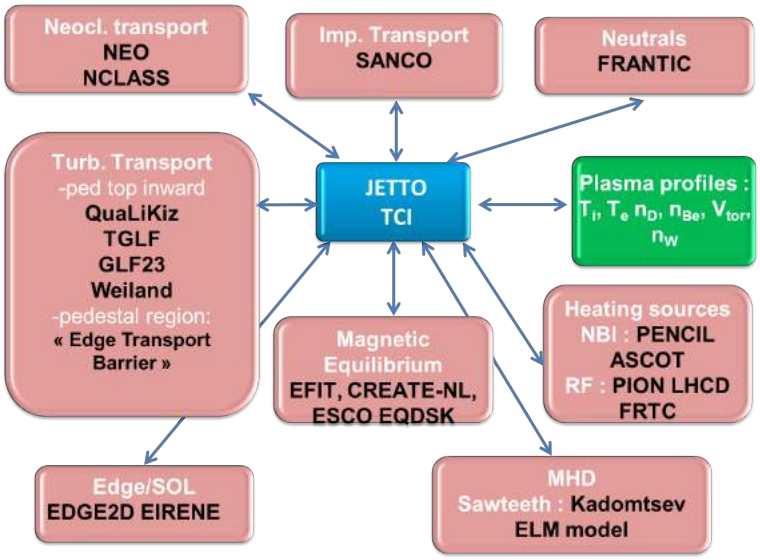

Figure 3.4 – Scheme of JETTO integrated modeling tool modules

JETTO [33, 115] is coupled to the impurity transport code SANCO [4] and solves the transport equation. SANCO evolves each ionization state of the impurity species and accounts for ionization, recombination and charge exchange. The used atomic data comes from the ADAS data base [65]. Modeling of the external heating systems is managed by PENCIL [34] or ASCOT [68] for the NBI part, and PION [46], LHCD and FRTC [47] for the RF heating. The magnetic equilibrium modeling is assured by EFIT [87] or ESCO [33], a fix boundary solver. Different kind of models are at disposal to model turbulent transport : empirical (Bohm-Gyro Bohm [45]), drift-wave models (Weiland [137], GLF23 [136], TGLF [99, 127]) or gyrokinetic (QuaLiKiz). Two models are available for neoclassical transport : NCLASS [74] and NEO [15, 17]. FRANTIC [117] models the neutrals source. Analytical models describe sawteeth with the Kadomtsev model [80], Neoclassical Tearing Modes (NTMs) and ELMs. Finally, EIRENE [112] and EDGE2D [121] assures the modeling of the scrape-off layer (SOL). The association of JETTO and the SOL codes is named JINTRAC.

3.3.2 Accomplished work using JETTO

This section proposes a non-exhaustive list of studies performed using JETTO integrated modeling. [85] models the L-H transition, including the W behavior using JINTRAC (ie JETTO/SANCO+EDGE2D and EIRENE), GLF23 and Bohm-GyroBohm, NCLASS, the continuous ELM model, PENCIL, ASCOT, PION, and HPI2 for the pellet modeling. [37] models the time evolution of density, temperature and rotation profiles using QuaLiKiz in JETTO/SANCO, coupled with PENCIL and PION. The main difference between [37] and this work is the presence of W, which requires the coupling with NEO as well as the modeling of radiation.

3.3.3 JETTO configuration : codes, assumptions and numerical settings

Figure 3.5 illustrates the JETTO configuration used for our specific case. The magenta boxes correspond to the codes that evolve self-consistently, and the grey boxes correspond to the quantities not modeled. Each code is briefly presented below, along with the corresponding numerical adjustments. Those settings are made to assure numerical stability and convergence while saving as much computation time as possible.

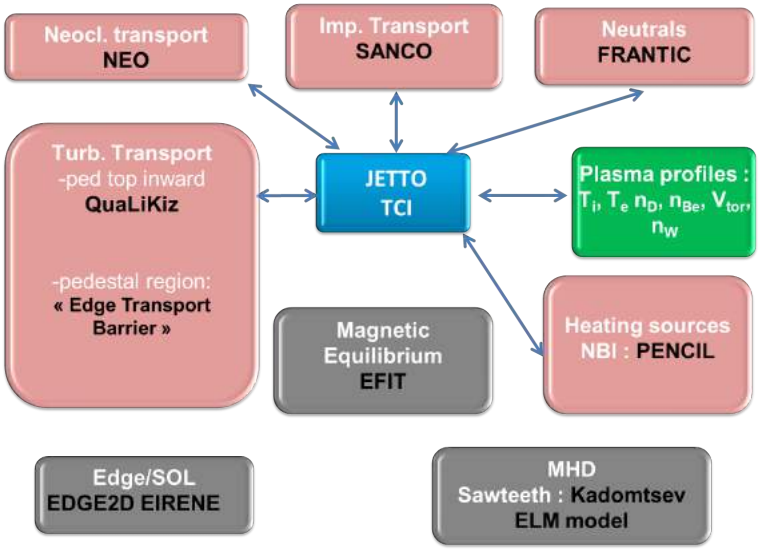

Figure 3.5 – Scheme of JETTO configuration as used in this work

For the pulse #82722 The time window 5.5s to 7.1s was chosen to be wide enough to cover several confinement times (with one confinement time of 0.4s) and at 7s the W already accumulated in the center (see figure 3.3a).

JETTO settings :	Shot Number	82722
	Number of grid points	61
	Start time (s)	45.5
	End time (s)	47.1
	Minimum timestep (s)	10^{-8}
	Maximum timestep (s)	10^{-3}
	Ion (1) mass	2
	Current boundary condition (amps)	$1.67.10^{6}$
	Electron temperature boundary condition (eV)	10^{2}
	Ion temperature boundary condition (eV)	10^{2}
	Ion Density boundary condition (cm^{-3})	$1.5.10^{13}$
	Edge velocity boundary condition (cm/s)	10^{6}
	IGLF23MSIGNCONS (sign preserving of TCI output)	1
	ITRDOWNSC (grid resolution for TCI)	25
	LAVERAGE_IONS (treat all ions consistently in TCI)	25
	TRMAXD (max diff. coeff for drift-wave models)	10^{5}

Magnetic equilibrium is not evolved in our simulations. We used instead the EFIT [87] reconstruction, a method which reconstructs the current profile parameters, the plasma shapes, and a current density profile satisfying the MHD equilibrium constraint.

SANCO models the impurity radiative losses and updates impurity gradients and densities. Especially SANCO can evolve radiative losses of heavy impurities such as W, which makes JETTO the best integrated modeling tool for our work. SANCO grid has a higher resolution on the edge and in the core. SANCO runs for the whole radius range, treats all charge states of the impurities and returns the most probable one, which is a good assumption for W. The atomic data used for W is ADAS 50, based on [108]. This choice is motivated by the fact that ADAS 50 data is consistent with the recombination rates which have been adjusted to experimental observations. [108] ADAS96 is used for Be.

SANCO settings :

	Tungsten	Berylium
Impurity mass	184	9.0129
Impurity charge	74	4
Escape velocity (cm/s)	0	0
Neutral flux (s^{-1})	10^{15}	10^{14}
Recycling factor	0	0
Abundance	1	300
IFLUS (use geometry from JETTO)	0	0
INDLIN (JETTO/SANCO profile interpolation)	2	2
ISPLITSANCOT (ratio SANCO/JETTO timestep)	100	100

The initial W content in the JETTO simulation is obtained by tuning the ratio

n_W/n_{Be} (called abundance on the SANCO board above) to match both the experimental value of $Z_{eff} = 1.34$, and the initial radiation level from bolometry diagnostic. This implies that all radiation is caused by W only. A fixed W neutral flux coming at the separatrix is also added. Note that W initial profile is constrained to be homothetic to the electron density profile, therefore the simulation starts with some W in the center. Figure 3.6 shows the W density Flux Surface Averaged (FSA) at the initial time 5.5s for the JETTO-QuaLiKiz-NEO simulation in magenta, and W density inferred from SXR-UV in black. The experimental profile shows no W in the central part at t=5.5s. Moreover, the simulation overestimates the W content at mid-radius up to a factor 2. Tuning the initial W content only based on radiation level and Z_{eff} was not the most precise method, but nonetheless this does not prevent the simulation to reproduce correctly the time evolution of the W behavior shown on figures 3.16, and 3.21 to 3.23.

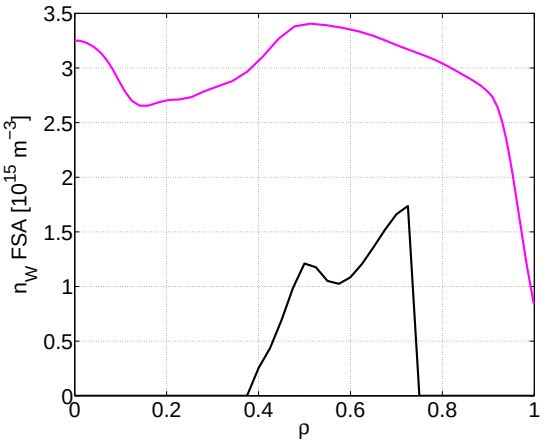

Figure 3.6 – Flux Surface Averaged W density at t=5.5s, initial time of the JETTO-QuaLiKiz-NEO simulation (magenta). Comparison with W density estimated from SXR-UV measurements (black).

NEO [15, 17] predicts neoclassical transport. Figure 3.3a shows that W presents strong poloidal asymmetries. As seen on section 3.4 in chapter 2, the combination of the analytical formula with NCLASS [74] is not accurate enough to model correctly the impact of poloidal asymmetries on neoclassical transport, making the use of a code accounting for poloidal asymmetries such as NEO necessary. Within JETTO, NEO runs for the impurity neoclassical transport over the whole radius range, from the axis to the LCFS. NEO inputs are plasma profiles (temperature, density, rotation) impurity profiles, concentrations and charges. Its outputs are, for each specie, neoclassical flux, diffusion and convection.

NEO settings :	Radial grid	16
	Minimum pitch angle polynomials	13
	NEO timestep	2.10^{-4}

For the turbulent transport, from pedestal top inward to $\rho = 0.03$, the quasi-linear gyrokinetic code QuaLiKiz is used. It is a first-principle gryo-kinetic code that accounts for trapped and passing ions and electrons, therefore Ion and Electron Temperature Gradients and Trapped Electron Mode. QuaLiKiz functioning is detailed in [22, 20, 37]. It accounts for all unstable modes and sums the flux over the wave number spectrum. It uses the shifted circle (s-α) geometry with a small inverse aspect ratio expansion. QuaLiKiz inputs are plasma profiles (temperature, density, rotation) impurity profiles, concentrations and charges. Its outputs are, for each specie, turbulent flux, diffusion and convection. Both QuaLiKiz and NEO codes are first-principle based and have a reasonable computational time. This argument is one of the reasons why JETTO was chosen for this work.

QuaLiKiz settings :

ρ_{min}	0.03
ρ_{max}	0.97
ITRTGLFSM (QuaLiKiz spatial smoothing)	3
TCISMTHTIME (Smootjing time for heat/part. diff.)	0.001
TRTGLFEPS (critical temp./dens. gradient under which heat coeff. set to 0)	0.05

The impact of the rotation is taken into account for $\rho > 0.5$ since QuaLiKiz is known to overestimate the ExB stabilization impact for high rotation values [37]. The collisions, kinetic electrons are also accounted for. The ETG scales are not included because they led to overestimated rotation predictions. A small Bohm-GyroBohm diffusion is also added (0.1% of particle diffusion coefficient, and 1% of heat diffusion coefficient) to ensure numerical stability.

The pedestal region is modeled using an "Edge Transport Barrier" (ETB). The pedestal width and the turbulent transport remains fixed during the whole simulation, with the fixed value of the diffusion tuned so that electron density and temperature profiles remain within experimental uncertainties at all times. A Prandtl number is also tuned to match the exprimental rotation. The ETB model is tuned using the code FRANTIC [129] to model neutral sources at the LCFS. A continuous ELM model, with tuned particle diffusivity and thermal conductivity was also necessary to reproduce the experimental pedestal, as in [85].

ETB settings :	Pedestal width (cm)	4
	Lower Thermal limit (cm^2/s)	5.10^3
	Lower particle ion limit (cm^2/s)	1.10^3
	Electron thermal transport multiplier	1.10^{-3}
	Ion thermal transport multiplier	1.10^{-3}
	Particle transport multiplier	1.10^{-2}
	FRANTIC gas puff target (cm^{-3})	$4.5.10^{13}$
	FRANTIC ion nominal puff rate (s^{-1})	6.10^{21}
	FRANTIC recycling coefficient	0.1
	ELM model max. transport multiplier (m^2/s)	1.10^8
	PRANDTL_ETB (Prandtl number for ETB)	0.75

ELMs and sawteeth are not modeled in our specific case, although several models are available and used in other studies [85].

The heating source, in this case NBI only, is modeled using PENCIL code [34]. PENCIL solves a simplified version of the Fokker-Planck equation and includes ionization by charge exchange, ionization by plasma electrons and ionization by plasma ions. PENCIL inputs are the ion energy, the total power and its distribution over the beams. PENCIL outputs are, in particular, the torque, electron and ion heating and particle sources.

PENCIL settings :

	Octant 4	Octant 8
Ion Mass	2	2
Ion energy (eV)	90.10^3	97.10^3
Beam fraction with E, E/2, E/3	0.51, 0.28, 0.21	0.52, 0.30, 0.18
Pini's	1, 4, 6	1, 4, 6
Normalize power to (W)	6.10^6	10.10^6

PENCIL was chosen because of its simplicity and therefore its computation low cost. In order to validate this choice, a comparison between PENCIL and NUBEAM inside TRANSP [103] is shown on figure 3.7. NUBEAM is more accurate than PENCIL because it is a Monte Carlo code that accounts for prompt losses and fast ions. At two different time slices (6s on figure 3.7a and 7s on figure 3.7b) the particle source (up) and the electron density (down) profiles are plotted. At 6s on figure 3.7a up, the PENCIL central particle source in red is two times larger than NUBEAM estimation, but the impact on the electron density is less than 10%. The same scenario happens at 7s, with a factor 3 difference on the central particle source and an impact of 10% on the electron density. This demonstrates that the accuracy of PENCIL is sufficient.

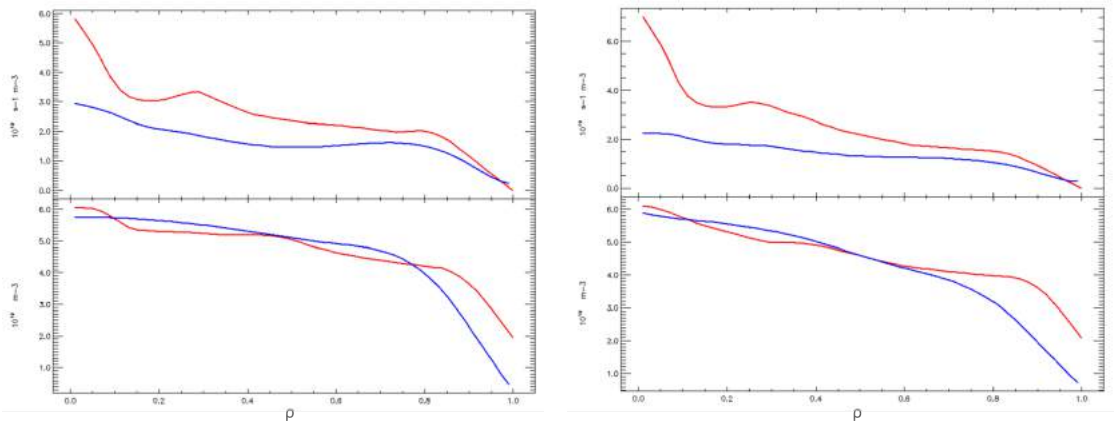

(a) NUBEAM/PENCIL comparison at t=6s. (b) NUBEAM/PENCIL comparison at t=7s.

Figure 3.7 – Comparison between NUBEAM (blue) and PENCIL (red) : particle source profile (up) and n_e profile (down)

3.4 JETTO predictions versus experiments

In this section we compare the experimental data with the self-consistently predicted profiles from JETTO combined with, in particular, NEO and QuaLiKiz.

3.4.1 Timetraces of the plasma parameters

Figures 3.8 to 3.15 present timetraces of several plasma parameters which are self-consistently and simultaneously evolved in the simulation : density, temperature, rotation, current, heating and impurity profiles. For each parameter, the JETTO-NEO-QuaLiKiz simulation is shown in magenta, and compared with experimental data when available. Timetraces are shown at three ρ positions : 0.1, 0.4, and 0.75.

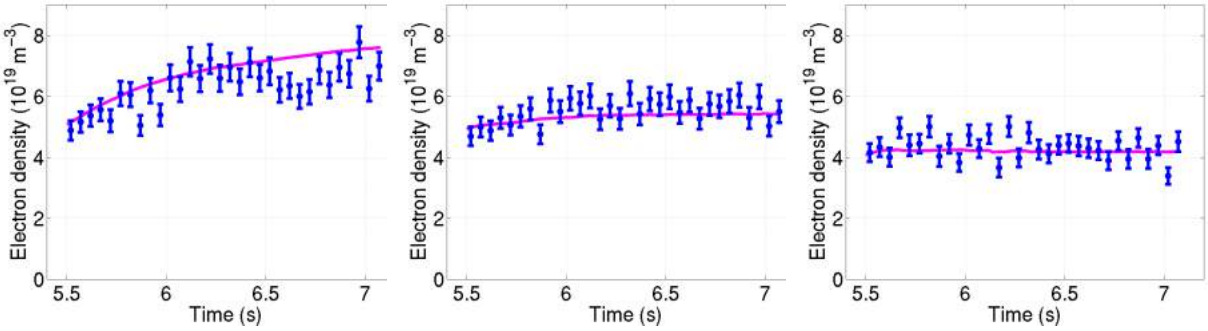

(a) ρ=0.1 (b) ρ=0.4 (c) ρ=0.75

Figure 3.8 – Electron density timetraces : comparison between JETTO-QuaLiKiz prediction and HRTS measurements at different ρ

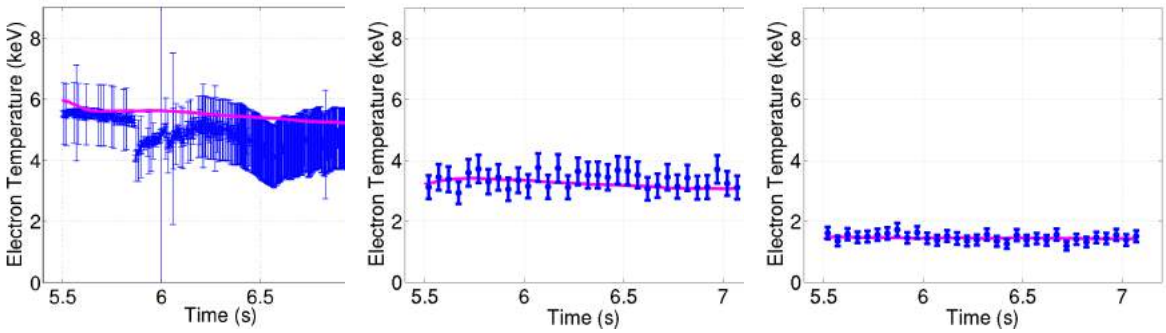

(a) ρ=0.1 (b) ρ=0.4 (c) ρ=0.75

Figure 3.9 – Electron temperature timetraces : comparison between JETTO-QuaLiKiz prediction and ECE at $\rho = 0.1$/HRTS measurements at $\rho = 0.4 - 0.75$

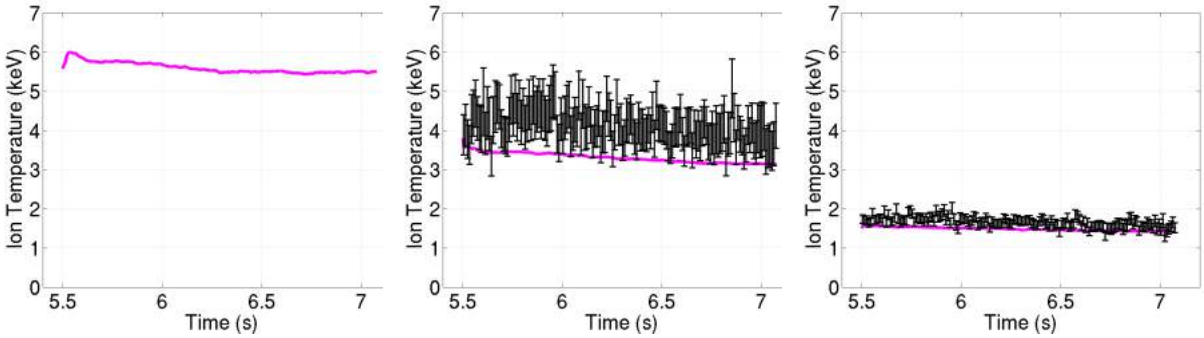

(a) ρ=0.1 (b) ρ=0.4 (c) ρ=0.75

Figure 3.10 – Ion temperature timetraces : comparison between JETTO-QuaLiKiz prediction and Charge Exchange measurements at different ρ

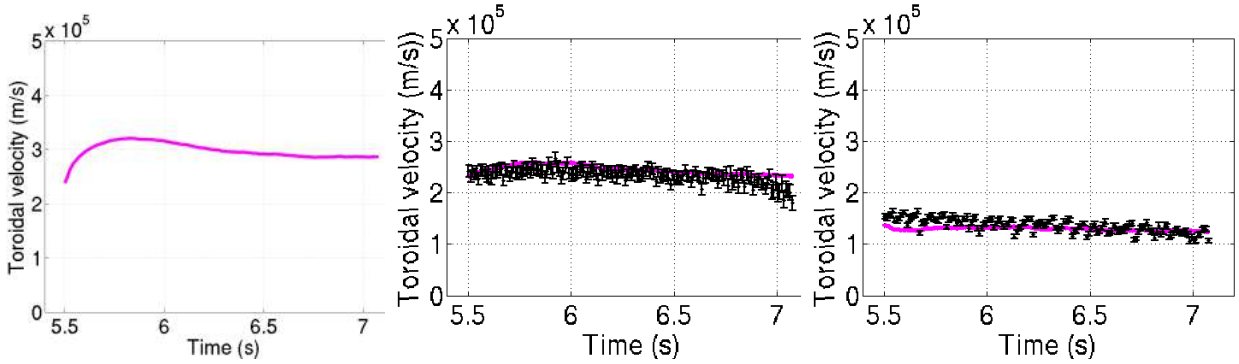

(a) ρ=0.1 (b) ρ=0.4 (c) ρ=0.75

Figure 3.11 – Toroidal rotation timetraces : comparison between JETTO-QuaLiKiz prediction (magenta) and Charge Exchange measurements at different ρ

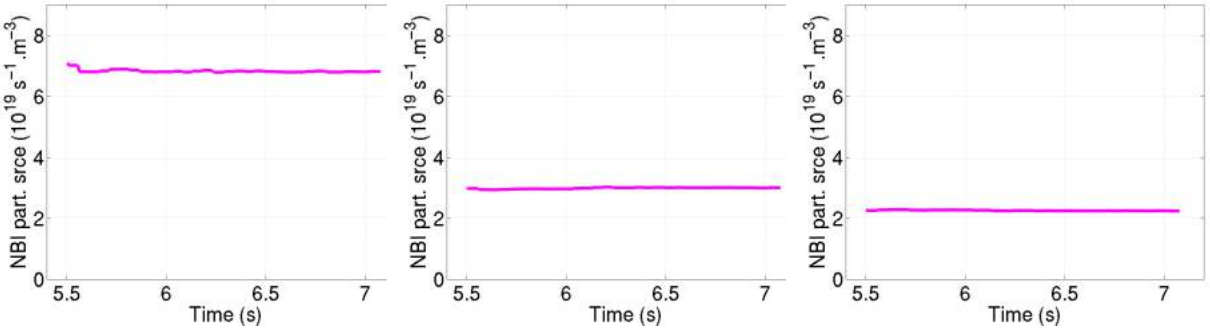

(a) ρ=0.1 (b) ρ=0.4 (c) ρ=0.75

Figure 3.12 – Timetraces of JETTO-QuaLiKiz prediction for NBI particle source at different ρ

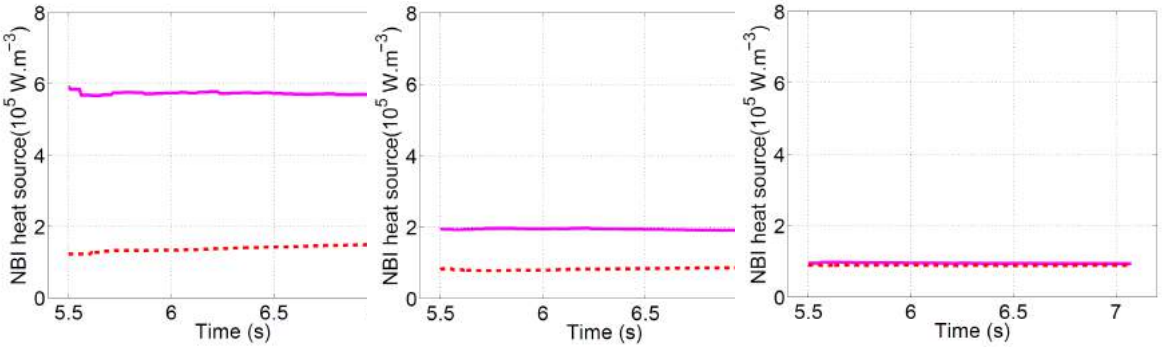

(a) ρ=0.1 (b) ρ=0.4 (c) ρ=0.75

Figure 3.13 – Timetraces of JETTO-QuaLiKiz prediction for NBI heat source (ion in magenta solid line and electron in red dashed line) at different ρ

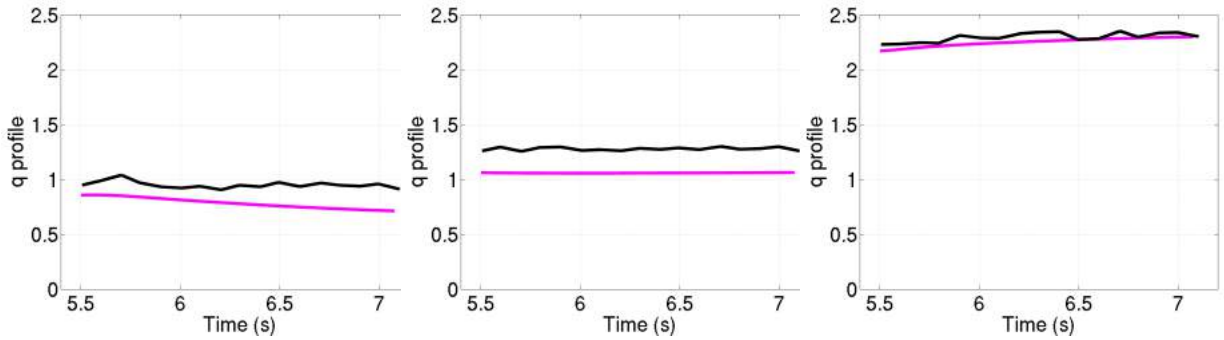

(a) ρ=0.1 (b) ρ=0.4 (c) ρ=0.75

Figure 3.14 – Safety factor timetraces : comparison between JETTO-QuaLiKiz prediction (magenta) and EFTF reconstruction at different ρ

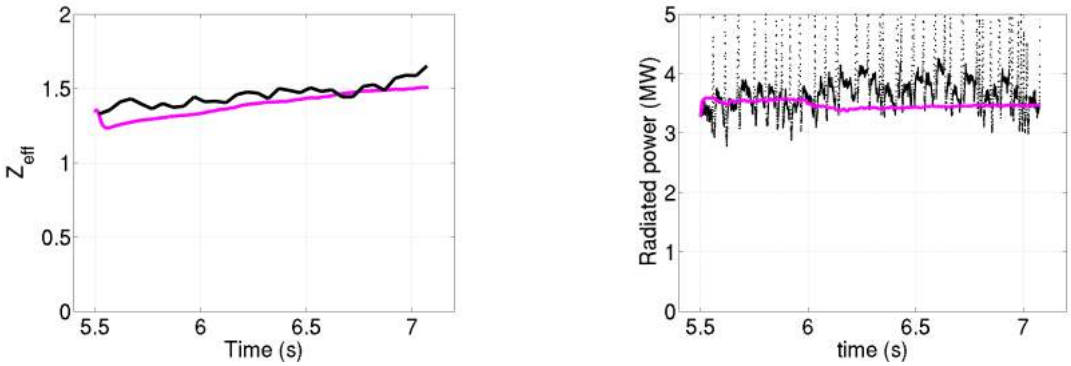

(a) Z_{eff} (b) Integrated radiation over time

Figure 3.15 – Z_{eff} and radiation timetraces : comparison between JETTO-QuaLiKiz prediction (magenta) and measurements at different ρ

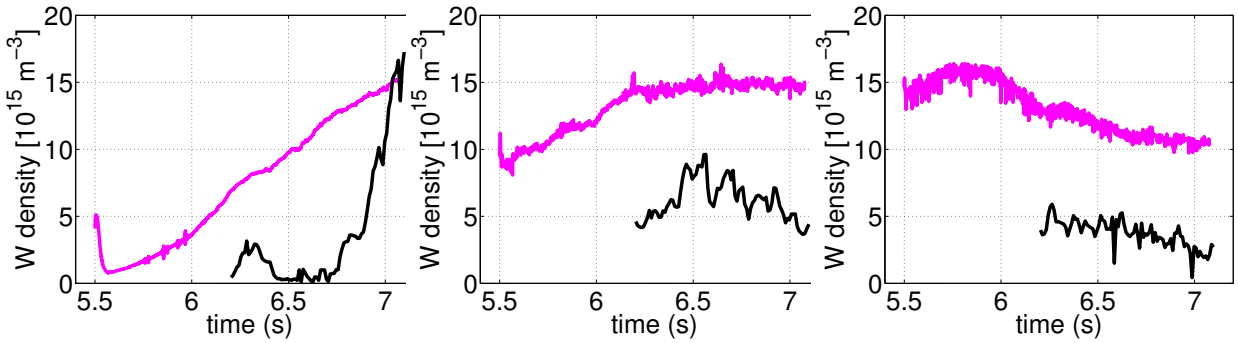

(a) ρ=0.1 (b) ρ=0.4 (c) ρ=0.75

Figure 3.16 – W density timetraces : comparison between JETTO-QuaLiKiz prediction (magenta) and estimation from SXR-UV measurements at different ρ

Figures 3.8 show the time evolution of electron density. The electron density prediction must be accurate in order to simulate properly the W transport, due to the main ion density gradient dependence of the W neoclassical transport as seen on equation 51 from chapter 2. The prediction of the central density peaking especially needs to be accurate in order to predict correctly the central W accumulation. On figure 3.8a close to the center the predicted density increases smoothly. The HRTS measurements, while also globally increasing, are impacted by the sawteeth. The simulation does not take sawteeth into account, therefore the local gradients are not well captured. For the two other radial position, the predicted density does not vary much, and mostly stays within experimental uncertainties with a maximum error of 25%. Overall QuaLiKiz globally captures the experimental central electron density peaking, even if all the subtle features are not reproduced due to the non-simulation of the sawteeth.

Figures 3.9 show the electron temperature. Similarly to the electron density case, the JETTO-QuaLiKiz simulation successfully captures the decreasing trend of central ECE measurements on figure 3.9a, but misses the sawtooth crashes, leading to inaccurate estimation of the local gradients. Around mid-radius (figure 3.9b) and close to the pedestal (figure 3.9c), the experimental temperature remains quite steady and JETTO-QuaLiKiz estimations lie within experimental uncertainties over time.

Ion temperature and toroidal rotation are not compared with experimental data in the center (figures 3.10a and 3.11a) due to the lack of charge exchange measurements. Profiles shown later on figure 3.20 and 3.21 illustrate that JETTO-QuaLiKiz central estimations are coherent. Moreover, assuming that $T_i \simeq T_e$ and comparing with 3.9a, QuaLiKiz predicts the ion temperature equal the electron temperature within 10%, which seems coherent. At $\rho = 0.4$ on figure 3.10b, JETTO-QuaLiKiz predictions tend to underestimate the charge exchange measurements by a maximum of 15% (calculated from the lower bound of the error bar). This can be explained by the fact that QuaLiKiz is an electrostatic code and

does not include nonlinear electromagnetic stabilization of ITG due to fast ions (see [37] and references therein).

Toroidal rotation predictions mostly lie within experimental uncertainties, except at early times at $\rho = 0.75$. Overall the experimental toroidal velocity remains quite constant over time. Note that the plasma rotates up to 30km/s, which leads to W Mach number around 2. According to chapter 2 section 3.4 and as seen later on the W distribution, this creates strong poloidal asymmetries on W and justifies the use of NEO in the integrated modeling configuration.

Figures 3.12 and 3.13 show the NBI particle and heat sources over time, self-consistently simulated by PENCIL. Note that the particle source in the center (figure 3.12a) is two times bigger than the one at mid-radius, which is consistent with the central electron density peaking seen on figure 3.8a, even if the peaking is limited by the sawteeth. As for the heating, figure 3.13 show that the ion heating is more important than the electron heating in the central area of the plasma.

The predictions of safety factor evolution are shown on figure 3.14. Note that, in the JETTO-QuaLiKiz-NEO simulation, the current evolves according to the current diffusion equation, but the equilibrium shape does not evolve accordingly since the magnetic equilibrium is not self-consistently simulated. The simulated q profile globally reproduces the profile reconstructed from EFTF equilibrium file, with a maximum error of 25$\%$. EFTF magnetic equilibrium is reconstructed using the same method as EFIT, with the addition of Faraday rotation constraint [59]. Note that JETTO-QuaLiKiz predictions tend to underestimate the EFTF reconstruction, which means that the q=1 position is also shifted.

Figure 3.15a shows the average Z_{eff} time evolution and figure 3.15b shows the total radiated power over time. The Z_{eff} globally increases with time, which can be explained by the fact that W contribution to Z_{eff} increases also with time. The total radiated power on the other hand varies but shows no sign of W accumulation. This can be a bit surprising since other discharges with W central accumulation showed a significant radiation increase [78]. The simulated radiation level does not vary much with time, which is consistent with the experimental signal. Even if the simulation does not capture all the small variations of the measurement, the error does not exceed 30$\%$. The radiation timetrace shows no sign of the W central accumulation because, as seen on equation 3.2, the radiation level due to the W depends on the cooling factor L_W^{SXR}. The cooling factor, illustrated on figure 8 in chapter 1, is maximized around T=1.5 keV. According to figure 3.18, T_e approaches this value in the outter radius, from which comes most of the radiated power. This explains why the central W accumulation is not visible on the timetrace of the total radiated power.

Figures 3.16 show the time evolution of the W content. The initial W content was estimated from the total radiation shown on figure 3.15b. In the central part, the simulated W density slowly and regularly increases, with a factor 3 increase between 6s and 7s. The experimental W accumulates a little at 6.3s before being flushed out. From 6.7s to the end of the time window, W strongly accumulates

with a factor 10 increase. It is coherent that the simulation does not account for the flushing out phenomenon since the sawteeth are not modeled, but even without it the simulation gets the trend that the W is accumulating, showing that the modeling of neoclassical and turbulent transports only is sufficient to reproduce the global trend of the W accumulation. The predicted W content at $\rho = 0.4$ and $\rho = 0.75$ overestimates the measurements up to a factor 2.

The goal of this work is to quantify how accurately the integrated modeling simulation self-consistently reproduces the experimental story of the 82722 pulse. JETTO-QuaLiKiz-NEO predictions are reliable over time for all of the four channels (density, temperatures and rotation), and this result is the first of its kind, along with [37], also with QuaLiKiz, and [125] with TGLF. The quality of the predictions enables a correct estimation of the W central accumulation. To deepen the analysis of the quality of the JETTO-QuaLiKiz-NEO predictions, the next section focuses on several profiles at different time slices, and 2D poloidal cuts of the W distribution.

3.4.2 Plasma profiles

3.4.2.1 Electron density

In order to further validate QuaLiKiz predictions, figure 3.17 shows electron density profiles at three different times : 6.2s after 0.7s of simulation (figure 3.17a), 6.8s after 1.3s of simulation (figure 3.17b) and 7s, after 1.5s of simulation (figure 3.17c). Both HRTS and LIDR are shown on figure 3.17 but we shall compare the simulation with HRTS only because of its higher time and space resolutions.

On figure 3.17a at 6.2s, QuaLiKiz predictions in magenta lie within experimental uncertainties of the HRTS in blue for the whole radius, except close to the axis where QuaLiKiz smoothes the local variations. The predicted pedestal is modeled by the ETB which has be tuned to match the experimental data. On figure 3.17b at 6.8s, QuaLiKiz prediction lies within experimental uncertainties from R=3.3m outward. But from R=3.3m inward, the experimental density dropped because of a sawtooth, therefore QuaLiKiz overestimates the central electron density. The experimental pedestal is stable and well captured by the Edge Transport Barrier modeling. On figure 3.17c at 7s after 1.5s of simulation, HRTS shows strong local gradients, especially close to the axis at R=3.1m. The pedestal is slightly shifted outward, therefore the Edge Transport Barrier no longer lies within experimental uncertainties. QuaLiKiz captures the global increase of the electron density and lies within experimental uncertainties. However it does not really reproduces the stiff central gradient shown by the measurements and smooths it out. This impacts the W transport as seen in the next section.

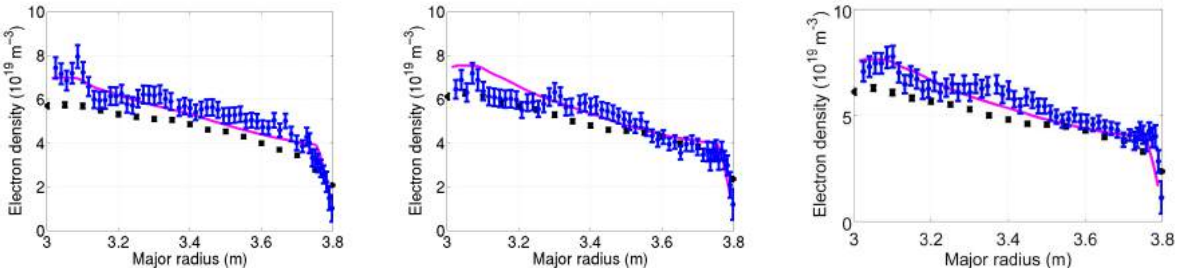

(a) Experimental and predicted n_e at t=6.2s after .7s of simulation.

(b) Experimental and predicted n_e at t=6.8s after 1.3s of simulation.

(c) Experimental and predicted n_e at t=7s after 1.5s of simulation.

Figure 3.17 – Comparison of experimental (LIDR in black HRTS in blue) and predicted (magenta solid line) electron density profiles

3.4.2.2 Electron and ion temperatures

The electron and ion temperature predictions are then compared with experimental data. The electron temperature profiles are first showed on figure 3.18 : at 6.2s after 0.7s of simulation (figure 3.18a), at 6.8s after 1.3s of simulation (figure 3.18b) and at 7s after 1.5s of simulation (figure 3.18c). QuaLiKiz predictions are in magenta solid line, and the HRTS measurements in blue.

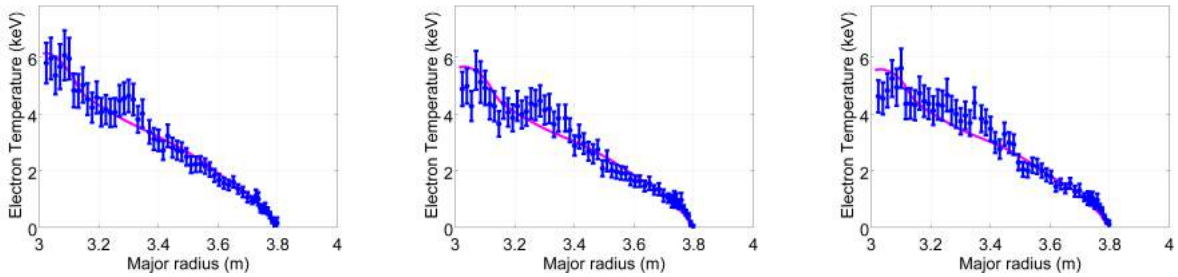

(a) Experimental and predicted T_e at t=6.2s after .7s of simulation.

(b) Experimental and predicted T_e at t=6.8s after 1s of simulation.

(c) Experimental and predicted T_e at t=7s after 1.5s of simulation.

Figure 3.18 – Comparison of experimental (HRTS in blue) and predicted (magenta solid line) electron temperature profiles

QuaLiKiz predictions show the same trends for the temperature that it did for the density. On figure 3.18a at 6.2s, QuaLiKiz predictions in magenta lie within experimental uncertainties of the HRTS in blue for the whole radius, except at R=3.3m where QuaLiKiz misses a bump and slightly underestimates the measurements. On figure 3.18b at 6.8s, the HRTS shows a global decrease of the electron temperature, while keeping the central peaking and the bump at R=3.3m. The experimental pedestal remains unchanged and well reproduced

by the Edge Transport Barrier. QuaLiKiz predicts the global decrease of the electron temperature, but still misses the bump at R=3.3m. QuaLiKiz predicts the central peaking and slightly overestimates it. On figure 3.18c at 7s after 1.5s of simulation, the bump at R=3.3m disappeared while a drop appeared at R=3.5m. QuaLiKiz predictions barely changed compared with 3.18b. Therefore it misses the drop at R=3.5m while staying within experimental uncertainties. Qualikiz still overestimates the very central temperature.

Now the ion temperature profiles are showed on figure 3.19 : at 6.2s after 0.7s of simulation (figure 3.19a), at 6.8s after 1.3s of simulation (figure 3.19b) and at 7s after 1.5s of simulation (figure 3.19c). QuaLiKiz predictions are in magenta solid line, and the Charge Exchange measurements are in black for most of the radial points, and blue for the pedestal.

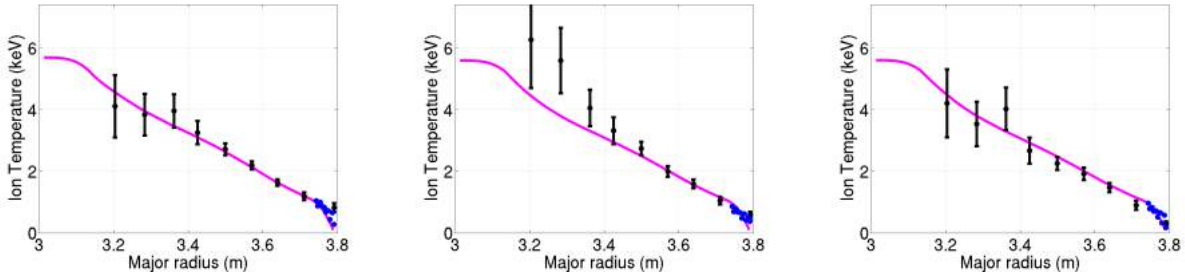

(a) Experimental and predicted T_i at t=6.2s after .7s of simulation.

(b) Experimental and predicted T_i at t=6.8s after 1s of simulation.

(c) Experimental and predicted T_i at t=7s after 1.5s of simulation.

Figure 3.19 – Comparison of experimental (Charge exchange in dark) and predicted (magenta solid line) ion temperature profiles

On figure 3.19a at 6.2s, QuaLiKiz predictions in magenta lie within experimental uncertainties of the Charge Exchange for the whole radius. On figure 3.19b at 6.8s, the Charge Exchange shows a global increase of the ion temperature, up to 50% at R=3.2m. QuaLiKiz predictions remain almost unchanged and therefore underestimates the measurements by a maximum of 15% (calculated from the lower bound of the error bar). The possible reasons for this underestimations are already developed in the previous section. On figure 3.19c at 7s after 1.5s of simulation, measured ion temperature slightly decreased at R=3.25-3.4m. QuaLiKiz predictions barely changed compared with 3.19b. Therefore it still underestimates the measurements at R=3.25-3.4m.

3.4.2.3 Rotation

The last plasma parameter to study is the toroidal rotation, shown on figure 3.20 : at 6.2s after 0.7s of simulation (figure 3.20a), at 6.8s after 1.3s of simulation (figure 3.20b) and at 7s after 1.5s of simulation (figure 3.20c). QuaLiKiz

predictions are in magenta solid line, and the Charge Exchange measurements are in black for most of the radial points, and blue for the pedestal.

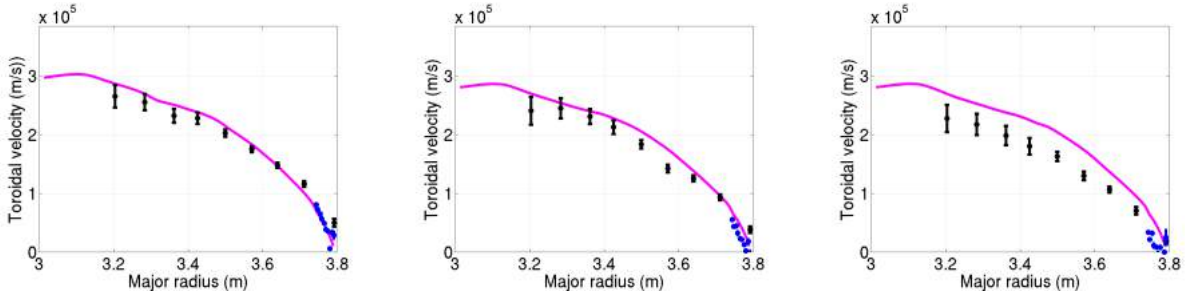

(a) Experimental and predicted V_{tor} at t=6.2s after .7s of simulation.

(b) Experimental and predicted V_{tor} at t=6.8s after 1s of simulation.

(c) Experimental and predicted V_{tor} at t=7s after 1.5s of simulation.

Figure 3.20 – Comparison of experimental (Charge exchange in dark) and predicted (magenta solid line) toroidal rotation profiles

On figure 3.20a at 6.2s, QuaLiKiz predictions in magenta lie within experimental uncertainties of the Charge Exchange for the whole radius. The central part also lacks experimental measurements. On figure 3.20b at 6.8s, the Charge Exchange shows a slight global decrease of the toroidal rotation, especially at R=3.5-3.65m. QuaLiKiz predicts the global decreasing but overestimates the strongest decrease of the measurements at R=3.5-3.65m. Finally on figure 3.20c at 7s after 1.5s of simulation, measured velocity profile slightly smooths out and the pedestal moves slightly. QuaLiKiz predictions barely changed compared with 3.20b. Therefore it slightly overestimates the measurements at R=3.3-3.7m and the Edge Transport Barrier model, which does not evolve, misses the pedestal.

3.4.3 W poloidal cuts

To analyze more precisely the time evolution of the W profile, figures 3.14, 3.15 and 3.16 below shows 2D maps of the W density at three different times : t=6.2s after .7s of simulation, t=6.8s after 1.3s of simulation and t=7s after 1.5s of simulation. W densities estimated from SXR-UV measurements are on the right, predictions are on the left.

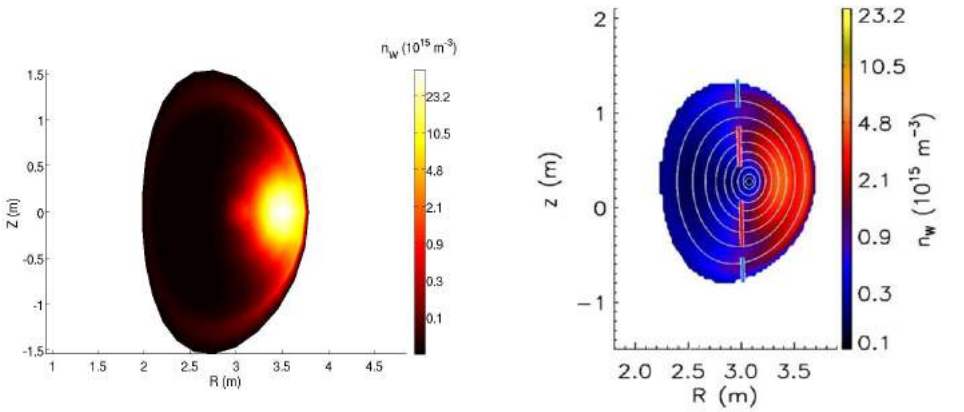

(a) Predicted n_W at t=6.2s after .7s of simulation.

(b) Experimental estimated n_W at t=6.2s after .7s of simulation.

Figure 3.21 – Comparison of estimated W density from SXR-UV measurements (right) and predicted W density (left)at t=6.2s after .7s of simulation

On figure 3.21, one can see that the amount of W in the simulation is of the order of magnitude $10^{15}m^{-3}$. Strictly looking at the absolute values, the simulated W content is about 3 times larger compared with the estimation from measurements. The initial amount of W was estimated from total radiation (see figure 3.15b) with an error of 30%, and the initial W profile in the simulation is homothetic to the electron density profile. Moving to the distribution of the W, the experimental W presents strong poloidal asymmetries, and so does the simulation, showing that NEO predicts accurately poloidal asymmetries. Note that one the simulation some W already moved towards the center. This is caused by the fact that the starting W profile in the simulation is homothetic to the electron density profile (see figure 3.6).

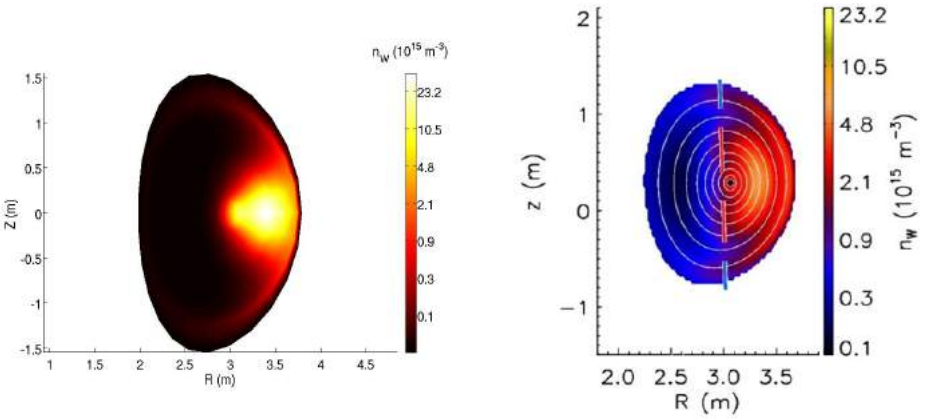

(a) Predicted n_W at t=6.8s after 1.3s of simulation.

(b) Experimental estimated n_W at t=6.8s after 1.3s of simulation.

Figure 3.22 – Comparison of estimated W density from SXR-UV measurements (right) and predicted W density (left) at t=6.8s after 1.3s of simulation

On figure 3.22 at t=6.8s after 1.3s of simulation, the predicted W amount is moving towards the center, as also seen on the estimation from measurements. The estimated W content from measurements also increased compared with t=6.2s, reducing the error on absolute W density values to a factor 2.

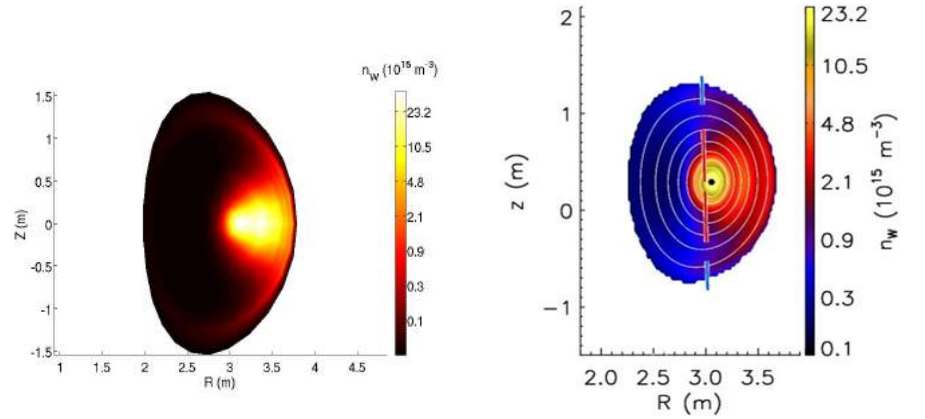

(a) Predicted n_W at t=7s after 1.5s of simulation.

(b) Experimental estimated n_W at t=7s after 1.5s of simulation.

Figure 3.23 – Comparison of estimated W density from SXR-UV measurements (right) and predicted W density (left) at t=7s after 1.5s of simulation

At the end of the simulation, after 1.5s at t=7s, the estimation from measurement on figure 3.16b shows that most of the W moved towards the center and

accumulated. On the simulation, most of the W kept moving towards the center, but not fast enough and a significant W amount is still present at mid radius, causing the simulated ratio from figure 3.13 to under estimate the experimental W ratio by a factor 2. However the time evolution of the W behavior definitely shows a trend of core accumulation.

Three phenomena can explain why the simulation does not fully succeed in transporting all the W to the plasma center. The first explanation is that the simulation does not model sawteeth and therefore some transport mechanisms can be missed. The second possibility is that the initial W profile, with some W already in the center, impacts the radiation profile and therefore modifies the density and temperature profiles, distorting the initial situation of the simulation. The third explanation could be that QuaLiKiz, as seen on figure 3.17 globally captures the global central density peaking but does not fully reproduce all the local gradients, especially at mid-radius and in the center. This could lead to under estimated neoclassical transport and therefore a weaker central accumulation.

Overall, the accuracy of the QuaLiKiz predictions of the main plasma profiles, especially electron density and rotation, allows NEO to correctly estimate the W neoclassical transport and therefore successfully reproduce the W central accumulation.

3.5 Actuators leading to W accumulation

The simulation successfully predicts self-consistently and simultaneously the plasma profiles evolution, as well as the W central accumulation. In this section the actuators leading to the accumulation are studied more closely. According to equation 51 from chapter 2, two main physical parameters impact the W neoclassical flux : the density gradient and the P_A^{model} and P_B^{model} factors accounting for poloidal asymmetries. Both can be modified through the NBI injection : the first one via the position of the fuelling, the second is linked with the toroidal rotation. In this section the NBI settings are varied to study the impact of the central particle fuelling and the angular momentum input on the W transport.

3.5.1 Central particle fuelling

As seen in chapter 2 section 2.4, the main ion gradient density has an unfavorable impact on the W neoclassical flux : the stiffer the density gradient, the more inward the W flux. In the case of 82722, the particle fuelling is stronger in the central part (see figure 3.13a), causing the central electron density to peak (figure 3.8a), and thus by ambipolarity the central main ion density peaks too. This increases the W neoclassical transport towards the axis, which definitely participates to the W central accumulation.

In order to confirm the link between central particle fuelling and central W accumulation, two new simulations are set : one with the particle injection artificially set to zero in PENCIL settings (in blue in the figures below), and the

other with partial off-axis particle source (in red). Figure 3.24a illustrates the NBI particle source profile at 6.5s : in magenta the simulation that was analyzed in the previous section, called from now on the reference simulation ; in blue the simulation with NBI particle source set to zero ; in red the simulation with partial off-axis particle source. Note that in the reference simulation the particle source is strongest close to the axis, explaining the central electron density increasing with time on figure 3.8a. In the case of the partially off-axis particle source, the central particle fuelling is reduced by 45%.

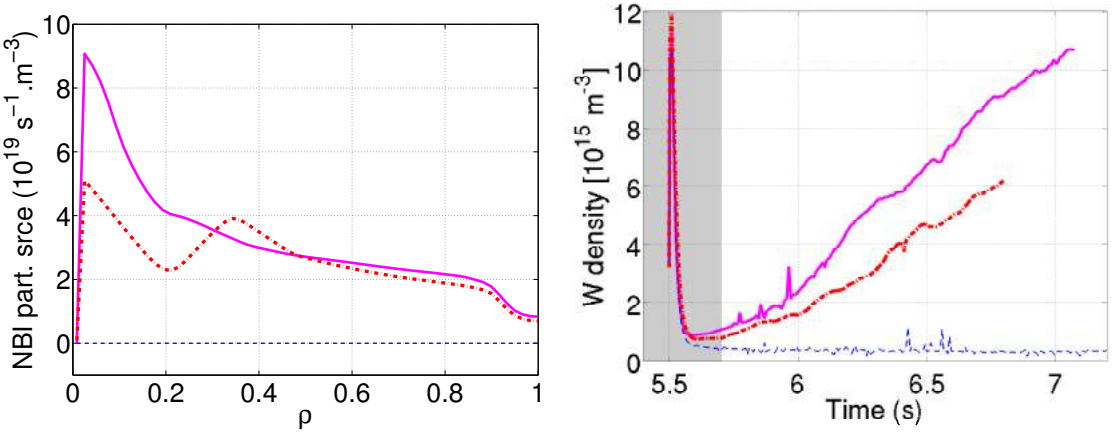

(a) NBI particle source profile at t=6.5s. (b) W density over time at ρ=0.05 at $\theta = 0$.

Figure 3.24 – Study of the impact of central NBI particle source on W accumulation. Reference simulation (magenta), simulation with NBI particle source at zero (blue) and partial-off axis particle souce (red)

Figure 3.24b shows the W density over time at ρ=0.1, close to the axis. The shaded section on figure 3.24b from t=5.5s to t=5.7s corresponds to the first simulated confinement time, needed for the simulation to move away from initial conditions. The removal of the central density source completely cancels the W accumulation phenomenon, highlighting the impact of the electron density gradient in the W transport. With a 45 % reduction of the central particle source, the central W density is limited, with a reduction of 42%.

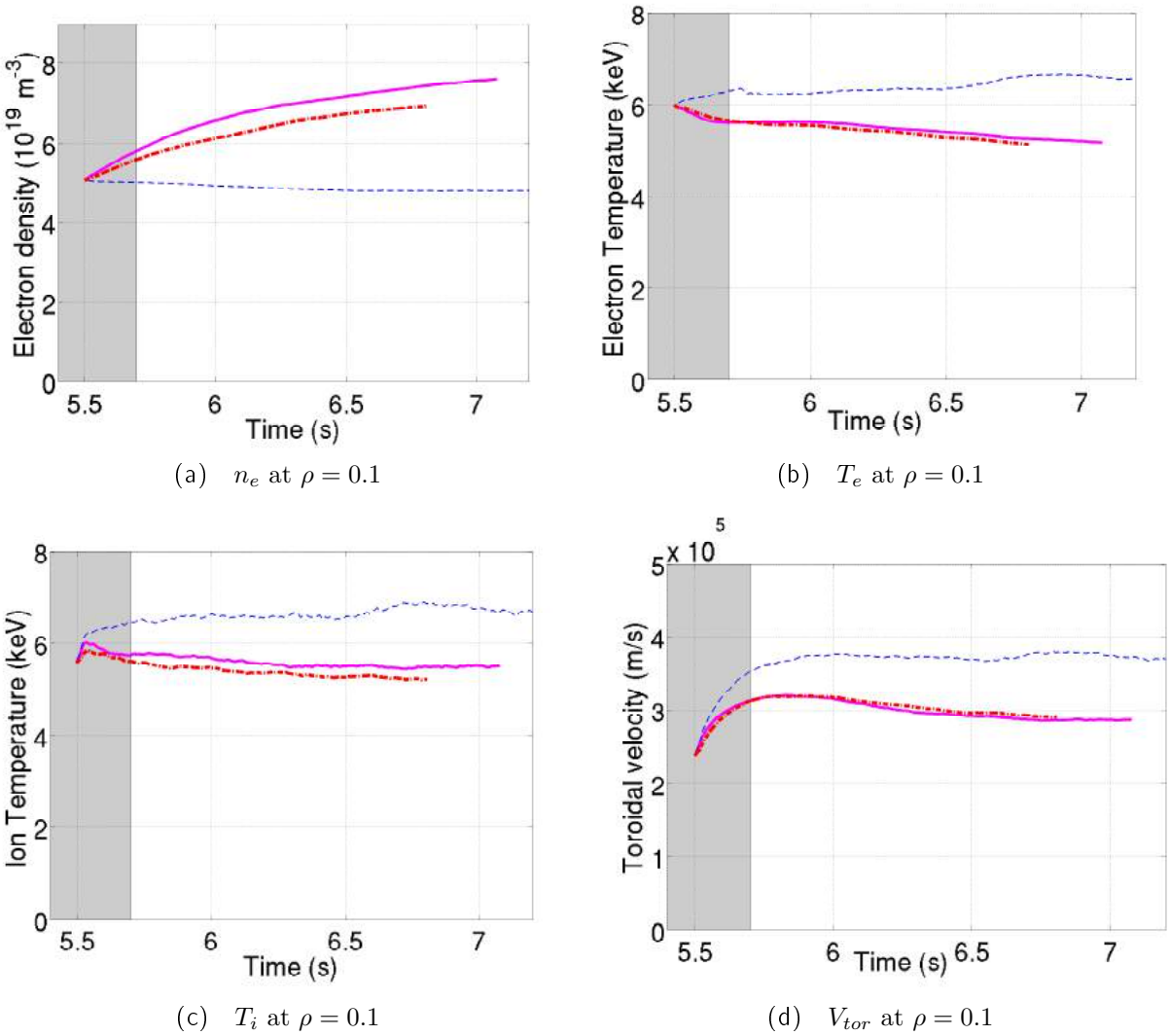

(a) n_e at $\rho = 0.1$

(b) T_e at $\rho = 0.1$

(c) T_i at $\rho = 0.1$

(d) V_{tor} at $\rho = 0.1$

Figure 3.25 – Density, temperatures and toroidal rotation over time at $\rho = 0.1$. Reference simulation (magenta), no NBI particle source (blue), partially off-axis NBI particle source (red)

Figure 3.25 show the density, temperatures and rotation timetraces at $\rho = 0.1$. For all those parameters, simulations can be divided in two groups : reference simulation and the simulation with partial off-axis source which share the same trends, and the no particle source simulation which has a specific behavior. First let us look at the electron density on figure 3.25a. The removal on the central particle fuelling cancels the central electron density peaking, which is expected. The other two simulations have an increasing central electron density. The reduction of central fuelling by 45% in red leads to a reduction of the central density peaking by only 25%.

The same trends are observed on ion and electron temperatures and for the rotation. The reference simulation and the simulation with partial off-axis source

share decreasing central temperatures and rotation, while these parameters remain constant for the simulation with no central particle source. This comes from the fact that, with no central particle fuelling, W does not accumulate, so the radiation level remains unchanged and the temperatures and rotation are not affected.

Overall this study demonstrates the direct link between the central particle fuelling and the W central accumulation. This is encouraging for devices such as WEST or ITER, which do not use NBI central particle fuelling.

3.5.2 Toroidal rotation

The other parameter impacting significantly the W neoclassical transport is the rotation. Indeed, rotation modifies the poloidal asymmetries, accounted for in P_A and P_B terms in equation 51 in chapter 2. In this specific JET-ILW pulse, these geometrical factors enhance the neoclassical convection up to a factor 40. Such big values are caused by the very important toroidal rotation shown on figure 3.3a. In order to study the impact of the rotation on the W central accumulation, figure 3.26 shows a comparison between the reference simulation in magenta and a simulation with no toroidal rotation in blue. The profile of the toroidal rotation is shown of figure 3.26a, the time evolution of the central W density is shown on figure 3.26b.

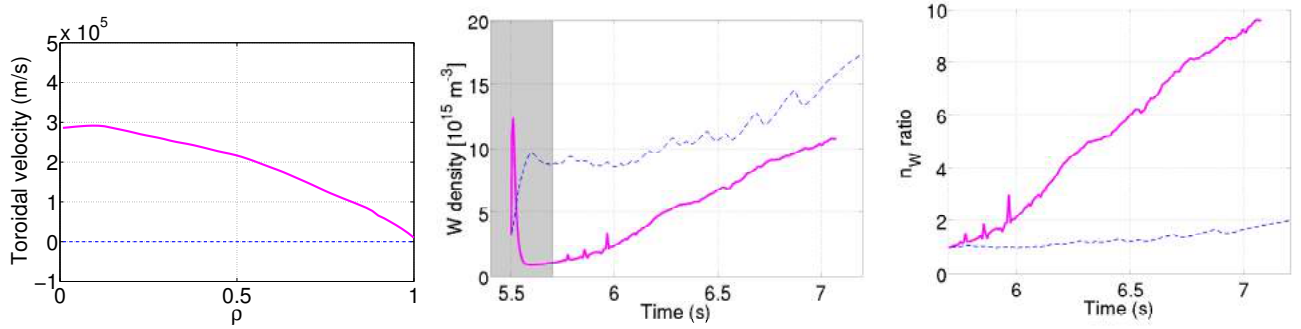

(a) Toroidal velocity profile at t=6.5s. (b) W density over time at ρ=0.1. (c) W density over time at ρ=0.1.

Figure 3.26 – Study of the impact of toroidal velocity on W accumulation. Reference simulation (magenta) versus simulation with toroidal rotation at zero (blue)

On figure 3.26b, during the first time confinement in the shaded area, for the reference simulation in magenta, the central W content drops before increasing again. Indeed W time scale is much shorter than the energy confinement time scale. However, for the simulation with no toroidal rotation, the W content remains stable and then increases. This makes the two simulations not directly comparable. In order to remove the effect of the first confinement time on W density, figure 3.26c shows the timetrace of W density normalized to its value at

the end of the first confinement time, at t=5.7s. Without the toroidal rotation, W central content doubles over time, while in presence of toroidal rotation, the W density increases by a factor 10. This clearly illustrates that the toroidal rotation plays a role in the W central accumulation process.

The removal of the toroidal rotation causes the two simulations to have very different early phases and therefore completely different time evolutions. We shall focus on the first confinement time in order to understand the mechanisms leading to such a big difference.

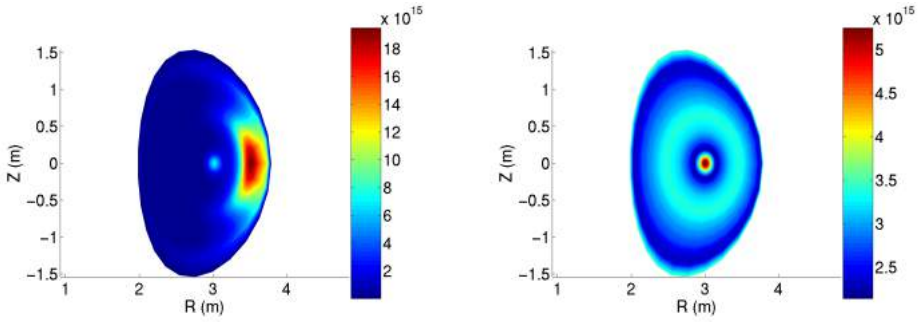

(a) Reference simulation (b) Simulation with no rotation

Figure 3.27 – W 2D maps at t=5.55s. Reference simulation (left) simulation with no rotation (right)

As mentioned earlier, the initial W density profile is homothetic to the electron density profile, therefore some W is already present in the center at the start of the simulation. Figure 3.27 show 2D poloidal cuts of the W density after 0.05s of simulation. In absence of toroidal rotation on figure 3.27b, the W is equally distributed in the plasma and no longer undergoes poloidal asymmetries, which strongly affects its transport. Figures 3.28 shows the W transport coefficients at the end of the first confinement time, at t=5.7s, time averaged over 0.1s to smooth the QuaLiKiz predictions.

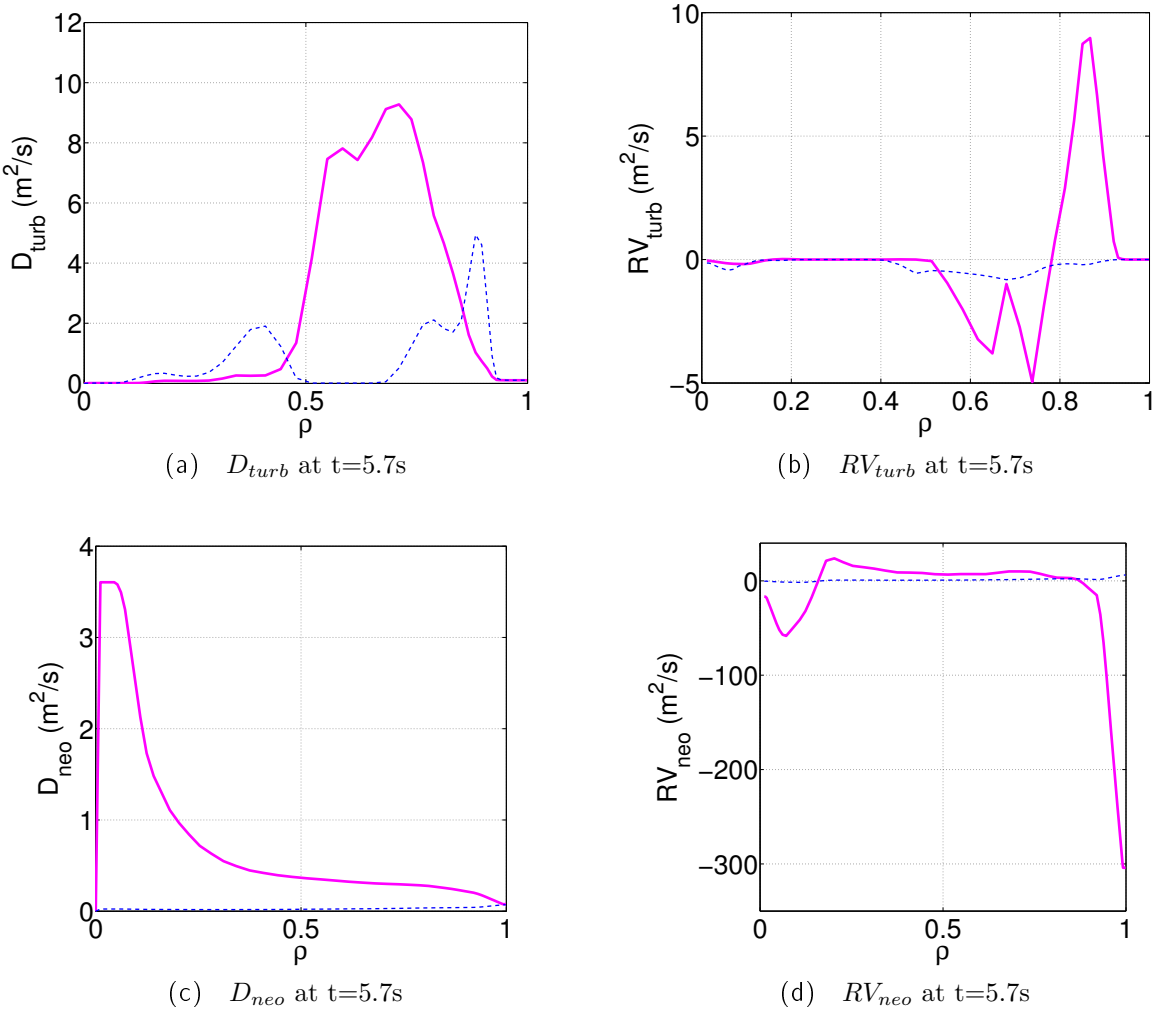

(a) D_{turb} at t=5.7s

(b) RV_{turb} at t=5.7s

(c) D_{neo} at t=5.7s

(d) RV_{neo} at t=5.7s

Figure 3.28 – W transport coefficients at t=5.7s, time averaged over 0.1s. Reference simulation (magenta), no toroidal rotation (blue)

As expected from equation 51 in chapter 2, the removal of the rotation reduces by a factor P_A, ie about 30, the neoclassical diffusion and convection (on figure 3.28c and 3.28d). The absence of rotation seems to also impact turbulent transport by reducing the turbulent convection and diffusion up to a factor 10, which can be surprising. In order to study this unexpected turbulence reduction, a QuaLiKiz standalone simulation is ran. In this standalone simulation, the parallel velocity is scanned, while fixing all the other inputs at their value from the reference JETTO simulation at t=5.7s at ρ=0.7. Figure 3.29 shows the W particle turbulent effective diffusion calculated by QuaLiKiz standalone. The magenta circle corresponds to the D Mach number of the reference JETTO simulation, at t=5.7s at ρ=0.7. The blue star corresponds to the particle diffusion with no torque, which is the configuration of the JETTO simulation shown in blue on figure 3.28. However the W particle diffusion with no torque cannot be

directly compared with the values of the JETTO simulation, since in the QuaLiKiz standalone all the inputs are fixed, while they evolve in the JETTO simulation.

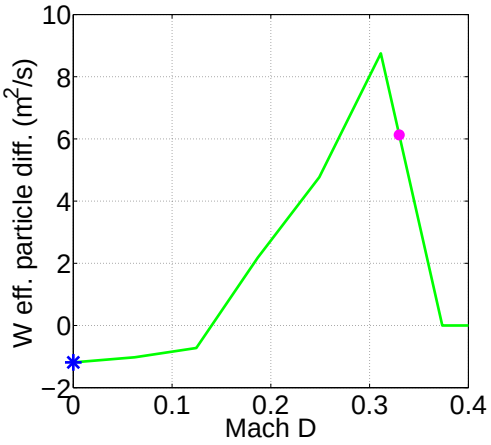

Figure 3.29 – W particle effective diffusion from QuaLiKiz standalone simulation, depending on D Mach number scan. Inputs of QuaLiKiz simulation correspond to the reference JETTO simulation at t=5s7 and ρ=0.7.

On figure 3.29, from Mach=0 to 0.3, the particle diffusion indeed increases with the parallel velocity, which corresponds to what is observed on JETTO simulations on figure 3.28. In particular, the difference on the particle diffusion between the blue star and the magenta circle approaches a factor 5, which is the right order of magnitude compared with the JETTO simulations.

The impact of poloidal asymmetries on W turbulent transport is accounted for in QuaLiKiz based on [8], as described in [37]. The analytical formulation from [8] has been shown to be valid for trace W, and Mach number $M_D << 1$ in the case of ITG dominant, and up to 0.4 in the case of TEM dominant. In the case of interest here, the ITG are the dominant mode, and the main ion Mach number reaches up to 0.5, therefore the analytical formula is valid. The W turbulent diffusion is here increased in presence of rotation. The impact of centrifugal effects on the various components of the turbulent convection (thermodiffusion, rotodiffusion, pure convection) results of a complex compensation of the different components (see [8]). Therefore it is expected to see the W turbulent particle transport (especially the increase of W turbulent diffusion) responding very differently to a modified Mach number, velocity shear and ExB shear velocity compared to the turbulent heat fluxes.

Overall, in absence of rotation, both turbulent and neoclassical W transport are reduced. As a consequence, W is no longer flushed out from the central zone of the plasma in the first confinement time. During the rest of the simulation, it is weakly transported to the center by residual neoclassical convection, but the W amount transported is negligible compared with the case with rotation (see figure 3.26c).

Now that the W transport is understood, we shall focus on the main ion

and electron heat transport in the JETTO simulations. Figure 3.30 shows the heat fluxes profiles from JETTO simulations (reference and without rotation) at t=5.7s, and the electron and ion heat diffusivities depending on D Mach number from the QuaLiKiz standalone simulation. Again on the QuaLiKiz standalone figures, the blue star corresponds to the heat coefficient value with no torque, and the magenta circle corresponds to the D Mach number of the reference JETTO simulation, at t=5.7s at ρ=0.7. Note that the heat diffusivities values are not exactly the same between QuaLiKiz and JETTO for the reference JETTO simulation, because JETTO is an iterative process while in QuaLiKiz standalone the gradients are fixed.

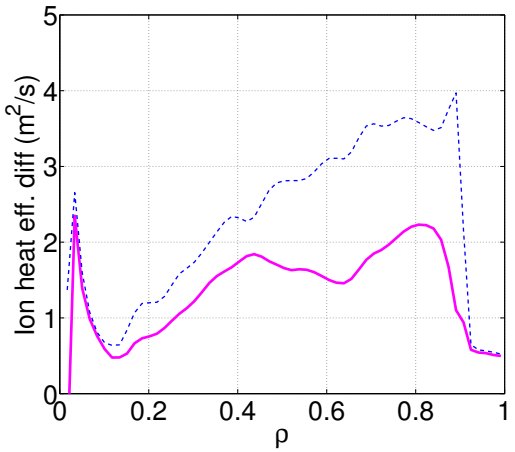

(a) JETTO ion heat effective diffusivity profile at t=5.7s

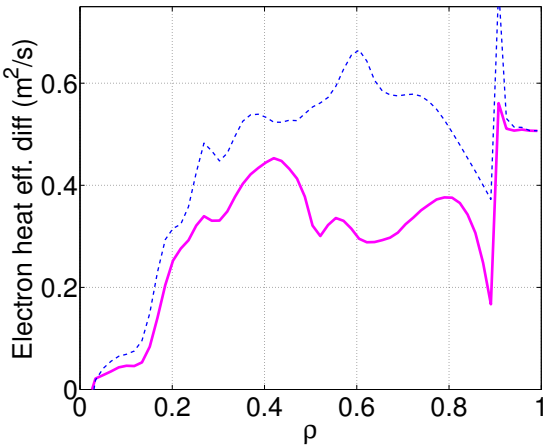

(b) JETTO electron heat effective diffusivity profile at t=5.7s

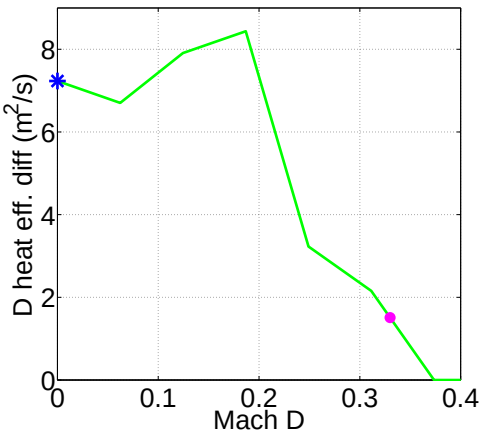

(c) QuaLiKiz standalone ion heat effective diffusivity

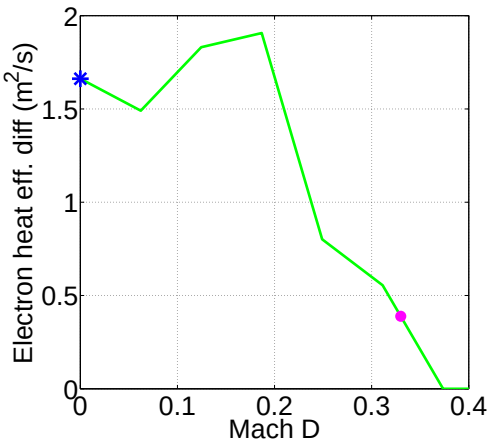

(d) QuaLiKiz standalone electron heat effective diffusivity

Figure 3.30 – Ion and electron heat effective diffusivities profiles from JETTO simulations at t=5.7s : reference (magenta) and without rotation (blue). Ion and electron heat effective diffusivities from QuaLiKiz standalone depending on D Mach number (green). All inputs of QuaLiKiz simulation correspond to the reference JETTO simulation at t=5s7 and ρ=0.7.

The heat fluxes behave as expected both for JETTO and QuaLiKiz standalone simulations. The rotation stabilizes the turbulence through the ExB shear [66]. As a consequence, the more the rotation increases, the more the heat coefficients are reduced. Therefore, toroidal rotation has a positive impact on the plasma confinement.

The comparison of QuaLiKiz standalone simulations with JETTO shows that W turbulent transport behaves in the opposite direction compared with ion and

electron heat transport.

Now the transport coefficients were studied and validated, we shall focus on the density and temperature profiles at t=5.7s, at the end of the first confinement time. We shall study the impact of the modification of the transport caused by the disappearance of the rotation.

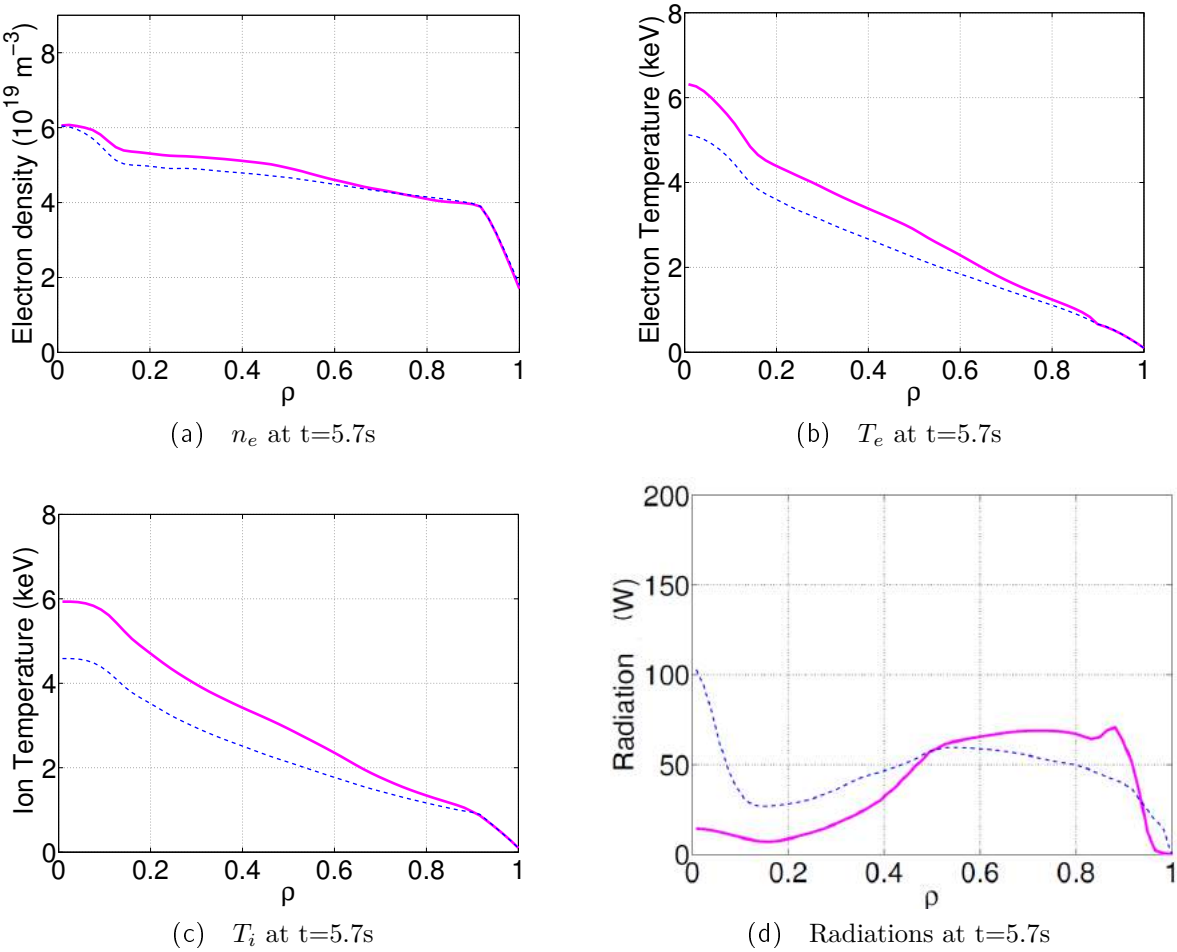

(a) n_e at t=5.7s

(b) T_e at t=5.7s

(c) T_i at t=5.7s

(d) Radiations at t=5.7s

Figure 3.31 – Density, temperatures and radiation profiles at t=5.7s. Reference simulation (magenta), no toroidal rotation (blue)

In absence of rotation, the electron and ion heat turbulent transport is increased. As a consequence, the electron and ion temperatures decrease, as seen on figures 3.31b and 3.31c. Note that the electron density profile on figure 3.31a is weakly impacted, except for the central density peaking which is slightly stiffer in absence of rotation. The central radiation on figure 3.31d is larger in absence of rotation since the W is not flushed out.

In summary, the removal of the toroidal rotation completely changes the W neoclassical transport, as expected, but also its turbulent transport (see figure 3.28). The study of the first confinement time allowed us to identify the toroidal

rotation as destabilizing for the W turbulence (see figure 3.29), but stabilizing for the main ion and the electrons (see figures 3.30c and 3.30d). Initially, the removal of the rotation is deleterious for both the energy confinement (increased turbulence for main ion and electrons) and the central W content since W is no longer flushed out. But once the impact of the first confinement time removed, it appears that toroidal rotation has a negative impact on the W central accumulation (see figure 3.26c).

Overall, the impact of the central particle fueling was clearly identified as an actuator of the W accumulation process. Its removal makes the accumulation disappear. The suppression of the toroidal rotation reduces both neoclassical and turbulent W transport. Therefore the W is still carried to the center of the plasma, however at a reduced rate than in presence of rotation.

3.6 Non-linearities : W stabilization impact

The time evolution of the simulation evolving self-consistently particle, heat, momentum for electrons, ions and impurities (W and Be) involves numerous non-linearities. One of these features is the fact that W seems to have a stabilization impact on turbulence. In order to study the mechanisms at play, a simulation with no W is set. In this simulation the Z_{eff} is still 1.34 as in the reference simulation, except the Be is considered the only impurity with concentrations up to 10^{18}. Figure 3.32 shows the ion and electron heat effective diffusions and the ion particle effective diffusion profiles at t=6.5s. The reference simulation with Be and W is in magenta and the simulation with Be only is in blue.

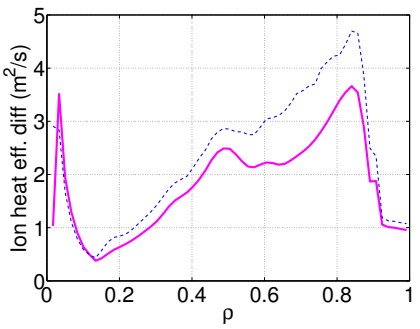

(a) Ion heat effective diffusion

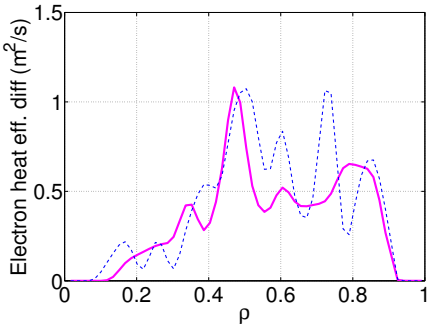

(b) Electron heat effective diffusion

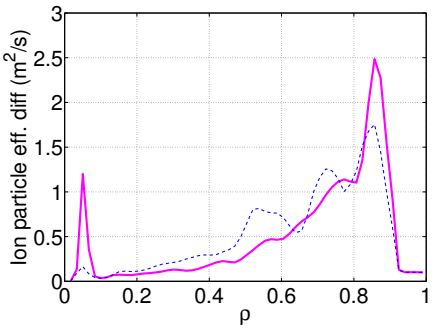

(c) Ion particle effective diffusion

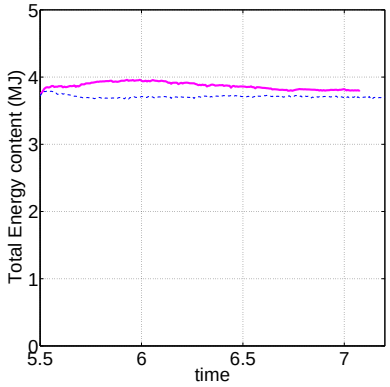

(d) Simulation without radiation

Figure 3.32 – Ion and electron heat effective diffusion and ion particle effective diffusion profiles at t=6.5s, and timetrace of the total energy content Reference simulation with W and Be (magenta) and simulation with Be only (blue)

Overtime, the energy content on figure 3.32d is lower in absence of W by a maximum of 7%. The ion heat diffusion is higher up to 40% in absence of W on figure 3.32a. The impact is less pronounced on the electron heat diffusion but still visible. As for the particle diffusion, in absence of W the diffusion is higher from $\rho = 0.2 - 0.8$. Overall W seems to cause a reduction of the heat and particle transport. The presence of W impacts two main parameters : the main ion dilution and the radiation level. To disentangle these two mechanisms, two simulations are discussed in the next sections, one for each parameter.

3.6.1 Possible cause : radiation

One explanation could be that the radiation caused by W impacts the electron and ion temperature enough to reduce the turbulence. To validate this assumption, a simulation was run with W and Be but with radiation set to zero. The ion and electron heat effective diffusions and the ion particle effective diffusion are shown at t=6.5s on figure 3.33. The reference simulation with W and Be is in

magenta, the simulation with Be only is in blue and the simulation with Be and W without radiation is in red.

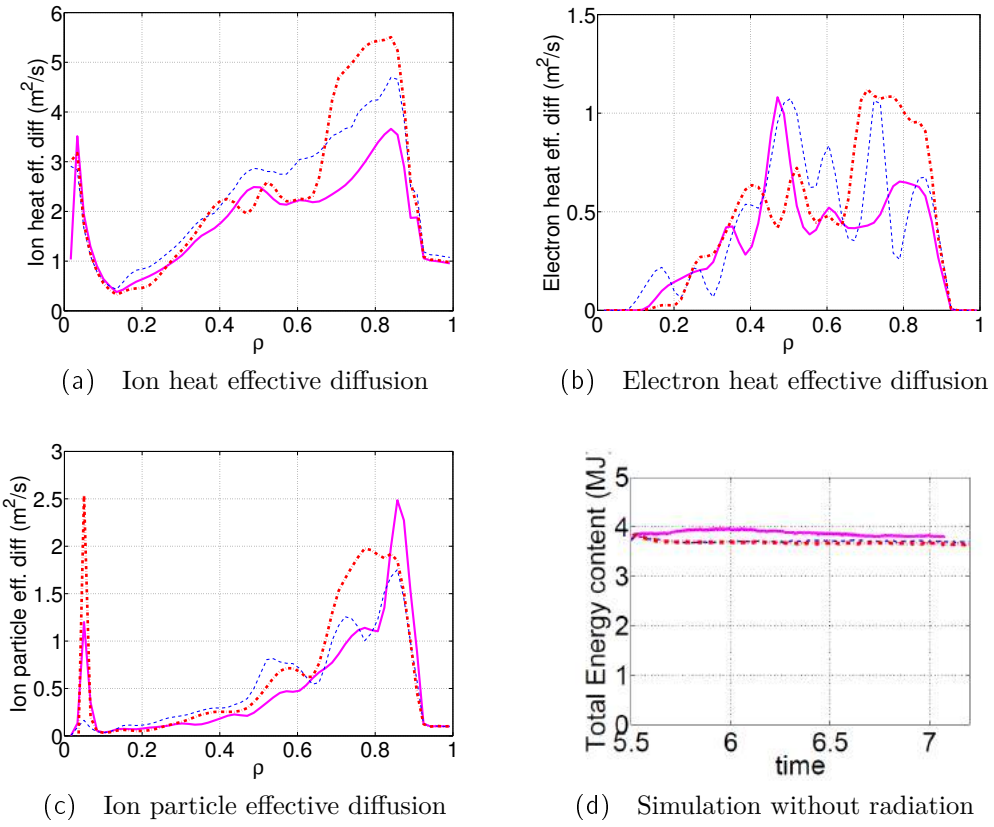

(a) Ion heat effective diffusion

(b) Electron heat effective diffusion

(c) Ion particle effective diffusion

(d) Simulation without radiation

Figure 3.33 – Ion and electron heat effective diffusion and ion particle effective diffusion at t=6.5s, and timetrace of the total energy content. Reference simulation with W and Be (magenta),simulation with Be only (blue) and simulation with Be and W without radiation (red)

On figure 3.33d, the energy content of the Be only and no radiation simulations is similar (1% difference). For the ion and electron heat diffusivities (figures 3.33a and 3.33b), the simulation without radiation behaves similarly. From the axis to $\rho = 0.4$, it follows the simulation with no W (in blue). For $\rho = 0.4 - 0.6$, it comes closer to the reference simulation (Be, W and radiation on) in magenta. Then from $\rho = 0.6$ outward, it comes closer with the simulation with no W. For the ion particle diffusivity on figure 3.33c, the simulation without radiation stays close to the simulation with no W. Overall, the removal of the radiation brings up the heat and particle diffusivities to the level of the simulation with no W.

In order to have a better understanding of the stabilization effect, the timetraces of ion and electron temperatures, the ratio T_e/T_i and the ion heat diffusivity are shown on figure 3.34 for the position ρ=0.7.

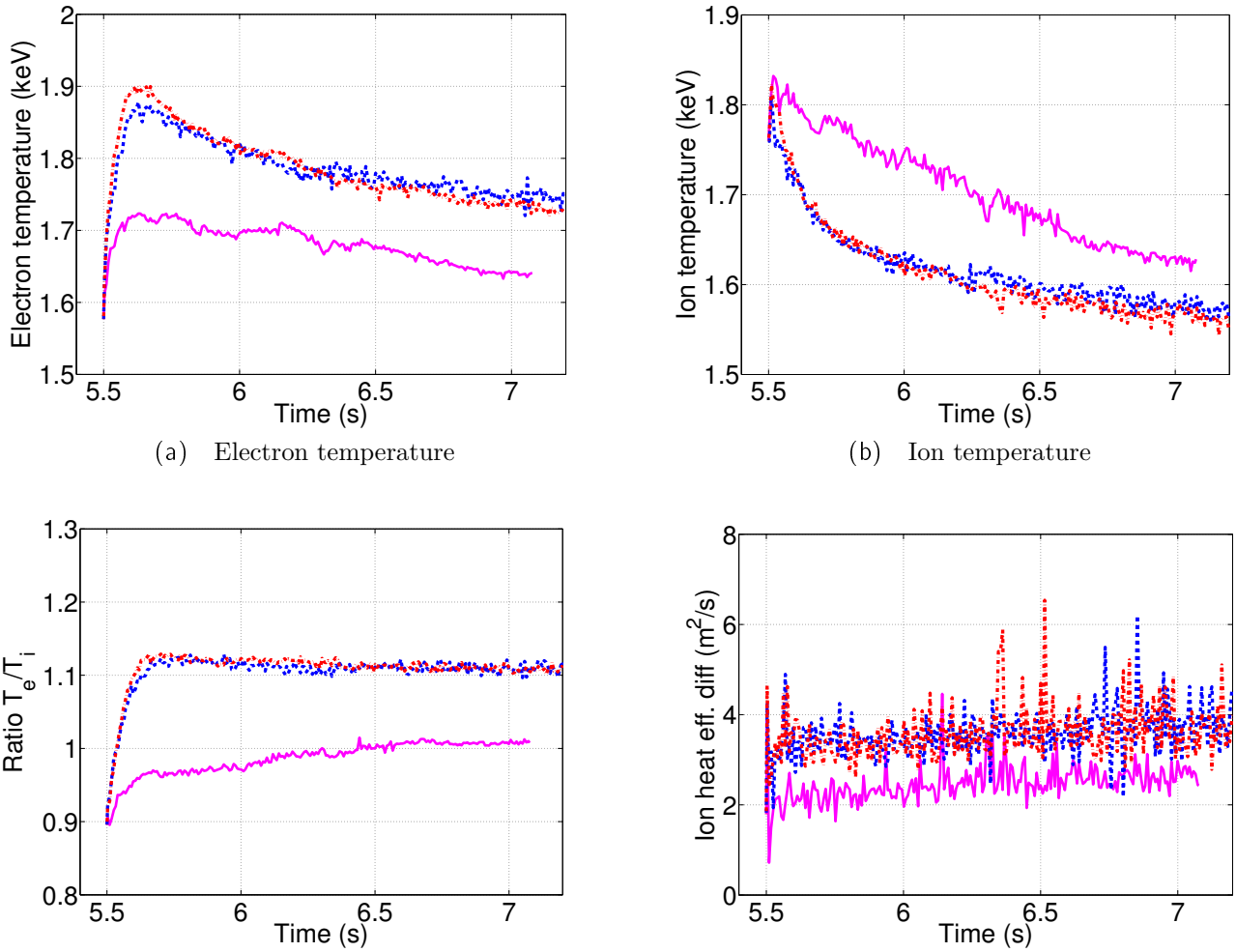

(a) Electron temperature

(b) Ion temperature

(c) Ratio T_e/T_i

(d) Ion heat eff. diff.

Figure 3.34 – Ion and electron temperatures, ratio T_e/T_i and ion heat effective diffusion timetraces at ρ=0.7. Reference simulation with W and Be (magenta), simulation with Be only (blue) and simulation with Be and W without radiation (red)

The temperature, density and rotation profiles at 6.5s are also shown on figure 3.35.

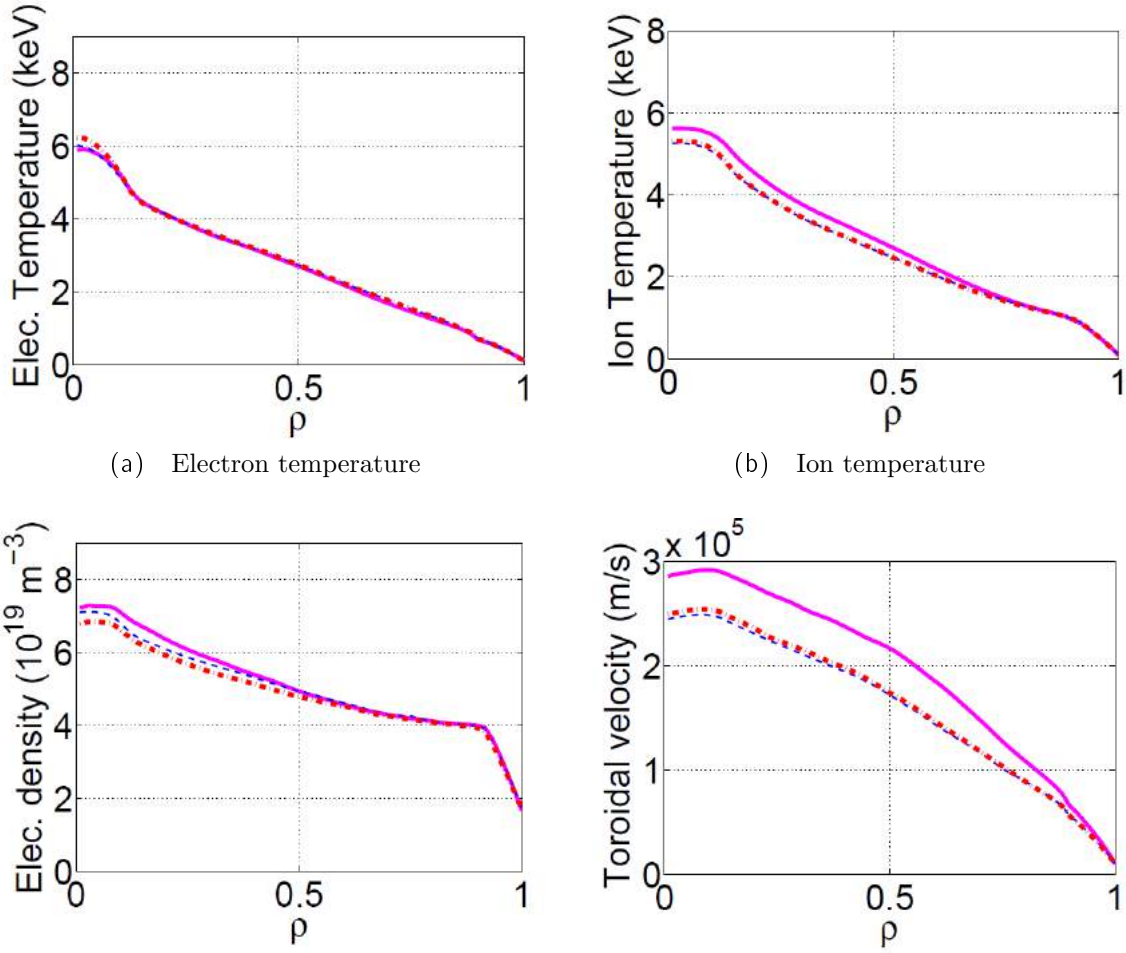

(a) Electron temperature

(b) Ion temperature

(c) Electron density

(d) Toroidal velocity

Figure 3.35 – Profiles of the ion and electron temperatures, electron density and toroidal rotation at t=6.5s. Reference simulation with W and Be (magenta), simulation with Be only (blue) and simulation with Be and W without radiation (red)

On all figures the curves split in two groups : the reference simulation with W and radiation on one side (magenta), and the simulations without radiation (red) and without W (blue) on the other side. The electron temperature on figure 3.34a is higher over time for the simulation without W and radiation. The electron temperature profile at 6.5s on figure 3.35a is very similar for the three simulations. The ion temperature on figure 3.34b is also impacted and is lowered in absence of W or in absence of radiation. On figure 3.35b, the central ion temperature of the simulations without radiation (red) and without W (blue) is decreased by 7%. The modification in the temperature impacts the ratio T_e/T_i shown on figure 3.34c, which is higher for the simulations without W and without radiation. The electron density on figure 3.35c and the toroidal velocity on figure 3.35d are also lower for the simulations without W and without radiation.

The enhanced electron temperature, combined with lower ion temperature leads to enhanced T_e/T_i, which is known to increase turbulence (see [26]). Therefore, the stabilization effect could be explained by this mechanism : the removal of W causes the radiation level to be significantly reduced. This impacts the temperature profiles as seen on figure 3.34 and the ratio T_e/T_i is enhanced, causing the turbulence to be reduced. In order to validate this explanation, a QuaLiKiz standalone simulation is run, scanning the electron temperature. All the other inputs are taken from the JETTO reference simulation parameters from t=6.5s and ρ=0.7. The ion and electron heat effective diffusivities and the ion particle effective diffusion are shown on figure 3.36. The red diamond corresponds to the T_e/T_i ratio at t=5.7S at ρ=0.7 for the simulation without radiation, in red on figure 3.34. The magenta circle corresponds to the T_e/T_i ratio at t=5.7S at ρ=0.7 for the reference simulation. Again, the values are not exactly the same between QuaLiKiz and JETTO for the reference JETTO simulation, because JETTO is an iterative process while in QuaLiKiz standalone the gradients are fixed.

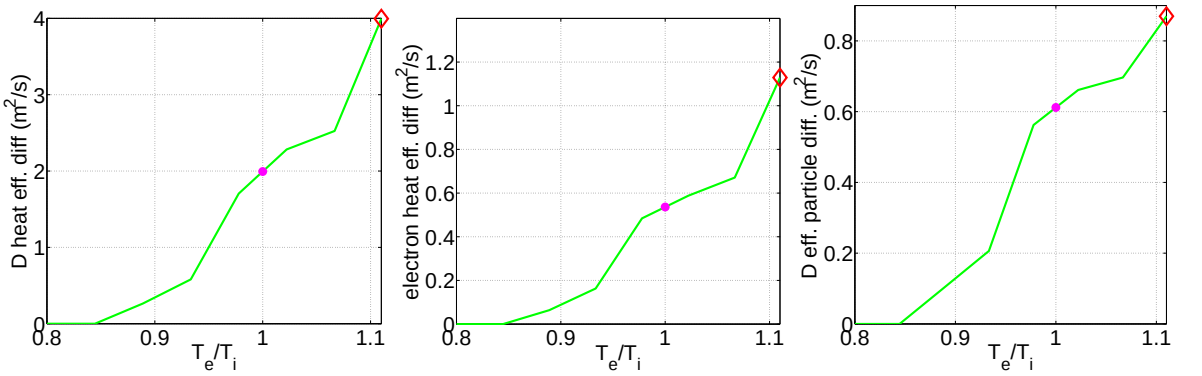

(a) Ion heat effective diffusion (b) Electron heat effective diffusion (c) Ion particle effective diffusion

Figure 3.36 – QuaLiKiz standalone : ion and electron heat effective diffusion and ion particle effective diffusion at t=6.5s.

On figure 3.36a and 3.36b, ion and electron heat effective diffusivities both increase with the ratio T_e/T_i, as expected. It is coherent with the JETTO simulation from figure 3.34 : without radiation, the T_e/T_i ratio is bigger therefore the turbulence increases. Note that the slope of the increase of heat coefficients is quite stiff. As a consequence, a small modification of the T_e/T_i ratio impacts significantly the turbulence. In this case, the removal of the radiation (i.e. the variation of heat diffusion between the red diamond and the magenta circle) caused an increase of 2.0 m^2/s for the ion heat diffusion, 0.54 m^2/s for the electron heat coefficient and 0.61 m^2/s for the ion particle diffusion coefficient.

The removal of the radiation impacts the temperature and has a destabilizing effect. This indicates that a large portion of the stabilization phenomenon occurs through the radiation. The next section focuses on the other mechanism susceptible to has a stabilizing effect : the effect of dilution.

3.6.2 Other possible cause : dilution

The other mechanism that could participate to the stabilization effect of W, is dilution. Indeed, even if W is a trace impurity, it undergoes poloidal asymmetries and therefore could locally no longer be a trace. Figure 3.37 shows the 2D poloidal cut of the W contribution to the Z_{eff} at t=6.5s as an illustration. The W contribution to Z_{eff} remains similar at all times of the simulation.

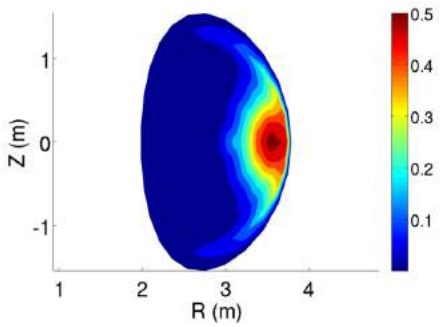

Figure 3.37 – W contribution to the Zeff $\Delta Z_{eff} = Z^2 n_W / n_e$ at t=6.5s

On the LFS the poloidal asymmetries cause the W to contribute to Z_{eff} up to 0.5. In those zones, the W is no longer a trace species and can contribute to the main ion dilution as well as modify the collisionality. It is established that increased Z_{eff} has a stabilizing impact through dilution [42, 126, 21, 26].

To estimate the impact of such a W contribution to Z_{eff}, QuaLiKiz standalone is run. Figure 3.38 illustrates QuaLiKiz ion and electron heat coefficients, as well as the ion particle diffusion. The blue star corresponds to the zero W concentration for the simulation with Be only, in blue on figures 3.33. The magenta circle corresponds to the W concentration at t=6.5s at ρ=0.7 for the reference simulation.

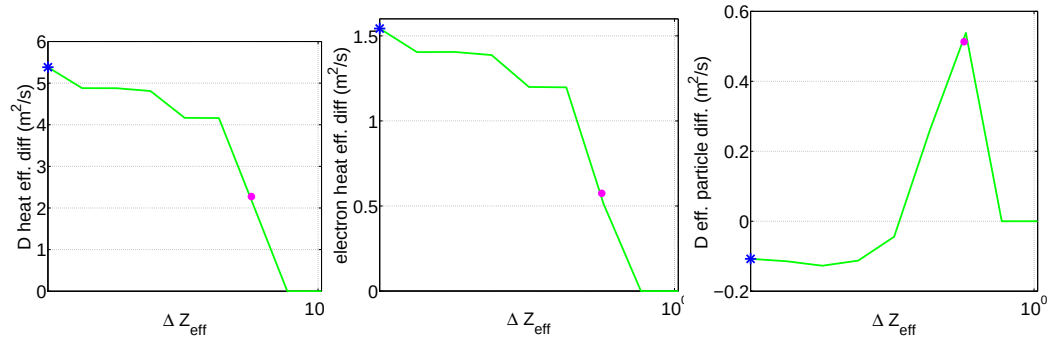

(a) Ion heat effective diffusion (b) Electron heat effective diffusion (c) Ion particle effective diffusion

Figure 3.38 – QuaLiKiz standalone : ion and electron heat effective diffusion and ion particle effective diffusion at t=6.5s.

On figure 3.38a and 3.38b, ion and electron heat effective diffusivities remain unchanged until $\Delta Z_{eff} = 2.10^4$. Then they decrease and reaches stable modes for $\Delta Z_{eff} = 3.10^{-1}$. On figure 3.38c, the main ion particle diffusion follows a completely different trend. This can be explained by the fact that QuaLiKiz ensures quasi neutrality, therefore the D content varies accordingly to the W content. Therefore the D density and density gradients are modified. The values of transport coefficients between the case without W and the W concentration from reference JETTO simulation (ie the difference between the blue star and the magenta circle) are of 3.1 m^2/s for the ion heat diffusion, 0.97 m^2/s for the electron heat coefficient and 0.62 m^2/s for the ion particle diffusion coefficient. Therefore the contribution of the dilution to the stabilization effect is 30% bigger compared with the contribution through the radiation seen on figures 3.36.

Overall, the W has a stabilizing effect on the turbulence. The effect mainly occurs through radiation and the modification of temperature profiles, but also through main ion dilution and increase of collisionality.

3.7 Conclusion of the chapter

Overall, for the first time, a simulation over multiple confinement times, flux driven, multi-channel (temperature, density and rotation profiles), including Be and W, accounting for poloidal asymmetries is performed. Within the integrated modeling environment JETTO, first-principles codes such as QuaLiKiz and NEO model respectively turbulent and neoclassical transport, up to the pedestal top. An empirical model is tuned to reproduce experimental measurements in the pedestal. The NBI particle, heat and sources are self-consistently modeled using PENCIL, while SANCO evolves radiation levels.

The simulation successfully reproduces the time evolution over 1.5s (hence 5 confinement times) of the temperature, density and rotation profiles. The predicted electron density, electron and ion temperature and rotation profiles lie within experimental uncertainties at all times. Moreover, the W central accumulation is correctly reproduced with the simulation of turbulent and neoclassical transport, but with no accounting of sawteeth and ELMs.

Actuators of the W accumulation are studied : central particle fuelling and torque inputs through NBI. It appears that removing the central particle source cancels the central W accumulation, and cutting by half the central particle fuelling reduces also by half the W central accumulation. This is encouraging for devices such as WEST or ITER, which do not use NBI central particle fuelling. The suppression of the torque reduces the neoclassical W transport as expected, but also reduces the W turbulent transport. It means that in this case, the toroidal rotation has a stabilizing impact on the main ion and electron turbulence, and a destabilizing impact on the W transport. Therefore the W is still carried to the center of the plasma, however slower than in presence of torque.

Finally, the stabilization effect of the W is studied and its causes are investigated. Indeed, removing W from the integrated modeling simulation led to a

significant reduction of the main ion heat diffusivity. Two mechanisms that could explain this stabilization effect are studied : through radiation and through dilution. First, radiation causes electron temperature to decrease and ion temperature to increase, leading to reduced T_e/T_i which is stabilizing. This mechanism represents most of the stabilization effect. This is encouraging because it means that W radiation has a positive impact on the plasma confinement, even if this small advantage does not fully compensate the catastrophic consequences of W accumulation. Locally, because of W poloidal asymmetries in a rotating plasma, the W contribution to Z_{eff} at the outboard mid-plane can go up to 0.5. This locally impacts turbulent transport through dilution and modified collisionality, which both have a stabilizing impact on turbulent transport.

4Conclusions and perspectives

The global energy demand is likely to further increase with time, therefore finding a sustainable, clean and safe energy source becomes an urgent problem. Thermonuclear fusion can meet all these requirements and be a source of massive centralized electricity. In particular, magnetic confinement fusion is currently the most advanced technology for this challenge, as ITER will be the first fusion device to produce more fusion energy than what it consumes. Among the many challenges faced by fusion research, the W pollution and central accumulation is a key issue. Indeed, current design entails W tiles for the most exposed plasma facing component. W has many advantages, such as low erosion rate, high melting point so high heat tolerance, and low tritium retention. But since W is a heavy impurity it causes strong line radiation so W contamination must be lowered as much as possible. Further degradation related to W central density peaking, called accumulation, must be avoided. W central accumulation is currently a key issue which limits the performances of fusion plasmas. In order to control W behavior, the first step is to understand the mechanisms leading to the W accumulation, and identify the actuators responsible for it. Since W transport interplays with many plasma parameters, the only way to understand the story of W behavior, is account simultaneously for radiation, heat particle and momentum source, turbulent and collisional transport. This is made possible thanks to integrated modeling platforms.

W behavior is impacted by many plasma parameters in complex non-linear interplays. Therefore modeling self-consistently W transport requires the use of first-principle based codes, which leads to a non-negligible computational cost. Especially, the W poloidal assymmetric distribution makes the use of a neoclassical code mandatory (NEO [15, 17]). In order to determine if it was feasible to combine geometric analytical terms from [9] describing the effect of poloidal asymmetries on W flux, with a simpler and faster neoclassical code, NCLASS [74], in order to produce results similar to the ones obtained with NEO at reduced CPU costs. At first, the analytical formula by Angioni-Helander [9] was tested outside of its range of applicability, for realistic tokamak parameters. Provided an empirically adjusted parameter for a better matching of NEO results, the analytical formula proved to be reliable enough, even out of its strict range of applicability. However, for very strong poloidal asymmetries, the analytical formula overestimates (up to 50%) NEO results, which makes it inadequate. The analytical formula was then combined in NCLASS and implemented in the integrated modeling environment JETTO. All the profiles are fits from experimental data, only the W profile is evolved, assuming a purely neoclassical transport. In one case based on JET baseline scenario parameters, for only one time slice, this fast model can predict a very similar 2D W density map as NEO while saving a factor of a thousand in computer time. In a second JET hybrid scenario case, for a simulation of 1.5s of plasma, the central tungsten peaking was overestimated

due to a sensitive balance between temperature screening and inward impurity convection near the magnetic axis. The model in its present formulation therefore cannot be considered to have general applicability, but could be used for scoping studies before running the full NEO model. The parametric dependencies of the temperature screening reduction due to poloidal asymmetrics still remains to be better characterised and explained by neoclassical theory. Therefore for our integrated modeling simulations, NEO is used.

For the first time, a simulation over multiple confinement times, flux driven, multi-channel (temperature, density and rotation profiles), including D, Be and W, accounting for poloidal asymmetries is performed. Within JETTO [33, 115], first-principles codes such as QuaLiKiz [22, 20, 37] and NEO model respectively turbulent and neoclassical transport, up to the pedestal top. An empirical model is tuned to reproduce experimental measurements in the pedestal. The NBI particle, heat and sources are self-consistently modeled using PENCIL [34], while SANCO [4] evolves radiation levels. The simulation successfully reproduces the time evolution over 1.5s (hence 5 confinement times) of the temperature, density and rotation profiles. The predicted electron density, electron and ion temperature and rotation profiles globally lie within experimental uncertainties, except during sawtooth crashed which are not modeled. Moreover, the W central accumulation time scale is correctly reproduced with the simulation of turbulent and neoclassical transport, but without accounting of sawteeth and ELMs and assuming a constant W flux at the LCFS. Actuators of the W accumulation are studied : central particle fuelling and torque inputs through NBI. It appears that removing the central particle source cancels the central W accumulation, and cutting by half the central particle fuelling reduces also by half the W central accumulation. This is encouraging for devices such as WEST or ITER, which do not use NBI central particle fuelling. The suppression of the torque reduces the neoclassical W transport as expected, but also reduces the W turbulent transport. It means that in this case, the toroidal rotation has a stabilizing impact on the main ion and electron turbulence, and a destabilizing impact on the W transport. Therefore the W is still carried to the center of the plasma, however slower than in presence of torque. Finally, the stabilization effect of the W is studied and its causes are investigated. Indeed, removing W from the integrated modeling simulation led to a significant reduction of the main ion heat diffusivity. Two mechanisms that could explain this stabilization effect are studied : through radiation and through dilution. The presence of radiation impact both electron and ion temperature, leading to reduced T_e/T_i, which is stabilizing. This is encouraging because it means that W radiation has a positive impact on the plasma confinement, even if this small advantage does not fully compensate the catastrophic consequences of W accumulation. Locally, because of W poloidal asymmetries in a rotating plasma, the W contribution to Z_{eff} at the outboard mid-plane can go up to 0.5. This locally impacts turbulent transport through dilution and modified collisionality, which both have a stabilizing impact on turbulent transport.

Now the integrated modeling tool works and its results are proofed against

experiment, many applications are possible. Before increasing the complexity of the simulation and coupling new codes, a first step would be to keep the same settings and try to reproduce another NBI-only JET-ILW pulse, in presence of W. This would allow to test the robustness of the numerical settings, especially for the ETB and the W source. The actual simulation could also be completed by a simple model for sawteeth, which would not increase too much the computational cost. This would answer the interrogation on the sawteeth impact on the profiles, for reproducing more accurately the W central accumulation. An ELM model could also be added [85], to model the pedestal and the W source more accurately. Finally, the SOL codes available in JINTRAC could be added in order to have a simulation accounting for all aspects of the plasma and study the impact of the W source on the central accumulation. It would also be very interesting to understand the mechanisms leading the RF heating to limit central accumulation. To do so, the study of a RF-only pulse could be a start, to isolate the interesting mechanisms. Then another pulse with NBI first and then RF heating could be modeled, to see if the mechanisms from the RF-only are reproduced and how they are modified by the presence of NBI heating. This aspect of W behavior is currently under investigation [29]. Finally, predictions for JET D-T campain, WEST or even ITER are now possible, the main doubt being the pedestal prediction. Also, in order to lighten the computational cost of first-principle codes in integrated modeling while keeping the physics accuracy, faster tools such as Neural Networks are currently developed for QuaLiKiz [36].

Bibliographie

[1] Tim ABRAM et Sue ION. « Generation-IV nuclear power : A review of the state of the science ». In : *Energy Policy* 36.12 (2008). Foresight Sustainable Energy Management and the Built Environment Project, p. 4323 – 4330. ISSN : 0301-4215. DOI : https://doi.org/10.1016/j.enpol.2008.09.059. URL : http://www.sciencedirect.com/science/article/pii/S0301421508004448 (cf. p. 10).

[2] U.S. Energy Information ADMINISTRATION. « International Energy Outlook ». In : (2017). URL : www.eia.gov/ieo (cf. p. 9).

[3] U.S. Energy Information ADMINISTRATION. « Key world energy statistics ». In : (2017). URL : http://www.iea.org/statistics (cf. p. 9).

[4] L. Lauro-Taroni et AL. 1994 (cf. p. 26, 65, 75, 79, 117).

[5] Pereverzev G.V. et AL. 1991 (cf. p. 27).

[6] C. ANGIONI, L. CARRARO, T. DANNERT, N. DUBUIT et al. « Particle and impurity transport in the Axial Symmetric Divertor Experiment Upgrade and the Joint European Torus, experimental observations and theoretical understanding ». In : *Physics of Plasmas* 14.5 (2007), p. 1–9. ISSN : 1070664X. DOI : 10.1063/1.2515300 (cf. p. 52).

[7] C. ANGIONI, F. J. CASSON, P. MANTICA, T. PÜTTERICH et al. « The impact of poloidal asymmetries on tungsten transport in the core of JET H-mode plasmas ». In : *Physics of Plasmas* 22.5 (2015). ISSN : 10897674. DOI : 10.1063/1.4919036 (cf. p. 53, 54, 56, 72).

[8] C ANGIONI, FJ CASSON, C VETH et AG PEETERS. « Analytic formulae for centrifugal effects on turbulent transport of trace impurities in tokamak plasmas ». In : *Physics of Plasmas* 19.12 (2012), p. 122311 (cf. p. 103).

[9] C ANGIONI et P HELANDER. « Neoclassical transport of heavy impurities with poloidally asymmetric density distribution in tokamaks ». In : *Plasma Physics and Controlled Fusion* 56.12 (2014), p. 124001–124008. ISSN : 0741-3335. DOI : 10.1088/0741-3335/56/12/124001. URL : http://stacks.iop.org/0741-3335/56/i=12/a=124001?key=crossref.0d855241b9a64a207201a2f3562a65b9$\backslash$npapers3://publication/doi/10.1088/0741-3335/56/12/124001 (cf. p. 21, 29, 52, 53, 60, 61, 72, 116).

[10] C ANGIONI, P MANTICA, T PÜTTERICH, M VALISA et al. « Tungsten transport in JET H-mode plasmas in hybrid scenario, experimental observations and modelling ». In : *Nuclear Fusion* 54.8 (2014), p. 83028. DOI : 10.1088/0029-5515/54/8/083028. URL : http://stacks.iop.org/0029-5515/54/i=8/a=083028 (cf. p. 23, 24, 27, 52, 54, 56, 61, 67, 72, 74, 75, 78).

[11] C ANGIONI, M SERTOLI, R BILATO, V BOBKOV et al. « A comparison of the impact of central ECRH and central ICRH on the tungsten behaviour in ASDEX Upgrade H-mode plasmas ». In : *Nucl. Fusion* 57.056015 (2017) (cf. p. 24).

[12] J.F. ARTAUD, V. BASIUK, F. IMBEAUX, M. SCHNEIDER et al. « The CRONOS suite of codes for integrated tokamak modelling ». In : *Nuclear Fusion* 50.4 (2010), p. 043001. ISSN : 0029-5515. DOI : 10.1088/0029-5515/50/4/043001. URL : http://stacks.iop.org/0029-5515/50/i=4/a=043001?key=crossref.789a86752c1e600c667a9bacdac4c6e9 (cf. p. 27).

[13] World Nuclear ASSOCIATION. « Supply of Uranium ». In : (2016). URL : http://www.world-nuclear.org/information-library/nuclear-fuel-cycle/uranium-resources/supply-of-uranium.aspx (cf. p. 10).

[14] B BAIOCCHI, J GARCIA, M BEURSKENS, C BOURDELLE et al. « Turbulent transport analysis of JET H-mode and hybrid plasmas using QuaLiKiz and Trapped Gyro Landau Fluid ». In : *Plasma Physics and Controlled Fusion* 57.3 (2015), p. 035003 (cf. p. 27).

[15] E A BELLI et J CANDY. « Drift-Kinetic Simulations of Neoclassical Transport APS-DPP Meeting Motivation for the NEO code ». In : (2008) (cf. p. 21, 29, 74, 75, 79, 82, 116).

[16] E A BELLI et J CANDY. « Kinetic calculation of neoclassical transport including self-consistent electron and impurity dynamics ». In : *Plasma Phys. Control. Fusion* 50.9 (2008), p. 95010. ISSN : 0741-3335. DOI : 10.1088/0741-3335/50/9/095010. URL : http://stacks.iop.org/0741-3335/50/i=9/a=095010 (cf. p. 52).

[17] E A BELLI et J CANDY. « Full linearized Fokker–Planck collisions in neoclassical transport simulations ». In : *Plasma Phys. Control. Fusion* 54.54 (2012), p. 15015–17. ISSN : 0741-3335. DOI : 10.1088/0741-3335/54/1/015015. URL : http://iopscience.iop.org/0741-3335/54/1/015015 (cf. p. 21, 29, 43, 52, 74, 75, 79, 82, 116).

[18] E A BELLI, J CANDY et C ANGIONI. « Pfirsch-Schluter neoclassical heavy impurity transport in a rotating plasma ». In : *Plasma Physics and Controlled Fusion* 56.12 (2014), p. 124002. ISSN : 13616587. DOI : 10.1088/0741-3335/56/12/124002. URL : http://iopscience.iop.org/0741-3335/56/12/124002/article/$\backslash$npapers3://publication/doi/10.1088/0741-3335/56/12/124002 (cf. p. 53).

[19] R. BILATO, O. MAJ et C. ANGIONI. « Modelling the influence of temperature anisotropies on poloidal asymmetries of density in the core of rotating plasmas ». In : *Nuclear Fusion* 54.7 (2014), p. 072003. ISSN : 0029-5515. DOI : 10.1088/0029-5515/54/7/072003. URL : http://iopscience.iop.org/0029-5515/54/7/072003/article/ (cf. p. 24, 52, 72).

[20] C BOURDELLE, J CITRIN, B BAIOCCHI, A CASATI et al. « Core turbulent transport in tokamak plasmas : bridging theory and experiment with QuaLiKiz ». In : *Plasma Physics and Controlled Fusion* 58.1 (2015), p. 014036 (cf. p. 20, 74, 83, 117).

[21] C BOURDELLE, X GARBET, GT HOANG, J ONGENA et RV BUDNY. « Stability analysis of improved confinement discharges : internal transport barriers in Tore Supra and radiative improved mode in TEXTOR ». In : *Nuclear Fusion* 42.7 (2002), p. 892 (cf. p. 113).

[22] C BOURDELLE, X GARBET, F IMBEAUX, A CASATI et al. « A new gyrokinetic quasilinear transport model applied to particle transport in tokamak plasmas ». In : *Physics of Plasmas* 14.11 (2007), p. 112501 (cf. p. 20, 52, 74, 83, 117).

[23] BP. « BP Statistical Review of World Energy ». In : (2017). URL : https://www.bp.com/en/global/corporate/energy-economics/statistical-review-of-world-energy.html (cf. p. 10).

[24] S BREZINSEK, T LOARER, V PHILIPPS, HG ESSER et al. « Fuel retention studies with the ITER-like wall in JET ». In : *Nuclear Fusion* 53.8 (2013), p. 083023 (cf. p. 22).

[25] J CANDY et RE WALTZ. « An eulerian gyrokinetic-maxwell solver ». In : *Journal of Computational Physics* 186.2 (2003), p. 545–581 (cf. p. 20).

[26] A CASATI, C BOURDELLE, X GARBET, F IMBEAUX et al. « Validating a quasi-linear transport model versus nonlinear simulations ». In : *Nuclear Fusion* 49.8 (2009), p. 085012 (cf. p. 112, 113).

[27] Alessandro CASATI. « A quasi-linear gyrokinetic transport model for tokamak plasmas ». In : *arXiv preprint arXiv :1204.3254* (2012) (cf. p. 19).

[28] F. J. CASSON, C. ANGIONI, E. A. BELLI, R. BILATO et al. « Theoretical description of heavy impurity transport and its application to the modelling of tungsten in JET and ASDEX Upgrade ». In : *Plasma Physics and Controlled Fusion* 014031 (2015), p. 1–9. ISSN : 0741-3335. DOI : 10.1088/0741-3335/57/1/014031. arXiv : 1407.1191. URL : http://arxiv.org/abs/1407.1191$\backslash$nhttp://dx.doi.org/10.1088/0741-3335/57/1/014031 (cf. p. 23, 24, 27, 52, 57–59, 72).

[29] F. J. CASSON, H. PATTEN, O. FICKER, J. CITRIN et al. *Fully predictive simulations of hybrid scenario evolution to optimise ICRH against impurity accumulation* (cf. p. 118).

[30] F.J. CASSON, R.M. MCDERMOTT, C. ANGIONI, Y. CAMENEN et al. « Validation of gyrokinetic modelling of light impurity transport including rotation in ASDEX Upgrade ». In : *Nuclear Fusion* 53.6 (2013), p. 063026. ISSN : 0029-5515. DOI : 10.1088/0029-5515/53/6/063026. arXiv : 1211.7312. URL : http://stacks.iop.org/0029-5515/53/i=6/a=063026?key=crossref.b270807a6b6c4210adcc3fe8bf574ecf (cf. p. 26).

[31] CEA. *Magnetic confinement*. 2016. URL : http://www-fusion-magnetique.cea.fr/gb/fusion/physique/modesconfinement.htm (cf. p. 17).

[32] CEA. *Magnetic fusion : the main principles*. 2016. URL : http://www-fusion-magnetique.cea.fr/fusion/principes/principes01.htm (cf. p. 13).

[33] G CENACCHI et A TARONI. *JET Internal Report*. 1988 (cf. p. 26, 79, 117).

[34] CD CHALLIS, JG CORDEY, H HAMNEN, PM STUBBERFIELD et al. « Non-inductively driven currents in JET ». In : *Nuclear Fusion* 29.4 (1989), p. 563 (cf. p. 79, 84, 117).

[35] W CHOE, C S CHANG et M ONO. « Temperature anisotropy in a cyclotron resonance heated tokamak plasma and the generation of poloidal electric field ». In : *Physics of Plasmas* 2 (1995), p. 2044–2054. ISSN : 1070664X. DOI : 10.1063/1.871456 (cf. p. 72).

[36] J CITRIN, S BRETON, F FELICI, F IMBEAUX et al. « Real-time capable first principle based modelling of tokamak turbulent transport ». In : *Nuclear Fusion* 55.9 (2015), p. 92001. ISSN : 0029-5515. DOI : 10.1088/0029-5515/55/9/092001. arXiv : 1502.07402v1. URL : http://stacks.iop.org/0029-5515/55/i=9/a=092001 (cf. p. 118).

[37] Jonathan CITRIN, Clarisse BOURDELLE, Francis J CASSON, Clemente ANGIONI et al. « Tractable flux-driven temperature, density, and rotation profile evolution with the quasilinear gyrokinetic transport model QuaLiKiz ». In : *Plasma Physics and Controlled Fusion* (2017) (cf. p. 20, 27, 73, 74, 79, 83, 90, 91, 103, 117).

[38] Daniel CLERY. *A Piece of the sun : the quest for fusion energy*. The Overlook Press, 2014 (cf. p. 11).

[39] David P COSTER, Vincent BASIUK, Grigori PEREVERZEV, Denis KALUPIN et al. « The european transport solver ». In : *IEEE Transactions on Plasma Science* 38.9 (2010), p. 2085–2092 (cf. p. 27).

[40] Pierre COTTIER. « Modelling the turbulent transport of angular momentum in tokamak plasmas-A quasi-linear gyrokinetic approach ». Thèse de doct. Ecole Polytechnique X, 2013 (cf. p. 15, 25, 26).

[41] Andris M DIMITS, G BATEMAN, MA BEER, BI COHEN et al. « Comparisons and physics basis of tokamak transport models and turbulence simulations ». In : *Physics of Plasmas* 7.3 (2000), p. 969–983 (cf. p. 19).

[42] RR DOMINGUEZ et MN ROSENBLUTH. « Local kinetic stability analysis of the ion temperature gradient mode ». In : *Nuclear fusion* 29.5 (1989), p. 844 (cf. p. 113).

[43] R DUX, V BOBKOV, A HERRMANN, A JANZER et al. « Plasma-wall interaction and plasma behaviour in the non-boronised all tungsten ASDEX Upgrade ». In : *Journal of Nuclear Materials* 390 (2009), p. 858–863 (cf. p. 24).

[44] R DUX, A JANZER, T PÜTTERICH et ASDEX Upgrade TEAM. « Main chamber sources and edge transport of tungsten in H-mode plasmas at ASDEX Upgrade ». In : *Nuclear Fusion* 51.5 (2011), p. 053002 (cf. p. 24).

[45] M ERBA, A CHERUBINI, VV PARAIL, E SPRINGMANN et A TARONI. « Development of a non-local model for tokamak heat transport in L-mode, H-mode and transient regimes ». In : *Plasma Physics and Controlled Fusion* 39.2 (1997), p. 261 (cf. p. 20, 79).

[46] L-G ERIKSSON, T HELLSTEN et U WILLÉN. « Comparison of time dependent simulations with experiments in ion cyclotron heated plasmas ». In : *Nuclear Fusion* 33.7 (1993), p. 1037 (cf. p. 79).

[47] AR ESTERKIN et AD PILIYA. « Fast ray tracing code for LHCD simulations ». In : *Nuclear fusion* 36.11 (1996), p. 1501 (cf. p. 79).

[48] Damien ESTÈVE. « Etude gyrocinétique du transport multi-espèces néoclassique et turbulent dans un plasma de fusion ». Thèse de doct. Aix-Marseille, 2015 (cf. p. 15).

[49] Damien ESTÈVE, Yanick SARAZIN, Xavier GARBET, Virginie GRANDGIRARD et al. « Self-consistent gyrokinetic modeling of neoclassical and turbulent impurity transport ». In : *Nuclear Fusion* (2017) (cf. p. 18, 20, 42, 43).

[50] Rodney C. EWING, William J. WEBER et Jie LIAN. « Nuclear waste disposal—pyrochlore (A2B2O7) : Nuclear waste form for the immobilization of plutonium and "minor" actinides ». In : *Journal of Applied Physics* 95.11 (2004), p. 5949–5971. DOI : 10.1063/1.1707213 (cf. p. 10).

[51] E FABLE, C ANGIONI, R FISCHER, B GEIGER et al. « Progress in characterization and modelling of the current ramp-up phase of ASDEX Upgrade discharges ». In : *Nuclear Fusion* 52.6 (2012), p. 063017 (cf. p. 27).

[52] N FEDORCZAK, P MONIER-GARBET, T PÜTTERICH, S BREZINSEK et al. « Tungsten transport and sources control in JET ITER-like wall H-mode plasmas ». In : *Journal of nuclear materials* 463 (2015), p. 85–90 (cf. p. 74).

[53] Noël FLEUROT, Claude CAVAILLER et JL BOURGADE. « The Laser Megajoule (LMJ) Project dedicated to inertial confinement fusion : Development and construction status ». In : *Fusion Engineering and Design* 74.1 (2005), p. 147–154 (cf. p. 14).

[54] T. FÜLÖP, S. BRAUN et I. PUSZTAI. « Impurity transport driven by ion temperature gradient turbulence in tokamak plasmas ». In : *Physics of Plasmas* 17.6 (2010), p. 1–9. ISSN : 1070664X. DOI : 10.1063/1.3430639 (cf. p. 52).

[55] T. FULOP et P. HELANDER. « Nonlinear neoclassical transport in a rotating impure plasma with large gradients ». In : *Doktorsavhandlingar vid Chalmers Tekniska Hogskola* 3066.1538 (1999), p. 3066–3075. ISSN : 0346718X. DOI : 10.1063/1.873593 (cf. p. 52, 53, 61, 72).

[56] T. FÜLÖP et P. HELANDER. « Nonlinear neoclassical transport in toroidal edge plasmas ». In : *Contributions to Plasma Physics* 42.2-4 (2002), p. 339–349. ISSN : 08631042. DOI : 10.1002/1521-3986(200204)42:2/4<339::AID-CTPP339>3.0.CO;2-H (cf. p. 53).

[57] J GARCIA, N HAYASHI, B BAIOCCHI, G GIRUZZI et al. « Physics comparison and modelling of the JET and JT-60U core and edge : towards JT-60SA predictions ». In : *Nuclear Fusion* 54.9 (2014), p. 093010 (cf. p. 26).

[58] C GARCIA-ROSALES. « Erosion processes in plasma-wall interactions ». In : *Journal of nuclear materials* 211.3 (1994), p. 202–214 (cf. p. 22).

[59] M GELFUSA, A MURARI, I LUPELLI, N HAWKES et al. « Influence of plasma diagnostics and constraints on the quality of equilibrium reconstructions on Joint European Torus ». In : *Review of Scientific Instruments* 84.10 (2013), p. 103508 (cf. p. 90).

[60] M GONICHE, RJ DUMONT, V BOBKOV, P BURATTI et al. « Ion cyclotron resonance heating for tungsten control in various JET H-mode scenarios ». In : *Plasma Physics and Controlled Fusion* 59.5 (2017), p. 055001 (cf. p. 24).

[61] V GRANDGIRARD, Y SARAZIN, P ANGELINO, A BOTTINO et al. « Global full-f gyrokinetic simulations of plasma turbulence ». In : *Plasma Physics and Controlled Fusion* 49.12B (2007), B173. URL : http://stacks.iop.org/0741-3335/49/i=12B/a=S16 (cf. p. 41, 42).

[62] Virginie GRANDGIRARD, Jérémie ABITEBOUL, Julien BIGOT, Thomas CARTIER-MICHAUD et al. « A 5D gyrokinetic full-f global semi-lagrangian code for flux-driven ion turbulence simulations ». In : *Computer Physics Communications* 207 (2016), p. 35–68 (cf. p. 20).

[63] Christophe GUILLEMAUT. « Modélisation du bord d'un plasma de fusion en vue d'ITER et validation expérimentale sur JET ». Thèse de doct. Aix-Marseille, 2013 (cf. p. 16).

[64] R. GUIRLET. « Transport dans les plasmas de tokamak ». In : *Master 2 : Physique et Sciences de la Matière Spécialité : Sciences de la Fusion* 0 (2014) (cf. p. 43, 46).

[65] F GUZMÁN, M O'MULLANE et HP SUMMERS. « ADAS tools for collisional–radiative modelling of molecules ». In : *Journal of Nuclear Materials* 438 (2013), S585–S588 (cf. p. 79).

[66] Taik Soo HAHM et Keith H BURRELL. « Role of flow shear in enhanced core confinement regimes ». In : *Plasma Physics and Controlled Fusion* 38.8 (1996), p. 1427 (cf. p. 105).

[67] Gordon B HAXEL, James B HEDRICK, Greta J ORRIS, Peter H STAUFFER et James W HENDLEY II. *Rare earth elements : critical resources for high technology*. Rapp. tech. 2002 (cf. p. 14).

[68] JA HEIKKINEN, TP KIVINIEMI, T KURKI-SUONIO, AG PEETERS et SK SIPILÄ. « Particle simulation of the neoclassical plasmas ». In : *Journal of Computational Physics* 173.2 (2001), p. 527–548 (cf. p. 79).

[69] P. HELANDER et D.J. SIGMAR. *Collisional Transport in Magnetized Plasmas*. 2002 (cf. p. 30, 52).

[70] Per HELANDER. « Neoclassical transport in a rotating impure plasma ». In : *Physics of Plasmas* 5.4 (1998), p. 1209–1211. ISSN : 1070664X. DOI : 10.1063/1.872629 (cf. p. 52).

[71] F L HINTON et R D HAZELTINE. « Theory of Plasma Transport in Toroidal Confinements Systems ». In : *Rev. Mod. Phys.* 48.2 (1976), p. 239–308 (cf. p. 44, 45).

[72] F. L. HINTON et S. K. WONG. « Neoclassical ion transport in rotating axisymmetric plasmas ». In : *Physics of Fluids* 28.10 (1985), p. 3082. ISSN : 00319171. DOI : 10.1063/1.865350. URL : http://adsabs.harvard.edu/cgi-bin/nph-data{_}query?bibcode=1985PhFl...28.3082H{\&}link{_}type=EJOURNAL$\backslash$npapers2://publication/doi/10.1063/1.865350$\backslash$nhttp://link.aip.org/link/PFLDAS/v28/i10/p3082/s1{\&}Agg=doi (cf. p. 72).

[73] S. P. HIRSHMAN et D.J. SIGMAR. « Neoclassical transport of impurities in tokamak plasmas ». In : *Nucl. Fusion* 1079 (1981) (cf. p. 52).

[74] W. a. HOULBERG, K. C. SHAING, S. P. HIRSHMAN et M. C. ZARNSTORFF. « Bootstrap current and neoclassical transport in tokamaks of arbitrary collisionality and aspect ratio ». In : *Physics of Plasmas* 4.9 (1997), p. 3230. ISSN : 1070664X. DOI : 10.1063/1.872465. URL : http://scitation.aip.org/content/aip/journal/pop/4/9/10.1063/1.872465 (cf. p. 21, 26, 49, 52, 54, 72, 79, 82, 116).

[75] IPCC. « Climate Change 2014 : Synthesis Report ». In : (2014). URL : http://www.ipcc.ch/report/ar5 (cf. p. 10).

[76] G JANESCHITZ, G FUSSMANN, J HOFMANN, LB RAN et al. « the ASDEX team, the NI team, the ICRH team ». In : *J. Nucl. Mater* 162.164 (1989), p. 624 (cf. p. 24).

[77] Frank JENKO, W DORLAND, M KOTSCHENREUTHER et BN ROGERS. « Electron temperature gradient driven turbulence ». In : *Physics of Plasmas* 7.5 (2000), p. 1904–1910 (cf. p. 20).

[78] E JOFFRIN, M BARUZZO, M BEURSKENS, C BOURDELLE et al. « First scenario development with the JET new ITER-like wall ». In : *Nuclear fusion* 54.1 (2013), p. 013011 (cf. p. 22, 90).

[79] E JOFFRIN, ACC SIPS, JF ARTAUD, A BECOULET et al. « The 'hybrid'scenario in JET : towards its validation for ITER ». In : *Nuclear fusion* 45.7 (2005), p. 626 (cf. p. 17).

[80] BB KADOMTSEV. « Magnetic field line reconnection ». In : *Reports on Progress in Physics* 50.2 (1987), p. 115 (cf. p. 79).

[81] Denis KALUPIN, I IVANOVA-STANIK, I VOITSEKHOVITCH, J FERREIRA et al. « Numerical analysis of JET discharges with the European Transport Simulator ». In : *Nuclear Fusion* 53.12 (2013), p. 123007 (cf. p. 27).

[82] Ye O KAZAKOV, I PUSZTAI, T FÜLÖP et T JOHNSON. « Poloidal asymmetries due to ion cyclotron resonance heating ». In : *Plasma Physics and Controlled Fusion* 54.10 (2012), p. 105010. ISSN : 0741-3335. DOI : 10.1088/0741-3335/54/10/105010. URL : http://stacks.iop.org/0741-3335/54/i=10/a=105010?key=crossref.2ddb38376aaee7c65f88bb36157a35fe (cf. p. 72).

[83] M. H. KEY. « Status of and prospects for the fast ignition inertial fusion concept ». In : *Physics of Plasmas* 14.5 (2007), p. 055502. DOI : 10.1063/1.2719178 (cf. p. 14).

[84] JE KINSEY, GM STAEBLER et RE WALTZ. « Predicting core and edge transport barriers in tokamaks using the GLF23 drift-wave transport model ». In : *Physics of Plasmas* 12.5 (2005), p. 052503 (cf. p. 26).

[85] Florian KOECHL, Alberto LOARTE, Vassili PARAIL, Paula BELO et al. « Modelling of transitions between L-and H-mode in JET high plasma current plasmas and application to ITER scenarios including tungsten behaviour ». In : *Nuclear Fusion* (2017) (cf. p. 26, 27, 79, 83, 84, 118).

[86] Matt LANDREMAN et Darin R ERNST. « Local and global Fokker–Planck neoclassical calculations showing flow and bootstrap current modification in a pedestal ». In : *Plasma Physics and controlled fusion* 54.11 (2012), p. 115006 (cf. p. 21).

[87] LL LAO, H St JOHN, RD STAMBAUGH, AG KELLMAN et W PFEIFFER. « Reconstruction of current profile parameters and plasma shapes in tokamaks ». In : *Nuclear fusion* 25.11 (1985), p. 1611 (cf. p. 79, 81).

[88] John D LAWSON. « Some criteria for a power producing thermonuclear reactor ». In : *Proceedings of the Physical Society. Section B* 70.1 (1957), p. 6 (cf. p. 14).

[89] A LOARTE, ML REINKE, AR POLEVOI, M HOSOKAWA et al. « Tungsten impurity transport experiments in Alcator C-Mod to address high priority research and development for ITER a ». In : *Physics of Plasmas* 22.5 (2015), p. 056117 (cf. p. 24, 74).

[90] P MANTICA, C ANGIONI, L Lauro TARONI, M VALISA et al. « Transport analysis of Tungsten and Beryllium in JET Hybrid Plasmas with the ITER-like wall ». In : 577.1997 (2012), p. 2012 (cf. p. 76).

[91] GF MATTHEWS, M BEURSKENS, S BREZINSEK, M GROTH et al. « JET ITER-like wall—overview and experimental programme ». In : *Physica Scripta* 2011.T145 (2011), p. 014001 (cf. p. 22).

[92] George H MILLER, Edward I MOSES et Craig R WUEST. « The National Ignition Facility : enabling fusion ignition for the 21st century ». In : *Nuclear fusion* 44.12 (2004), S228 (cf. p. 14).

[93] Sergei V MIRNOV. « VD Shafranov and Tokamaks ». In : *Journal of Plasma Physics* 82.1 (2016) (cf. p. 17).

[94] « Neoclassical analysis of impurity transport following transition to improved particle confinement ». In : *Nuclear Fusion* 30.6 (1990), p. 1117–1127. ISSN : 0029-5515. DOI : 10.1088/0029-5515/30/6/013 (cf. p. 30, 46, 48–50, 53, 54).

[95] R NEU, M BALDEN, V BOBKOV, R DUX et al. « Plasma wall interaction and its implication in an all tungsten divertor tokamak ». In : *Plasma Physics and Controlled Fusion* 49.12B (2007), B59 (cf. p. 22).

[96] R NEU, R DUX, A GEIER, O GRUBER et al. « Tungsten as plasma-facing material in ASDEX Upgrade ». In : *Fusion engineering and design* 65.3 (2003), p. 367–374 (cf. p. 22).

[97] R NEU, R DUX, A GEIER, A KALLENBACH et al. « Impurity behaviour in the ASDEX Upgrade divertor tokamak with large area tungsten walls ». In : *Plasma physics and controlled fusion* 44.6 (2002), p. 811 (cf. p. 22).

[98] Rudolf NEU, A KALLENBACH, M BALDEN, V BOBKOV et al. « Overview on plasma operation with a full tungsten wall in ASDEX Upgrade ». In : *Journal of Nuclear Materials* 438 (2013), S34–S41 (cf. p. 22).

[99] Hans NORDMAN, Jan WEILAND et Anders JARMÉN. « Simulation of toroidal drift mode turbulence driven by temperature gradients and electron trapping ». In : *Nuclear Fusion* 30.6 (1990), p. 983 (cf. p. 20, 79).

[100] ITER ORGANIZATION. *60 years of progress*. 2017. URL : https://www.iter.org/sci/BeyondITER (cf. p. 12).

[101] ITER ORGANIZATION. *Fuelling the fusion reaction*. 2017. URL : https://www.iter.org/sci/fusionfuels (cf. p. 11).

[102] ITER ORGANIZATION. *What will ITER do ?* 2017. URL : https://www.iter.org/sci/Goals (cf. p. 12).

[103] Alexei PANKIN, Douglas MCCUNE, Robert ANDRE, Glenn BATEMAN et Arnold KRITZ. « The tokamak Monte Carlo fast ion module NUBEAM in the National Transport Code Collaboration library ». In : *Computer Physics Communications* 159.3 (2004), p. 157–184 (cf. p. 26, 84).

[104] JWM PAUL. « The DITE experiment ». In : *Nuclear fusion* 25.9 (1985), p. 1097 (cf. p. 21).

[105] AG PEETERS et D STRINTZI. « The effect of a uniform radial electric field on the toroidal ion temperature gradient mode ». In : *Physics of plasmas* 11.8 (2004), p. 3748–3751 (cf. p. 20, 74, 75).

[106] V PHILIPPS. « Tungsten as material for plasma-facing components in fusion devices ». In : *Journal of nuclear materials* 415.1 (2011), S2–S9 (cf. p. 24).

[107] K L Van De PLASSCHE, J CITRIN, C BOURDELLE, V DAGNELIE et A HO. « Realtime capable quasilinear gyrokinetic modelling using neural networks ». In : *EPS* (2017) (cf. p. 73).

[108] Th PÜTTERICH, R NEU, R DUX, AD WHITEFORD, MG O'MULLANE, HP SUMMERS et al. « Calculation and experimental test of the cooling factor of tungsten ». In : *Nuclear Fusion* 50.2 (2010), p. 025012 (cf. p. 22, 23, 77, 81).

[109] J.M. RAX. *Physique des Tokamaks*. École polytechnique : Physique. Éd. de l'École polytechnique, 2011. ISBN : 9782730215800. URL : https://books.google.fr/books?id=V_O68-cPhgkC (cf. p. 18, 37, 39).

[110] PH REBUT. « The JET preliminary tritium experiment ». In : *Plasma Physics and Controlled Fusion* 34.13 (1992), p. 1749 (cf. p. 12).

[111] ML REINKE, IH HUTCHINSON, JE RICE, NT HOWARD et al. « Poloidal variation of high-Z impurity density due to hydrogen minority ion cyclotron resonance heating on Alcator C-Mod ». In : *Plasma Physics and Controlled Fusion* 54.4 (2012), p. 045004 (cf. p. 24, 52).

[112] D REITER. « Progress in two-dimensional plasma edge modelling ». In : *Journal of Nuclear Materials* 196 (1992), p. 80–89 (cf. p. 79).

[113] Francesco ROMANELLI et R KAMENDJE. « Overview of JET results ». In : *Nuclear Fusion* 49.10 (2009), p. 104006 (cf. p. 17).

[114] M ROMANELLI et M OTTAVIANI. « Effects of density asymmetries on heavy impurity transport in a rotating tokamak plasma ». In : *Plasma physics and controlled fusion* 40.10 (1998), p. 1767 (cf. p. 52, 53, 72).

[115] Michele ROMANELLI, Gerard CORRIGAN, Vassili PARAIL, Sven WIESEN et al. « JINTRAC : A System of Codes for Integrated Simulation of ». In : 9 (2014), p. 1–4 (cf. p. 26, 29, 52, 65, 74, 75, 79, 117).

[116] P. H. RUTHERFORD. « Impurity transport in the Pfirsch-Schluter regime ». In : *Physics of Fluids* 17.9 (1974), p. 1782. ISSN : 00319171. DOI : 10.1063/1.1694975. URL : http://link.aip.org/link/?PFLDAS/17/1782/1 (cf. p. 50).

[117] Tomar S. 1981 (cf. p. 79).

[118] Y. SARAZIN. « Turbulence and Transport ». In : *Master 2 : Physique et Sciences de la Matière, Spécialité : Sciences de la Fusion* (2013) (cf. p. 34, 35).

[119] M. SERTOLI, C. ANGIONI, ASDEX Upgrade Team T. ODSTRCIL et EUROFusion MST1 TEAM. « Parametric dependencies of the experimental tungsten transport coefficients in ICRH and ECRH assisted ASDEX Upgrade H-modes ». In : *Physics of Plasmas* 24.11 (2017), p. 112503. DOI : 10.1063/1.4996412 (cf. p. 21).

[120] M SERTOLI, T ODSTRCIL, C ANGIONI et al. « Interplay between central ECRH and saturated (m, n)=(1, 1) MHD activity in mitigating tungsten accumulation at ASDEX Upgrade ». In : *Nuclear Fusion* 55.11 (2015), p. 113029 (cf. p. 77).

[121] R SIMONINI, G CORRIGAN, G RADFORD, J SPENCE et A TARONI. « Models and Numerics in the Multi-Fluid 2-D Edge Plasma Code EDGE2D/U ». In : *Contributions to Plasma Physics* 34.2-3 (1994), p. 368–373 (cf. p. 79).

[122] European Nuclear SOCIETY. *Fuel comparison*. 2017. URL : https://www.euronuclear.org/info/encyclopedia/f/fuelcomparison.htm (cf. p. 11).

[123] Lyman SPITZER JR. « The stellarator concept ». In : *The Physics of Fluids* 1.4 (1958), p. 253–264 (cf. p. 13).

[124] G. M. STAEBLER, J. E. KINSEY et R. E. WALTZ. « A theory-based transport model with comprehensive physics ». In : *Physics of Plasmas* 14.5 (2007), p. 1–7. ISSN : 1070664X. DOI : 10.1063/1.2436852 (cf. p. 52).

[125] Gary M STAEBLER, Jon E KINSEY, Emily A BELLI, Jefferey CANDY et al. « Resolving the mystery of transport within internal transport barriers a ». In : *Physics of Plasmas* 21.5 (2014), p. 055902 (cf. p. 26, 91).

[126] GM STAEBLER, GL JACKSON, WP WEST, SL ALLEN et al. « Improved High-Confinement Mode with Neon Injection in the DIII-D Tokamak ». In : *Physical review letters* 82.8 (1999), p. 1692 (cf. p. 113).

[127] GM STAEBLER, JE KINSEY et RE WALTZ. « Gyro-Landau fluid equations for trapped and passing particles ». In : *Physics of Plasmas* 12.10 (2005), p. 102508 (cf. p. 20, 79).

[128] T TALA, F IMBEAUX, V.V PARAIL, C BOURDELLE et al. « Fully predictive time-dependent transport simulations of ITB plasmas in JET, JT-60U and DIII-D ». In : *Nuclear Fusion* 46.5 (2006), p. 548–561. ISSN : 0029-5515. DOI : 10.1088/0029-5515/46/5/007 (cf. p. 26).

[129] S. TAMOR. « ANTIC : A Code for Calculation of Neutral Transport in Cylindrical Plasmas ». In : 19 (1980) (cf. p. 83).

[130] Tetsuo TANABE. *Tritium : Fuel of Fusion Reactors*. Springer, 2017 (cf. p. 11).

[131] Chris THOMAS, Alison CAMERON, Rhys GREEN, Michel BAKKENES et al. « Extinction risk from climate change ». In : 427 (fév. 2004), p. 145–8 (cf. p. 10).

[132] D VAN HOUTTE, G MARTIN, A BECOULET, J BUCALOSSI et al. « Recent fully non-inductive operation results in Tore Supra with 6 min, 1 GJ plasma discharges ». In : *Nuclear Fusion* 44.5 (2004), p. L11 (cf. p. 12).

[133] D VEZINET, D MAZON, R GUIRLET, J DECKER et Y PEYSSON. « Impurity density derivation from bandpass soft x-ray tomography : applicability, perspectives and limitations ». In : *Nuclear Fusion* 54.8 (2014), p. 083011 (cf. p. 77).

[134] I VOITSEKHOVITCH, P BELO, J CITRIN, E FABLE et al. « Modelling of JET hybrid scenarios with GLF23 transport model : E× B shear stabilization of anomalous transport ». In : *Nuclear Fusion* 54.9 (2014), p. 093006 (cf. p. 26).

[135] Stodiek VON GOELER, W STODIEK et N SAUTHOFF. « Studies of internal disruptions and m= 1 oscillations in tokamak discharges with soft—x-ray techniques ». In : *Physical Review Letters* 33.20 (1974), p. 1201 (cf. p. 17).

[136] RE WALTZ, GM STAEBLER, W DORLAND, GW HAMMETT, M KOTSCHENREUTHER et JA KONINGS. « A gyro-Landau-fluid transport model ». In : *Physics of Plasmas* 4.7 (1997), p. 2482–2496 (cf. p. 20, 26, 79).

[137] J WEILAND, AB JARMEN et H NORDMAN. « Diffusive particle and heat pinch effects in toroidal plasmas ». In : *Nuclear Fusion* 29.10 (1989), p. 1810 (cf. p. 20, 79).

[138] Jan WEILAND et Hans NORDMAN. « Drift wave model for inward energy transport in tokamak plasmas ». In : *Physics of Fluids B : Plasma Physics* 5.5 (1993), p. 1669–1671 (cf. p. 26).

[139] J. WESSON et D. CAMPBELL. *Tokamaks*. T. 149. 2011, p. 1–37 (cf. p. 14, 21, 29).

[140] J. A. WESSON. « Poloidal distribution of impurities in a rotating tokamak plasma ». In : *Nuclear Fusion* 37.5 (1997), p. 577. ISSN : 0029-5515. DOI : 10.1088/0029-5515/37/5/I01. URL : http://iopscience.iop.org/0029-5515/37/5/I01$\backslash$nhttp://iopscience.iop.org/0029-5515/37/5/I01/pdf/0029-5515{_}37{_}5{_}I01.pdf (cf. p. 23, 52, 53, 72, 77).

[141] Hartmut ZOHM. « Edge localized modes (ELMs) ». In : *Plasma Physics and Controlled Fusion* 38.2 (1996), p. 105 (cf. p. 16).